

Abstract

Title of Dissertation: The Origins and Ionization Mechanisms of
H α Filaments in the Cool Cores of
Galaxy Groups and Clusters

Michael McDonald, Doctor of Philosophy, 2011

Dissertation directed by: Professor Sylvain Veilleux
Department of Astronomy

We present a survey of 10 galaxy groups and 23 galaxy clusters aimed at explaining the presence of warm, ionized filaments in the cool cores of galaxy clusters. By combining deep, high spatial resolution H α , far-UV, and X-ray data from the *Maryland Magellan Tunable Filter*, *Hubble Space Telescope*, and *Chandra X-ray Observatory*, respectively, we have assembled the most complete picture of these mysterious filaments to date. This extensive database has allowed us to shed new light on two critical questions: i) Where does the cool gas in these filaments come from? ii) What process or processes are responsible for ionizing the cool filaments.

As a pilot project, we obtained high-resolution H α and far-UV data for Abell 1795 and find that the previously-discovered H α filament is, in fact, two very thin, intertwined filaments extending 50 kpc and with a width < 700 pc. The clumpy UV morphology and UV/H α flux ratios of these filaments suggest that they may consist of chains of star-forming regions. Based on these data we conclude that the H α emission is a result of photoionization by young stars and that the cool gas filaments are a byproduct of the intracluster medium cooling onto a fast-moving central galaxy.

When we consider the full sample of 23 galaxy clusters, we find several strong correlations between the X-ray and H α data. In general, complex, extended H α

filaments are found in clusters with cool, low-entropy cores. Furthermore, the morphology of the warm gas is correlated with the soft X-ray morphology and the filaments are found to occupy regions where, locally, the intracluster medium is cooling fastest. Finally, we find a strong correlation between the mass of gas cooling below X-ray temperatures and the mass of gas in the warm filaments. These results provide strong evidence that the ionized filaments are a result of highly-asymmetric runaway cooling in the intracluster medium.

By extending this sample to include 10 galaxy groups we are able to probe more than 2 orders of magnitude in mass and cooling rate. We find that there is only a weak correlation between the presence of ionized filaments and the total mass of the system. Instead, the presence of ionized filaments appears to depend almost entirely on the *core* properties, specifically whether there is a cool, low-entropy core. We find that groups are, in general, cooling more efficiently than clusters, due to their lower starting temperature. This can only be the case if cool-core groups are experiencing exclusively weak AGN feedback, which we show is the case.

Finally, using new far-UV data from the *Hubble Space Telescope*, we find that 12/15 systems with H α emission are consistent with being photoionized by young stars. The three remaining systems are under-luminous in the far-UV for their H α luminosity, suggesting an alternative ionization source such as fast shocks or significant internal reddening. When we supplement this sample with UV data from *GALEX* and IR data from *Spitzer* we find a correlation between the star formation rate and the ICM cooling rate for 32 systems. The inferred efficiency of stars forming out of the cooling ICM is $14_{-8}^{+18}\%$, which is consistent with the Universal fraction of baryons in stars. These results suggest that, for the majority of cases, young star formation provides sufficient UV flux to ionize the cool filaments.

**The Origins and Ionization Mechanisms of
H α Filaments in the Cool Cores of
Galaxy Groups and Clusters**

by

Michael McDonald

Dissertation submitted to the Faculty of the Graduate School of the
University of Maryland at College Park in partial fulfillment
of the requirements for the degree of
Doctor of Philosophy
2011

Advisory Committee:

Professor Sylvain Veilleux, chair
Professor Ted Jacobson
Professor Michael Loewenstein
Professor Richard Mushotzky
Professor Stuart Vogel

© Michael McDonald 2011

Preface

The contents of this thesis are published in a series of four articles in the Astrophysical Journal. The titles of these articles, their publication date, and the location of the published results in this thesis are as follows:

Paper Title	Pub. Date (Journal)	Thesis Chapter
MMTF-H α and HST-FUV Imaging of the Filamentary Complex in Abell1795	10/2009 (ApJ Letter)	§2
On the Origin of the Extended H α Filaments in Cooling Flow Clusters	10/2010 (ApJ Article)	§3
The Effect of Environment on the Formation of H α Filaments and Cool Cores in Groups and Clusters	02/2011 (ApJ Article)	§4
Star Formation Efficiency in the Cool Cores of Galaxy Clusters	04/2011 (ApJ Article)	§5

Dedicated to: My wife, Kelly, for putting her eggs in this basket.

Acknowledgements

I would like to take this opportunity to thank my advisor, Sylvain Veilleux, for all that he has done for me over the past four years. His unique ability to provide guidance and support while allowing considerable independence created the ideal environment for me to grow as a scientist. Moreover, witnessing him balance work with family helped me to grow as a person. I look forward to many years of continued collaborations and, more importantly, many more pisco sours and empanadas.

I am also indebted to Richard Mushotzky and David Rupke for considerable contributions to this work. Richard introduced me to the world of X-ray astronomy, and was the primary source of knowledge for all things related to cooling flows over the past two years. It is mainly due to his efforts that I can call myself an X-ray astronomer while keeping a straight face. David passed the mantle of "MMTF guy" to me during our brief overlap at the University of Maryland, providing me with a 1-year crash course on tunable filters. His careful, deliberate nature taught me to slow down and do things right the first time.

There are countless other people at UMD and elsewhere who have helped to shape both me and this thesis over the past four years, but a few stand out and deserve mention. My MSc advisor, Stéphane Courteau, who instilled in me a love for astronomy and a drive to succeed many years ago. Stacy Teng, who taught me everything I know about reducing X-ray data. Lisa Wei, who, despite my aversion to radio astronomy, has turned me on to sub-mm work. Stuart Vogel, Chris Reynolds, Eve Ostriker, and Cole Miller, for providing constructive feedback on this work over the years.

Finally, I would like to thank my family for being there for me during this process. To my parents, who taught me the value of hard work from a very young age, thank you. Without your support and encouragement, none of this would have been possible. I'll never be able to repay you for everything you've done for me. And lastly to my wife, Kelly, thank you for being so totally awesome. Your support and selflessness know no bounds. You are truly my partner in every sense of the word and I'm forever grateful to have found you.

Contents

List of Tables	ix
List of Figures	x
1 Introduction	1
1.1 Galaxies and Galaxy Clusters	1
1.2 The History and Properties of Cooling Flows	2
1.3 Optical Emission in Cluster Cores	5
1.4 Potential Ionization Sources in Cluster Cores	7
1.5 Star Formation in Brightest Cluster Galaxies	8
1.6 Observatories/Instruments Used in This Work	9
1.6.1 Chandra X-ray Observatory – ACIS	11
1.6.2 Hubble Space Telescope – ACS/SBC	12
1.6.3 Magellan – The Maryland Magellan Tunable Filter	13
1.7 Outline of Thesis	15
2 MMTF-$H\alpha$ and <i>HST</i>-FUV Imaging of the Filamentary Complex in Abell 1795	17
2.1 Introduction	17
2.2 Observations and Data Reduction	19
2.2.1 $H\alpha$ – Maryland-Magellan Tunable Filter	19
2.2.2 Far UV – Hubble Space Telescope ACS/SBC	19
2.3 Results	20
2.4 Discussion	24
2.4.1 Origin and Power Source of Filaments	24
2.5 Concluding Remarks	30
3 On the Origin of the Extended $H\alpha$ Filaments in Cooling Flow Clusters	32
3.1 Introduction	32
3.2 Data Collection and Analysis	36
3.2.1 $H\alpha$: MMTF	38

3.2.2	Near-UV: <i>GALEX</i> and <i>XMM-OM</i>	39
3.2.3	X-Ray: <i>Chandra</i>	41
3.2.4	1.4 GHz Radio: NVSS	47
3.3	Results	47
3.3.1	Warm Ionized Filaments	47
3.3.2	Star Formation	53
3.3.3	X-Ray Profiles	57
3.3.4	Properties of X-Ray Gas On and Off of Filament	64
3.3.5	Properties of BCGs	71
3.4	Discussion: Origin of the H α Filaments	74
3.4.1	Origin of the Cool Gas	76
3.4.2	Evidence for Conduction	80
3.4.3	Role of Magnetic Fields	81
3.5	Summary and Future Prospects	82
4	The Effect of Environment on the Formation of Hα Filaments and Cool Cores in Galaxy Groups and Clusters	85
4.1	Introduction	85
4.2	Data Collection and Analysis	87
4.2.1	Sample Selection	87
4.2.2	H α : MMTF	88
4.2.3	X-Ray: <i>Chandra</i>	91
4.3	Results	92
4.3.1	Warm Ionized Filaments	92
4.3.2	Global and Core X-Ray Properties	93
4.3.3	X-Ray – H α Correlations	100
4.4	Discussion	106
4.4.1	Groups vs Clusters: Differences and Similarities	106
4.4.2	The Origin of H α Filaments in Groups and Clusters	113
4.5	Summary and Future Prospects	114
5	Star Formation Efficiency in the Cool Cores of Galaxy Clusters	118
5.1	Introduction	118
5.2	Data Collection and Analysis	120
5.3	Results	123
5.4	Discussion	133
5.4.1	Star Formation as an Ionization Source	133
5.4.2	Star Formation Efficiencies in Cooling Flows	137
5.5	Summary and Future Prospects	140

6	Summary and Future Work	142
6.1	Summary	142
6.2	Future Work	146
6.2.1	Optical Spectroscopy of H α Filaments	146
6.2.2	A Complete Multiwavelength View of the ICM at $z\sim 0$	149
6.2.3	The Evolution of Feedback and Cooling in Cluster Cores	152
6.3	Conclusions	155
A	Properties of Individual Clusters	156
B	Glossary	162
	Bibliography	164

List of Tables

2.1	Luminosities, flux ratios, and SFRs for Abell 1795	31
3.1	Sample of 23 cooling flow clusters with MMTF H α imaging	37
4.1	Properties of our sample of 10 galaxy groups and 17 clusters	89
5.1	Sample of 15 cooling flow clusters with MMTF H α and HST FUV imaging	122
6.1	Multi-wavelength data available for our sample of cool core clusters .	151

List of Figures

1.1	Temperature profiles of cool core and non-cool core clusters	4
1.2	Multiwavelength view of Perseus A	6
1.3	Evidence for star formation in cool core BCGs	10
1.4	Chandra ACIS field of view	11
1.5	Field of view for HST ACS/SBC, MMTF, and ACIS	13
1.6	Schematic drawing of a Fabry-Perot etalon	15
2.1	High-resolution imaging of star-forming filaments in Abell 1795	21
2.2	Color composite image of Abell 1795	22
2.3	Close-up view of the criss-crossing filaments in Abell 1795	24
2.4	Plot of FUV versus $H\alpha$ surface brightness in Abell 1795	27
3.1	UV SEDs for 15 clusters from GALEX and XMM-OM	42
3.2	UV–NIR relations in cluster cores	43
3.3	Examples of on-filament X-ray spectral extraction regions	45
3.4	Multi-wavelength data for 21 clusters w/ NUV and $H\alpha$ data	49
3.4	Continued.	50
3.4	Continued.	51
3.4	Continued.	52
3.4	Continued.	53
3.5	False color X-ray images of three clusters in our sample	54
3.6	NUV versus $H\alpha$ luminosities for 21 cluster cores	55
3.7	Radial profiles of X-ray-derived cluster properties	58
3.8	$H\alpha$ -X-ray correlations in galaxy cluster cores	60
3.9	Plot of R_{cool} versus the maximum extent of $H\alpha$ emission	62
3.10	$H\alpha$ surface brightness profiles along filaments	63
3.11	Ratio of temperature and metallicity on and off of filaments	67
3.12	Metallicity of X-ray gas on filament compared to surrounding ICM	68
3.13	Distribution of various ICM properties in and out of filaments	69
3.14	1.4 GHz radio luminosities for clusters with and without filaments	72
3.15	Comparison of $H\alpha$ flux with K' -band luminosity of BCG	73
3.16	Simulated image of Perseus A at high redshift	75

4.1	X-ray and optical data for the 10 groups in this sample	94
4.1	Continued.	95
4.2	X-ray scaling relations for 10 groups and 17 clusters	97
4.3	Frequency of H α emission versus global X-ray properties	98
4.4	Frequency of H α emission versus core X-ray properties	101
4.5	H α -X-ray correlations for groups and clusters	103
4.6	Plot of R_{cool} versus the maximum extent of H α emission	104
4.7	Distribution of various ICM properties in and out of filaments	105
4.8	Correlation of various cooling rates with the cluster/group mass	108
4.9	1.4 GHz radio luminosity versus ICM cooling luminosity	112
5.1	Optical and FUV data for 15 galaxy cluster cores	124
5.1	Continued.	125
5.1	Continued.	126
5.2	FUV versus H α luminosity for 15 BCGs	127
5.3	Distribution of FUV/H α ratios for 10 clusters	130
5.4	Star formation rate versus X-ray cooling rate for 32 clusters	132
5.5	UV spectral energy distributions for 6 cluster cores	137
5.6	Distribution of star formation efficiencies for 26 cluster cores	139
6.1	Positioning of long-slit spectra along ionized filaments	146
6.2	Optical line ratios in filaments	148
6.3	Evolution of the cool core fraction with redshift	153
6.4	Simulated observations of high-redshift clusters at H α	154

Chapter 1

Introduction

1.1 Galaxies and Galaxy Clusters

The field of extragalactic astronomy was first born when it was discovered that the so-called “spiral nebulae” were, in fact, galaxies external to our own Milky Way Galaxy. The field quickly flourished, with the number of known external galaxies increasing by orders of magnitude with each decade. Large area surveys such as the Palomar All Sky Survey (Minkowski & Abell 1963; Reid et al. 1991), Two-Micron All-Sky Survey (Skrutskie et al. 2006), and the Sloan Digital Sky Survey (Abazajian et al. 2009) played a major role in mapping out the extragalactic universe in unprecedented detail, leading to a more complete understanding of galaxy properties with each successive survey.

One of the first (and most relevant to this work) discoveries about extragalactic sources was that they had a tendency to clump in space. In the 1920’s and 30’s, Shapley & Ames (1926) and Zwicky (1937, 1938) contributed to the growing body of research which eventually led to the conclusion that galaxies tend to live in groups and clusters, with only a relatively small fraction found in the field. With this new understanding, the study of galaxy clusters was sparked. Much like with

external galaxies, the number of known galaxy clusters quickly reached astronomical proportions aided early on by the pioneering work of Zwicky et al. (1961, 1963, 1966), Abell (1958) and Abell et al. (1989) who compiled the first substantial catalogs of thousands of galaxy clusters.

1.2 The History and Properties of Cooling Flows

While the study of galaxy clusters dates back to the 1930's, it wasn't until the 1960's that the hot intracluster medium (ICM; see Appendix B for a complete glossary) was discovered serendipitously by the first rocket-flown X-ray detectors. Soon after, this X-ray emission was identified as originating from hot gas at $\sim 10^7$ K which is cooling via a combination of line and thermal Bremsstrahlung emission. The gas is roughly in hydrostatic equilibrium, such that the temperature of the intracluster medium is proportional to the total mass in gas, stars, and dark matter. In typical galaxy clusters, the amount of mass in the hot ICM vastly outweighs the mass in stars. Thus, the discovery of the ICM completely revolutionized our understanding of galaxy clusters and provided a new technique to study their properties.

The fact that we observe X-ray emission from clusters is evidence that they are cooling radiatively. Early studies (see review by Fabian 1994) found that a large fraction of nearby clusters have dense cores of gas with cooling times shorter than the age of the cluster. Such a system should initiate a cooling flow, where gas cools, becomes denser, falls to smaller radius where the cooling time is shorter and, thus, continues to cool and fall in to the cluster core. Figure 1.1 shows the dichotomy between so-called "cool core" and "non cool core" systems. At large radii, the temperature profiles of clusters are all similar and are well-described by a gas in hydrostatic equilibrium. At small radii, a large fraction of clusters deviate from the

expected steadily-rising temperature profile, showing dense, low-temperature cores. In the absence of any reheating, the mass of gas cooling below X-ray temperatures ($\sim 10^6\text{K}$) per year is given by:

$$\frac{dM}{dt} = \frac{2L\mu m}{5kT} \quad (1.1)$$

where L is the cooling luminosity, μ is mean molecular weight, m is the mass of a proton, k is Boltzmann’s constant, and T is the temperature at the cooling radius. In the cores of some galaxy clusters, where the density, traced by the luminosity (L), is high and the temperature (kT) is relatively low, this should lead to massive amounts of cool gas ($\sim 100\text{--}1000 M_\odot \text{ yr}^{-1}$) being deposited onto the cluster core – hence the name “cool core clusters”. The lack of evidence for such large amounts of cold molecular gas or young stars is often referred to as the “cooling flow problem”.

More recent high spectral resolution X-ray observations of cluster cores (Peterson & Fabian 2006) have found that only a very small fraction of the mass in the “classical cooling flow” is cooling below X-ray temperatures ($\sim 0.3 \text{ keV}$). This discovery effectively split the problem in two: 1) What process prevents the gas that we observe to be cooling at 1 keV from reaching 0.3 keV? and 2) What happens to the small fraction of gas that we *do* observe to cool below X-ray temperatures? In addition, recent work by Peres et al. (1998) suggests that the cooling region is much smaller than previously thought, which implies overall lower estimates on the mass deposition rate. It is now generally accepted that some form of heating balances the radiative cooling, leading to reduced cooling rates on the order of $1\text{--}10 M_\odot \text{ yr}^{-1}$. Mechanical and radiative feedback from active galactic nuclei (AGN feedback) and starbursts (e.g., Peterson & Fabian 2006; Veilleux et al. 2005), gas sloshing in the cluster core (e.g., Zuhone & Markevitch 2009), merger shocks (e.g., Randall et al. 2002) and conduction from the surrounding ICM (e.g., Voigt & Fabian 2004) have all been suggested as possible contributors to ICM heating. However, the relative

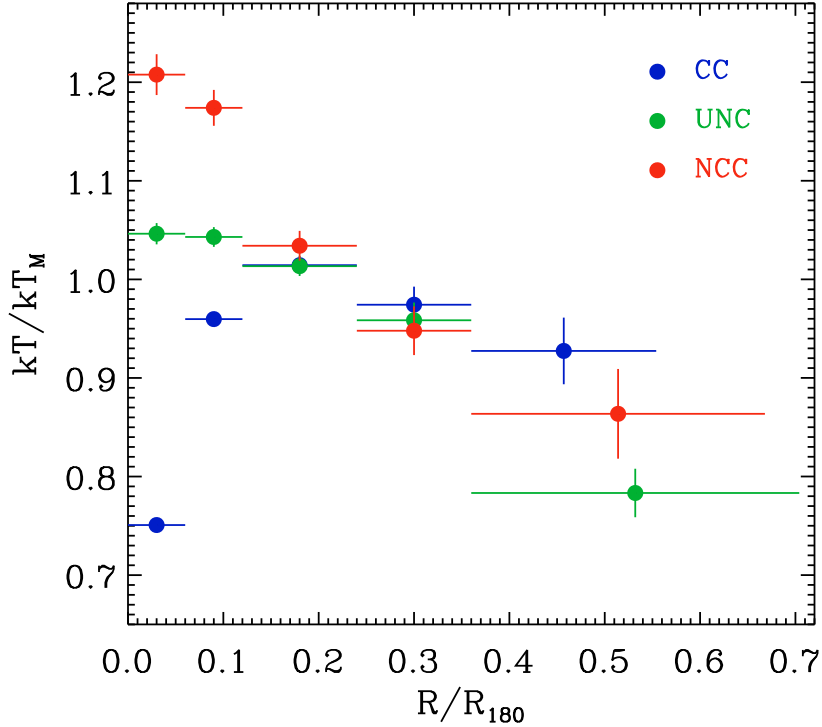


Figure 1.1 Mean temperature profiles for cool core (blue), non cool core (red), and uncertain (green) clusters from Leccardi & Molendi (2008). In the inner regions, the difference between cool core and non cool core is obvious, while in the outer regions the profiles are similar.

importance of each process remains unclear.

Further complicating matters is the fact many of these different processes which play an active role in galaxy clusters have a strong dependence on environment. In order to simplify things slightly, one can turn to galaxy groups, where the effects of heating may be more readily seen due to their lower mass and central density. This idea has been used to determine the role of AGN feedback in the galaxy group NGC 5098 (Randall et al. 2009). In this case, it was found that there is enough energy released into the IGM to offset the radiative cooling in the X-ray, thus solving the “cooling flow problem” for this specific case. This promising new technique of balancing cooling and feedback processes in galaxy groups is currently being pursued

by several research groups.

1.3 Optical Emission in Cluster Cores

The presence of warm ($T \sim 10^4\text{K}$) hydrogen in the form of line-emitting filaments extending from the BCG has been observed in many cool core clusters to date (e.g., Crawford et al. 1999; Heckman et al. 1989; Hu et al. 1985; Jaffe et al. 2005). The most notable case of such emission is in the core of the Perseus cluster (Figure 1.2). The brightest cluster galaxy, NGC1275, exhibits complex filamentary structure in $\text{H}\alpha$ extending for tens of kpc in radius (Conselice et al. 2001). While several intriguing ideas have been put forward, the origin of this gas and the mechanism for heating it are, as yet, unknown. While the presence of cool gas could be attributed to the purported cooling flow, one would then expect a relatively symmetric geometry. However, this is not generally the case. Crawford et al. (2005) provide a summary of the possible mechanisms which could produce cool gas with an asymmetric morphology for a specific scenario: a BCG with a high relative velocity at the center of a cooling flow cluster. Oegerle & Hill (2001) find that $\sim 15\%$ of BCGs are moving with a high peculiar velocity, so an asymmetric distribution of warm gas in this fraction of clusters would be relatively straightforward to explain in the context of Crawford et al. (2005).

Potential general explanations for the presence of extended, cool filaments are: i) runaway cooling of the ICM (e.g., Cowie et al. 1980; Fabian et al. 1984; Heckman et al. 1989; Sharma et al. 2010), ii) uplifted streams of cool gas from buoyant radio bubbles (e.g., Churazov et al. 2001; Revaz et al. 2008; Reynolds et al. 2005; Vernaleo & Reynolds 2007), iii) sloshing of cool gas about the potential minimum (e.g., Johnson et al. 2010; Zuhone & Markevitch 2009), and iv) stripping of gas from late-type

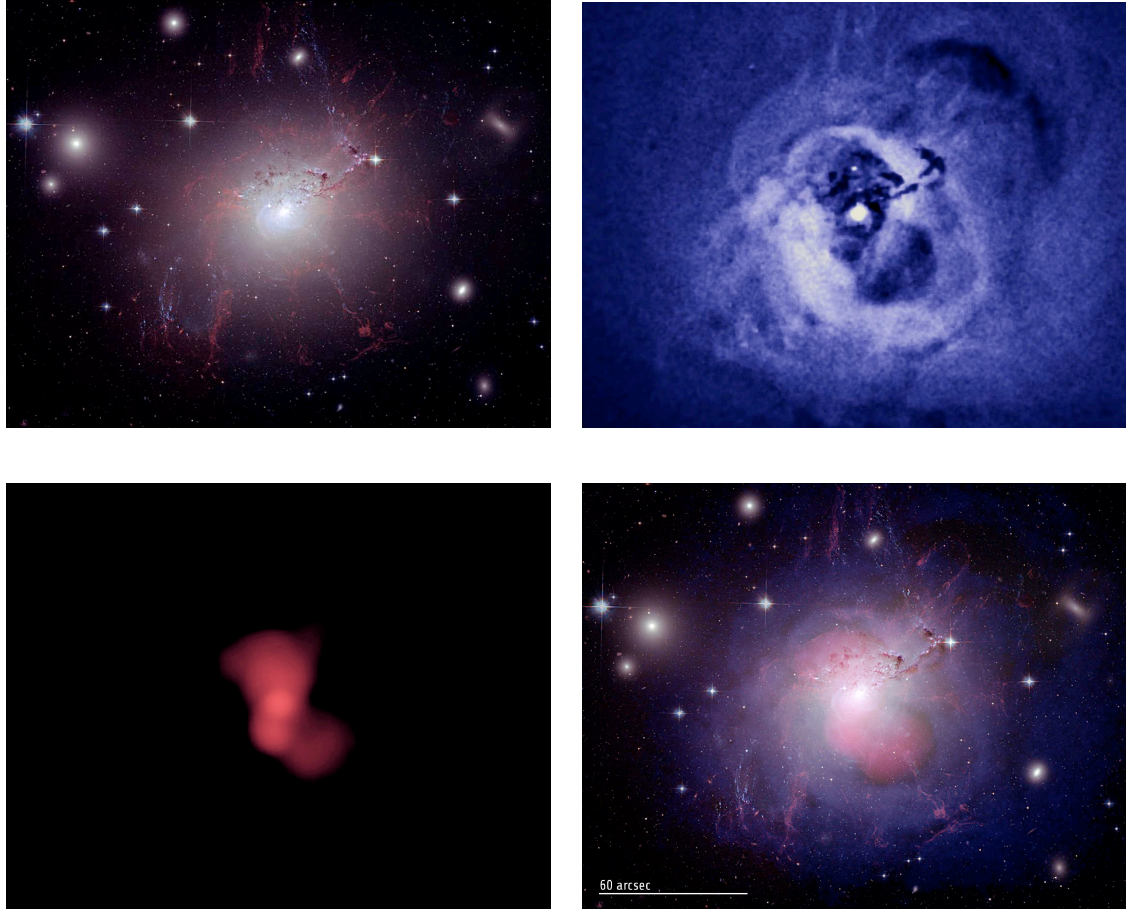


Figure 1.2 Multiwavelength images of the core of the Perseus cluster. Upper left: optical continuum and $H\alpha$ (red) emission. Upper right: X-ray unsharp mask. Lower left: 328 MHz radio emission. Lower right: All three panels overlaid. The scale bar represents 60 arcseconds (Fabian et al. 2006).

galaxies interacting with the BCG. Each of these mechanisms has the potential to produce thin, radial filaments of warm gas extending from the cluster core.

A major problem standing in the way of an explanation of these filaments is that there are still only a small number of known cases with clearly extended emission (i.e. NGC 1275, Abell 1795, Sersic 159-03). This is due to the fact that extended line emission is difficult to observe without a Fabry-Perot or an integrated-field spectrometer. Attempts have been made to quantify the fraction of BCGs which exhibit $H\alpha$ emission using the Sloan Digital Sky Survey (e.g., Edwards et al. 2007).

However, spectroscopic studies usually only tell us about the very center of the BCG, which will typically be bright in H α if an AGN is present. What is needed is a deep, wide-field, narrow-band survey of clusters of varying richness in order to assess the ubiquity and extent of the warm gas.

One of the more successful recent programs to look for extended emission in cooling flow clusters was that of Jaffe et al. (2005), using the Taurus Tunable Filter (TTF; Bland-Hawthorn & Jones 1998). The use of a tunable filter allows the observer to tune to a large range in wavelengths with a very narrow bandwidth ($\sim 10\text{\AA}$). The ability to tune the wavelength is particularly useful when observing cooling-flow clusters, of which there are very few in the local Universe. Thus, to observe H α , one typically needs to look at $\lambda > 6800\text{\AA}$, which a traditional H α narrow-band filter will not reach.

1.4 Potential Ionization Sources in Cluster Cores

Crawford et al. (2005) provide a list of potentially contributing heating/ionization sources in the optical line-emitting filaments, including (i) the central AGN, (ii) hot young stellar population outside the cD galaxy, (iii) X-rays from the ICM itself, (iv) heat conduction from the ICM to the colder filaments, (v) shocks and turbulent mixing layers, and (vi) collisional heating by cosmic rays. Arguments based on the AGN energetics and the line ratios in and out of the central region suggest that the AGN is not strongly influencing the ionization of the material much beyond the central region ($R \lesssim 6$ kpc). The long, thin geometry of the filaments and their quiescent velocity field (Crawford et al. 2005) seem to rule out ionization by shocks and/or turbulent mixing layers, while the relative weakness of high-ionization lines suggests that ionization by the X-ray ICM is also a small contributor. This leaves

scenarios (ii), (iv), and (vi) as the most plausible explanations for the dominant heating mechanism in the filaments.

A significant amount of the literature on cool core clusters is devoted to these three viable heating/ionization processes. Voigt & Fabian (2004) showed that, in a sample of 16 clusters, heating by conduction is able to offset radiative cooling and prevent massive cooling flows. If conduction is operating at such high efficiencies, it is plausible that it may also be responsible for ionizing the warm filaments. Another mechanism which can both quench the majority of the cooling and ionize the warm filaments is cosmic ray ionization (Crawford et al. 2005; Ferland et al. 2009). This mechanism is particularly promising due to the fact that the majority of cool core clusters have radio-loud AGN. Ferland et al. (2009) show that this method can reproduce the observed optical line ratios in emission-line nebulae. Finally, perhaps the least exotic ionization mechanism, photoionization by young stars, will be examined in more detail in the following section.

1.5 Star Formation in Brightest Cluster Galaxies

Shortly after it was realized that cooling flows may exist in the cores of galaxy clusters, there were multiple attempts at identifying star-forming regions in and around the central brightest cluster galaxy (hereafter BCG). While there was evidence found for star formation from CO, IR and UV data, the amount of star formation did not agree well with the expectations of $\sim 100 M_{\odot} \text{yr}^{-1}$. However, with the recent understanding that only a small fraction of the classical cooling flow is actually able to cool below X-ray temperatures, there have been several groups which have reported evidence for star formation (hereafter SF) which is within an order of magnitude of the expected rate if the cooling flow were completely converted into stars. Studies

in the optical (e.g., Rafferty et al. 2008), mid-IR (e.g., O’Dea et al. 2008, hereafter MIR), and UV (e.g., Hicks et al. 2010), have found typical SF rates ranging from $\sim 1\text{--}10 M_{\odot} \text{ yr}^{-1}$ (O’Dea et al. 2008). This implies that gas at temperatures of $\sim 10^{6\text{--}7}$ K is being continuously converted into stars with an efficiency on the order of $\sim 10\%$. The fact that most of these studies consider the *integrated* SF rates makes it difficult to determine the exact role of young stars in ionizing the extended warm gas observed at $\text{H}\alpha$, since the two may not be spatially coincident or the measurements may be contaminated by the inclusion of a central AGN.

In Figure 1.3 we present two studies which offer compelling evidence for star formation in cool core clusters. Hicks et al. (2010) present a careful analysis of archival GALEX near-far UV and *Spitzer* IR data and find that the cool cores of galaxy clusters occupy a similar space to star-forming galaxies in IR excess versus UV color. O’Dea et al. (2008) utilized millimeter emission from the CO molecule to estimate the total mass in molecular gas and found that it was strongly correlated with the amount of IR emission. This result matches exactly with what is seen in typical star-forming regions. These two studies offer compelling evidence that star formation *is* ongoing in cool cores, although the relationship between the star-forming regions and the optically-emitting filaments remains unknown due to the poor spatial resolution of these data.

1.6 Observatories/Instruments Used in This Work

A detailed multiwavelength approach is essential to track down all gas phases in the bright central galaxies (BCGs) and intracluster medium (ICM). Below, we describe the three instruments which have been crucial in allowing us to carefully map the hot and warm gas phases, along with the distribution of massive young stars, at

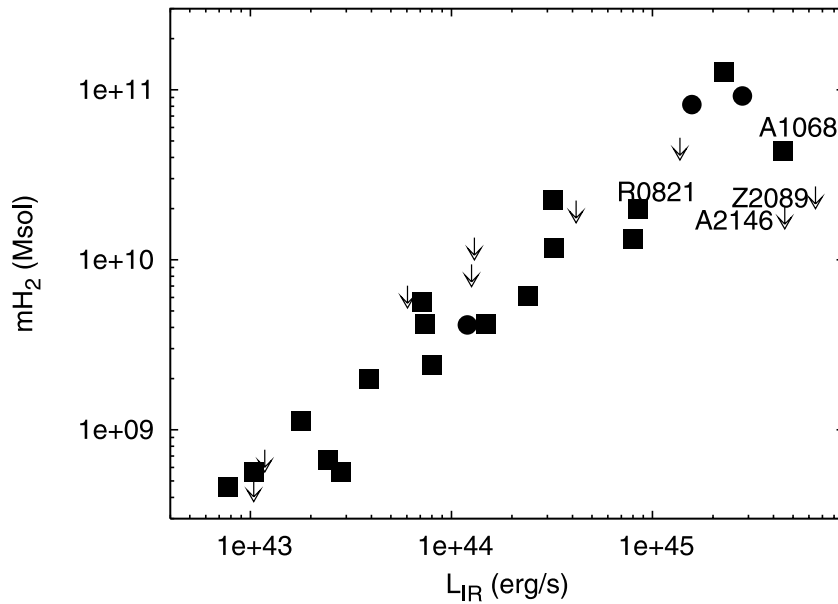
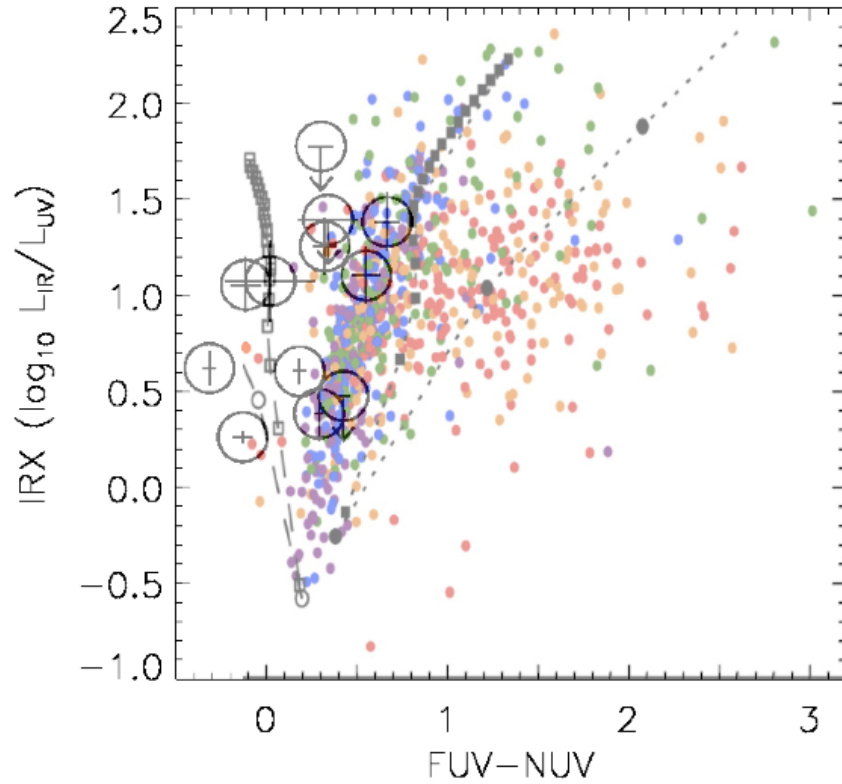


Figure 1.3 Top: Figure 9 from Hicks et al. (2010) showing IR excess versus UV color. Large circles represent BCGs in cool core clusters, while colored points show normal galaxies with strong (blue) to weak (red) star formation. The positions of the cool core clusters on this plot are consistent with galaxies exhibiting dusty star formation. Bottom: Figure 7 from O’Dea et al. (2008) showing H_2 mass (from CO) versus IR luminosity for cool core clusters. The strong correlation is indicative of star forming regions.

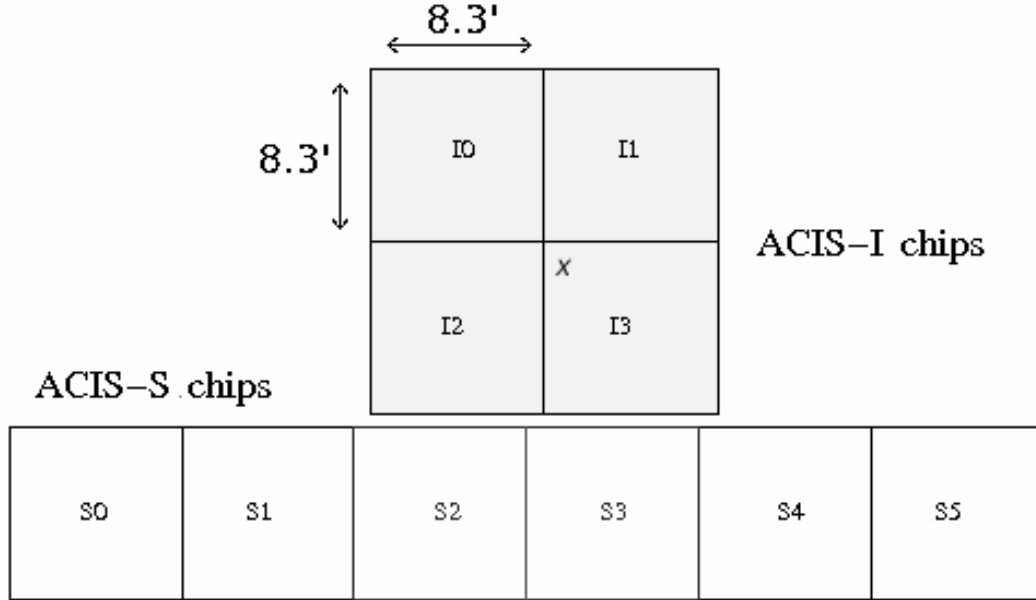


Figure 1.4 Field of view for the ACIS-I (4×4 chips, $16.6' \times 16.6'$) and ACIS-S (6 chips, $49.8' \times 8.3'$) spectroscopic imaging arrays on the *Chandra X-ray Observatory*.

unprecedented spatial resolution.

1.6.1 Chandra X-ray Observatory – ACIS

Due to its large field of view and superb spatial resolution, the Advanced CCD Imaging Spectrometer (ACIS) on the *Chandra X-ray observatory* is the ideal instrument to study structure in the hot intracluster medium. This imaging spectrometer has two focal plane arrays, as shown in Figure 1.4, with fields of view of $16.9' \times 16.9'$ for ACIS-I and $8.3' \times 50.6'$ for ACIS-S. Both arrays have a pixel scale of $0.492''/\text{pixel}$ and an 80% encircled power radius of $0.685''$, allowing for the easy identification of features such as filaments, shocks, and nuclei. This thesis utilizes archival data from both arrays.

With the ACIS instrument, each spatial pixel contains a complete spectrum from $\sim 0.5\text{--}8.0$ keV. With a deep enough exposure, this allows for the creation of 2-dimensional maps of spectroscopically-determined quantities such as the ICM

temperature, electron density, metal abundance, and cooling time. While these spectra are relatively low resolution ($\Delta E \sim 160eV$), they are sufficient to quantify the cooling properties of the ICM, assuming a cooling model a priori (e.g., Fabian 1994).

1.6.2 Hubble Space Telescope – ACS/SBC

For the past 20 years, the *Hubble Space Telescope* (HST) has been providing images of the Universe with unprecedented spatial resolution. The high quality of the onboard instruments allow for superior image quality over the wavelength range from 1150–17000Å, offering continuous coverage from the far-UV to the near-IR. Due to our requirement to achieve sub-arcsecond resolution in the UV (to match the ACIS and MMTF image quality) the Advanced Camera for Surveys Solar Blind Channel (ACS/SBC) was our preferred option over wider-field observatories such as the *Galaxy Evolution Explorer* (GALEX) and *XMM Optical Monitor* (XMM-OM).

This camera has a $35'' \times 35''$ field of view, which is significantly smaller than both the MMTF and ACIS fields of view (see Figure 1.5). However, as we discuss in §2 and §5, this is generally sufficient to image the full extent of the optical emission-line nebulae. The pixel scale and spatial resolution for the ACS/SBC is $0.032''/\text{pixel}$ and $\sim 0.06''$ (FWHM), respectively, allowing us to achieve sub-arcseconds resolution in the ultraviolet – something that XMM-OM and GALEX are unable to provide.

While the (STIS) instrument on HST also has an ultraviolet imaging mode, the sensitivity of this instrument at wavelengths shorter than 2000Å is slightly less than the ACS/SBC, making the ACS/SBC a more desirable option for this specific program.

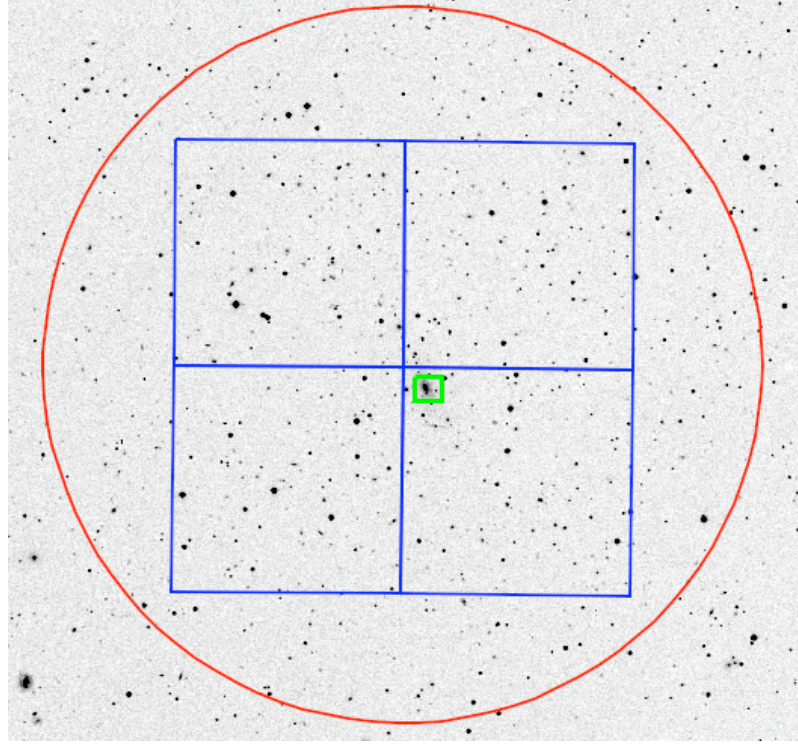


Figure 1.5 Field of views for the MMTF (red), ACIS I (blue) and ACS/SBC (green) overlaid on a digital sky survey image of Abell 229. While the ACS/SBC is quite small relative to the ACIS and MMTF field of view, it is large enough to fully image the BCG in most cases.

1.6.3 Magellan – The Maryland Magellan Tunable Filter

Built on the same principles as the TTF, the Maryland-Magellan Tunable Filter (MMTF; Veilleux et al. 2010) has taken narrow-band imaging to a whole new level. The MMTF functions as a standard Fabry-Perot (FP), employing two highly-reflective parallel plates and basic optics principles to filter out all but a given set of wavelengths, but is designed to work in lower orders. The equation governing the transmission of the tunable filter is:

$$T_e = \frac{(1 - R)^2}{1 + R^2 - 2R \cos \left(\left[\frac{2\pi}{\lambda} \right] 2nl \cos \theta \right)} = \frac{1}{1 + F \sin^2 \left(\left[\frac{2\pi}{\lambda} \right] nl \cos \theta \right)} \quad (1.2)$$

where λ is the wavelength of light incident on the plates, n is the refractive index of the material between the plates, l is the spacing of the highly-reflective plates, θ is the angle of incidence, R is the reflectance, and F is the coefficient of finesse, given by:

$$F = \frac{4R}{(1 - R)^2} \quad (1.3)$$

Equation 1.2 is illustrated in Figure 1.6. From this equation it is clear that, assuming straight-on incidence ($\theta = 0$), the transmission reaches a maximum for $(2\pi nl)/\lambda = 0, \pi, 2\pi, 3\pi$, etc. This means that the wavelength which achieves maximum transmission is directly proportional to the plate spacing. Thus, the filter can be “tuned” to transmit a specific wavelength by changing the plate spacing. The separation between adjacent peaks of different order, or the “free spectral range” is given by:

$$FSR \simeq \frac{\lambda^2}{2nl} \simeq \frac{\lambda}{mn} \quad (1.4)$$

where m is the order of interference. The width of the transmission window is given by:

$$\Delta\lambda \simeq \frac{FSR}{\pi\sqrt{F}/2} \simeq \frac{\lambda^2}{2nl} \frac{1}{\pi\sqrt{F}/2} \simeq \frac{\lambda^2}{nl\pi\sqrt{F}} \quad (1.5)$$

For the MMTF, the reflectance over the range 5000–9200Å is $95 \pm 5\%$, yielding a value of $F \sim 80$. With relatively large spacing, this can allow very fine wavelength resolution, for applications such as measuring accurate radial velocities. However, with high-precision electronics, one can control the spacing between the plates to mere microns. Specifically, the MMTF can operate with spacings ranging from 6.6 – 15.3 μm , which yields $\Delta\lambda \sim 10\text{Å}$ at $\lambda \sim 6600\text{Å}$. This very narrow bandpass can be tuned to any wavelength from 5000–9200Å. The MMTF is installed in the IMACS spectrograph on the Magellan 6.5m telescope. The combination of a superb observing site in Las Campanas, and the active optics employed at Magellan enables a typical delivered image quality of $\sim 0.5''$. Furthermore, the wide field of

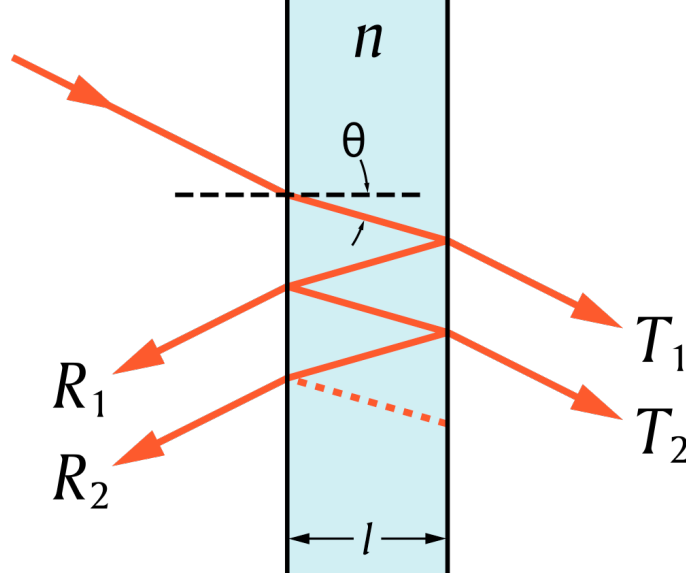


Figure 1.6 Schematic drawing of a Fabry-Perot etalon. The vertical lines represent the two highly-reflective plates, separated by a width of l , while the red lines represent the incident light which is arriving at an angle of incidence, θ .

the IMACS camera provides a field of view of $27'$ ($10'$ monochromatic). All of these factors combine to make the MMTF the best tunable filter currently in operation for investigating point source or extended line emission over large spatial scales.

1.7 Outline of Thesis

The goal of this thesis is to understand the origins and ionization mechanisms responsible for the optical line-emitting nebulae observed in the cool cores of galaxy clusters. We have attempted to address this complicated problem in a series of four papers (McDonald & Veilleux 2009; McDonald et al. 2011a, 2010, 2011b) which comprise the body of this thesis.

In Chapter 2 we present the first results from this project for a single cluster, Abell 1795. This chapter presents new, high-spatial resolution $H\alpha$ and far-UV imaging using the MMTF and *Hubble Space Telescope*. We discuss the current literature

on this unique object and attempt to explain the presence of the thin, extended, warm filaments in the context of star formation.

Chapter 3 represents the largest portion of this thesis, containing the results of our survey of 23 galaxy clusters with the MMTF. These optical data were supplemented with X-ray, UV, near-IR and radio data and represent the largest sample of high spatial resolution imaging of emission-line nebulae in cool core clusters to date. Using this wealth of high quality multi-wavelength data we present compelling evidence that these filaments are intimately linked to the rapidly cooling ICM. These results are discussed in the context of several current models.

In Chapter 4 we extend our sample of 23 clusters to include 10 lower-mass groups. The effect of environment is examined in a sample covering nearly 3 orders of magnitude in system mass. The results from Chapter 3 are also re-examined with the addition of these 10 additional systems.

In Chapter 5 we introduce new high-resolution far-UV data from the *Hubble Space Telescope* for 15 galaxy clusters. These data allow us to investigate photoionization by young stars as a potential ionization mechanism. We discuss the implications of our derived star formation rates in the context of the cooling flow model and galaxy formation in general.

Finally, in Chapter 6 we summarize the results of this work. We address outstanding questions which the current data are unable to resolve, and discuss upcoming work which will shed light on these remaining mysteries.

Chapter 2

MMTF- $H\alpha$ and *HST*-FUV Imaging of the Filamentary Complex in Abell 1795

2.1 Introduction

The absence of massive ($\sim 100 - 1000M_{\odot} \text{ yr}^{-1}$) cooling flows in the cores of X-ray luminous galaxy clusters is often used as prime evidence that feedback plays an important role in regulating star formation and galaxy formation in dense environments (see, e.g., review by Veilleux et al. 2005). Energies of a few $\times 10^{49}$ ergs per solar mass of stars formed are needed to explain the sharp cutoff at the bright end of the galaxy luminosity function. Starburst-driven winds are too feeble by a factor of several to fully account for the cutoff, so AGN feedback is invoked. The ubiquity of large “cavities” in the X-ray surface brightness of clusters with radio galaxies confirms that AGN outflows modify the thermodynamics of the intracluster medium (ICM; see review by Peterson & Fabian 2006). The relativistic gas injected into the

ICM by the AGN has enough energy to quench the mass accretion of cooling flows, but the exact mechanism by which the energy in the radio bubbles turns into heat is still debated.

The presence of warm hydrogen in the form of line-emitting filaments extending from the brightest cluster galaxy (hereafter BCG) has been observed in many cooling flow clusters to date (e.g., Crawford et al. 1999; Jaffe et al. 2005). However, while several intriguing ideas have been put forward, the origin of this gas and the mechanism for heating it are, as yet, unknown. Of all the galaxy clusters with known optical filaments, there is perhaps none quite so spectacular as Abell 1795. This cluster has been very extensively studied at a variety of wavelengths, leading to the discovery of a single, long (~ 50 kpc) filament seen in $H\alpha$ (Cowie et al. 1983; Jaffe et al. 2005) and X-ray (Fabian et al. 2001), a powerful, double-sided, radio jet (Ge & Owen 1993) emanating from the central AGN, and a very disturbed, star-forming, central region (McNamara et al. 1996).

As part of a survey of cooling flow clusters, we have carried out deep, high-resolution (delivered image quality, DIQ $\sim 0.7''$) imaging of Abell 1795 at $H\alpha$ and [N II] $\lambda 6583$ using the Maryland-Magellan Tunable Filter (MMTF) on the Magellan-Baade 6.5-m telescope and in the far-ultraviolet (FUV) using the ACS solar blind channel (SBC) camera on the *Hubble Space Telescope* (*HST*). These data far surpass any previously available images of the filaments in this cluster in both depth and spatial resolution; this chapter describes the results from our analysis of these data. The results from the survey will be presented in the upcoming chapters. The acquisition and reduction of the data on Abell 1795 are discussed in §2.2, followed by a description of the results (§2.3) and a discussion of the implications (§2.4). Throughout this chapter we assume a distance to Abell 1795 of 260 Mpc.

2.2 Observations and Data Reduction

2.2.1 $H\alpha$ – Maryland-Magellan Tunable Filter

MMTF has a very narrow bandpass ($\sim 5\text{--}12\text{\AA}$) which can be tuned to any wavelength over $\sim 5000\text{--}9200\text{\AA}$ (Veilleux et al. 2010). Coupled with the exquisite image quality of Magellan, this instrument is ideal for detecting emission-line filaments in distant clusters. During April 2008, we observed Abell 1795 for a total of 60 minutes each at $\lambda_{H\alpha} = 6972.8\text{ \AA}$, $\lambda_{[NII]} = 6994.7\text{ \AA}$ and $\lambda_{\text{continuum}} = 7044\text{ \AA}$. These data were reduced using the MMTF data reduction pipeline¹. The continuum image was then PSF and intensity matched to the narrow-band images to allow for careful continuum subtraction.

2.2.2 Far UV – Hubble Space Telescope ACS/SBC

FUV imaging was acquired using the ACS SBC on the *HST* in the F140LP bandpass, with a total exposure time of 1197 seconds. With the MMTF data already in hand, we were able to choose two different pointings of the $35'' \times 35''$ field of view to allow full coverage of the SE filament. Exposures with multiple filters are required to properly remove the known SBC red leak, which may be substantial in the central region due to the fact that the underlying galaxy is very luminous and red. However, we were unable to obtain complementary exposures in a redder SBC band for the filaments, due to scheduling constraints, and thus we proceed without removal of the offending light. The central UV fluxes have an associated error of $\sim 2.5\%$ due to the underlying red galaxy (based on a preliminary analysis of additional FUV data of the central galaxy obtained by W. Sparks and collaborators).

¹<http://www.astro.umd.edu/~veilleux/mmtf/datared.html>

2.3 Results

Figures 2.3 – 2.3 show the newly acquired MMTF and *HST* data on Abell 1795. The most striking result is that the “SE filament”, which has long been known (Cowie et al. 1983) is, in fact, a pair of thin, intertwined filaments in $H\alpha$. These filaments are $\sim 42''$ and $35''$ (52.9 and 44.1 kpc) in length, and their widths in $H\alpha$ are unresolved ($< 0''.7 \sim 1$ kpc). The discovery of thin strands in the SE filament is reminiscent of magnetic field lines. A stronger than average magnetic field in the ICM could prevent the filament material from evaporating due to thermal conduction. The BCG in Abell 1795 is a bright double-jet radio-loud cD galaxy (4C 26.42) with therefore strong extended magnetic field (Ge & Owen 1993), but radio emission is not detected beyond ± 6 kpc from the nucleus. We return to this issue in §2.4.

In the central region of Abell 1795, the $H\alpha$ emission forms a ring, with a cavity slightly northeast of the BCG center (Figure 2.3). The morphology is very similar to that seen in the X-ray (Fabian et al. 2001). The cavity surrounds one of the radio jets emanating from the AGN, suggesting that it was created by recent AGN activity (Crawford et al. 2005). The very sharp extension directly to the southwest of the central region is coincident with the counter-jet. The jet appears to be efficiently heating the gas in this region (van Breugel et al. 1984). In general, the $H\alpha$ emission spatially correlates well with the X-ray emission in both the central regions and on larger scales to within the spatial resolution of the X-ray data.

The upper middle panel of Figure 2.3 reveals the distribution of [N II] in Abell 1795. All of the features that are seen in $H\alpha$ are also visible in [N II], including both filaments, the short SW jet, the nucleus and the cavity northeast of the nucleus. The ratio of [N II]/ $H\alpha$, a measure of the relative importance of heating and ionization, is high and fairly uniform throughout the filaments (~ 0.35 – 0.55 , see Table 2.1 and the

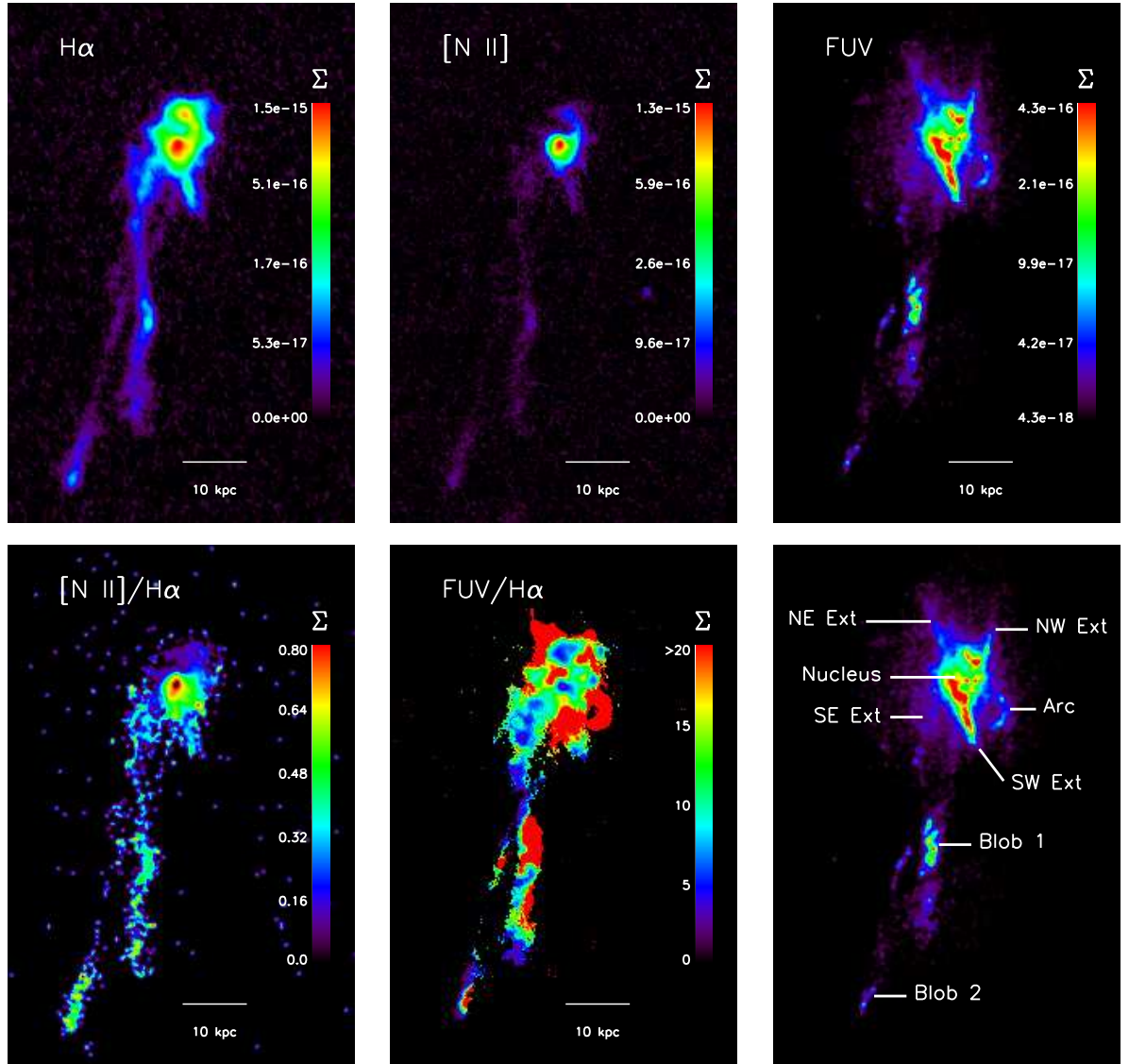


Figure 2.1 MMTF H α and [N II] λ 6583 and *HST*/SBC FUV images of Abell 1795. The three upper panels show maps of the surface brightness, Σ , in units of $\text{ergs s}^{-1} \text{cm}^{-2} \text{arcsec}^{-2}$. The lower left and center panels are [N II]/H α and FUV/H α ratio maps, respectively. In the latter image, the red shade represents regions where there is very little or no H α coincident with the FUV emission. The bottom right panel outlines the terminology we use in this chapter, specifically in Table 2.1, for the different regions. The “central region” consists of all emission north of (and including) the SW extension.

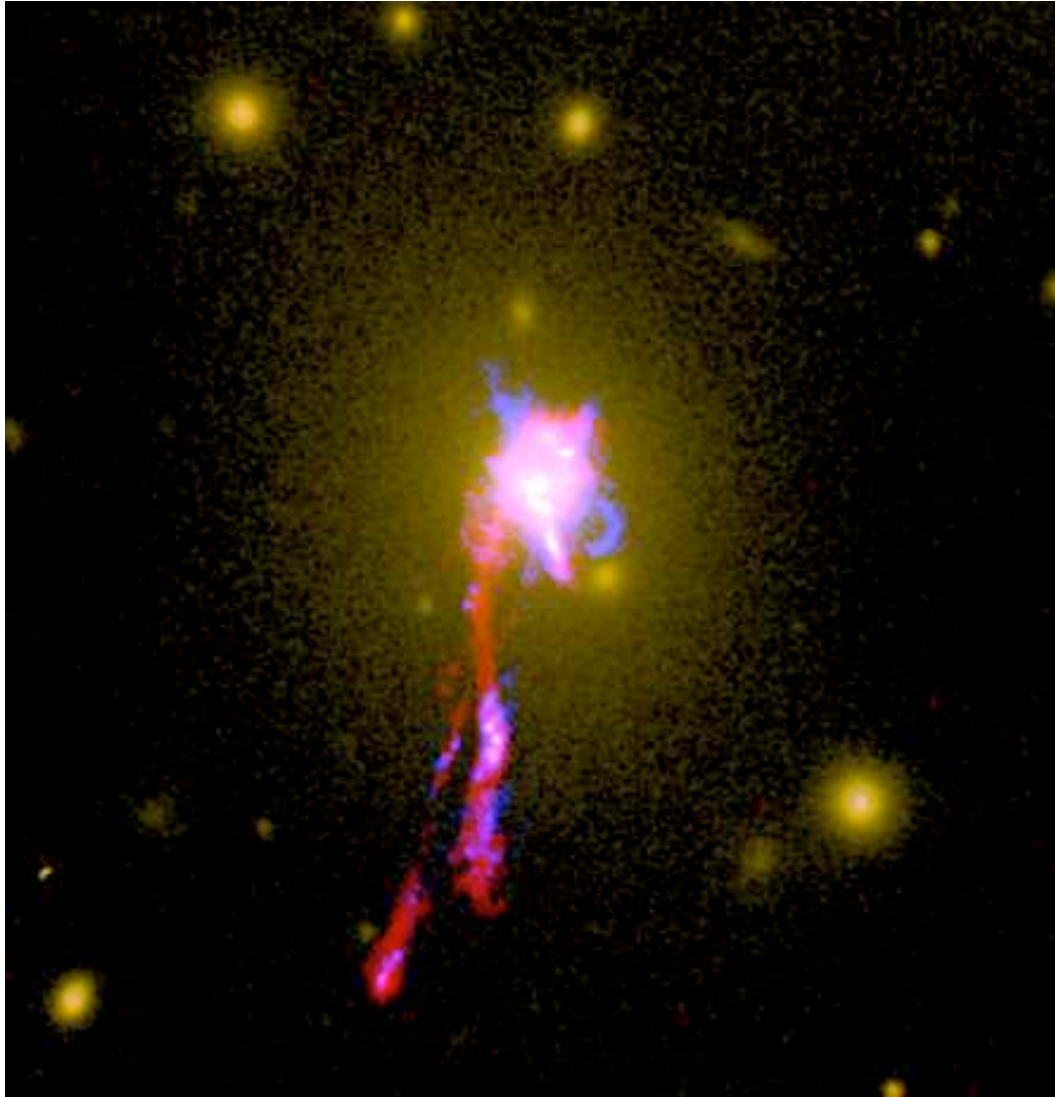


Figure 2.2 Color composite image of Abell 1795. The three colors represent the red continuum (yellow), $H\alpha$ (red) and far UV (blue). The long SE filament is resolved into two intertwined filaments in $H\alpha$ and FUV.

lower left panel of Figure 2.3); this elevated ratio confirms earlier results (Crawford et al. 2005, and references therein) and seems inconsistent with photoionization by hot stars. $[N II]/H\alpha$ is even higher in the nucleus, approaching unity, likely due to heating by the AGN, and drops northeast of the nucleus, where the jet has apparently cleared out a cavity. Given the MMTF bandwidth ($\sim 10\text{\AA}$), we note that

the [N II] image will also contain any H α with relative velocity $>785 \text{ km s}^{-1}$, and vice versa. However, since the typical velocity widths are $\sim 300 \text{ km s}^{-1}$ in the filaments (e.g., Crawford et al. 2005), we do not expect interline contamination to be important.

In the FUV (Figure 2.3, upper right panel, and Figure 2.3), both strands are visible and, with the added resolution of *HST*, are resolved in some regions into chains of bright, compact sources – the sites of recent star formation (see also Crawford et al. 2005). The two brightest blobs seen in the filaments at H α (blobs #1 and #2 in the nomenclature of Figure 2.3) break up in FUV point-source and diffuse emission, but spatial offsets of $\sim 1\text{--}2 \text{ kpc}$ are visible between the H α and FUV emission centroids. This shift is particularly obvious in the FUV/H α map in the lower middle panel of Figure 2.3. We do not believe this relative offset is due to astrometric errors since it was also noted in the earlier data of Crawford et al. (2005).

Most of the bright H α features in the central region emit strong FUV, such as the nucleus, the ring and the SW extension. However, there are features in the central region that are not common between the FUV and H α data. In the FUV map, there are two northern extensions to the east and west (the NE and NW “extensions” in Figure 2.3), as well as a curved extension southwest of the central region (the “arc”). The emission in these regions is lumpy but largely unresolved into point sources. In H α , there is a very bright and thick extension at the base of the SE filament which is not nearly as bright in the FUV. This region and other anomalous features are easily identified in the FUV/H α map. (More details will be given in an upcoming chapter where images of the central region of Abell 1795 in all three FUV bands of ACS/SBC are considered. This multiband analysis is beyond the scope of the present chapter.

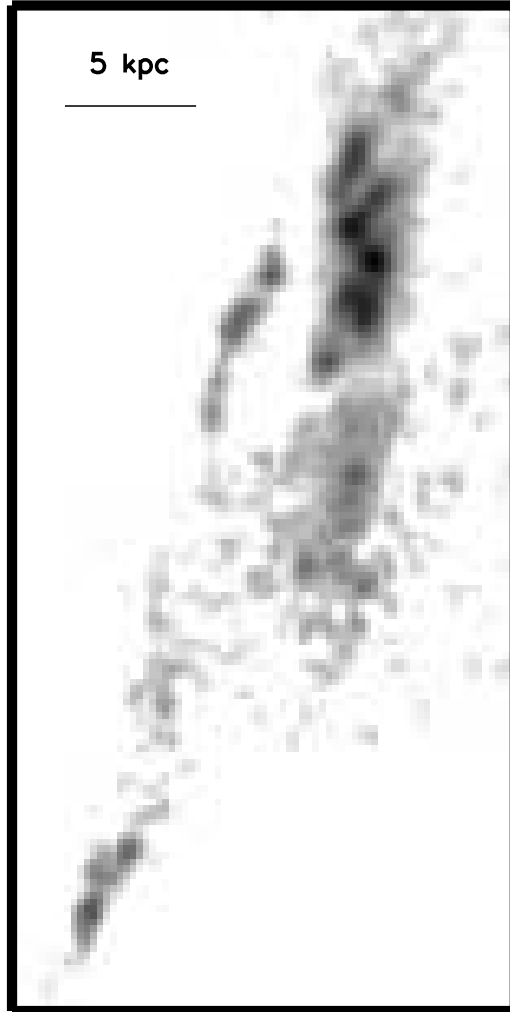


Figure 2.3 Close-up view of the criss-crossing filaments in the FUV showing both of the bright blobs. The brightest portions of the filaments break up into young UV-bright super star clusters.

2.4 Discussion

2.4.1 Origin and Power Source of Filaments

A number of very specific scenarios were put forward by Fabian et al. (2001) to explain the origin of the SE filament, taking into account that 4C 26.42 is in motion within the gravitational potential of the Abell 1795 cluster (Crawford et al. 2005;

Oegerle & Hill 2001; Rodríguez-Martínez et al. 2006): (a) a cooling wake, produced by a cooling flow occurring around the moving cD galaxy (as in NGC 5044; David et al. 1994), (b) a “condensation trail” produced by the ram pressure of the radio source passing through the multiphase medium of the ICM and ISM of the host galaxy, (c) evaporation of cold gas ram-pressure stripped from the cD galaxy, and (d) an accretion wake produced by the gravitational focussing effects of the moving cD galaxy on the ICM (e.g., Sakelliou et al. 1996).

Scenario (d) requires that the accreting ICM be gravitationally focused by the cD galaxy and cool into a wake. However, the relatively large sound speed of the hot gas makes it unlikely that this process alone can account for the presence of the long, thin, X-ray filament. In scenario (c), the material making up the filaments is ISM stripped from the cD galaxy. The large mass of hot gas in the filaments, $\sim 5 \times 10^9 M_{\odot}$ (Fabian et al. 2001), and thin geometry of the filaments are hard to explain in this scenario. However, this does not exclude the possibility that *some* of the gas outside the cD galaxy is produced in this way (e.g. the broad base of the $H\alpha$ filaments). Scenario (b) also presents some problems. As argued by Fabian et al. (2001), it seems unlikely that the cD galaxy plunging through the ICM would result in cooling, rather than heating, of the multiphase medium. Moreover we see no obvious connection in the data between the radio jets of 4C 6.42 and the long filaments.

By process of elimination, these arguments seem to favor scenario (a). The very thin geometry of the $H\alpha$ filaments points to highly non-linear runaway cooling in this region. Potentially contributing heating/ionization sources in the filaments include (i) the central AGN, (ii) hot young stellar population outside the cD galaxy, (iii) X-rays from the ICM itself, (iv) heat conduction from the ICM to the colder filaments, (v) shocks and turbulent mixing layers, and (vi) collisional heating by cosmic rays.

Arguments based on the AGN energetics and the line ratios in and out of the central region suggest that the AGN is not strongly influencing the ionization of the material much beyond the central region ($R \lesssim 6$ kpc). The long, thin geometry of the filaments and their quiescent velocity field (Crawford et al. 2005) seem to rule out ionization by shocks and/or turbulent mixing layers, while the relative weakness of high-ionization lines suggests that ionization by the X-ray ICM is also a small contributor. This leaves scenarios (ii), (iv), and (vi) as the most plausible explanations for the dominant heating mechanism in the filaments.

The presence of FUV point sources in the filaments (Figure 2.3) lends support to scenario (ii), but is there enough star formation to account for the observed $H\alpha$ emission? To try to answer this question, we compare the FUV and $H\alpha$ emission. Figure 2.4 shows the average $H\alpha$ and FUV surface brightnesses of the brighter features defined in Figure 2.3. The $H\alpha$ and FUV luminosities of these features are listed in Table 2.1. Assuming that the FUV and $H\alpha$ star formation rate prescriptions of Kennicutt (1998) derived from the global properties of star-forming galaxies also apply individually to these features (we return to this assumption below), we find that the $H\alpha$ and FUV surface brightnesses and luminosities of these features imply star formation rate surface densities and star formation rates which are generally consistent to within a factor of ~ 2 of each other. (The only exceptions are the arc and the NE and NW extensions, which are underluminous in $H\alpha$; this could be due to a lack of gas in these regions or other forms of continuum emission process. A detailed analysis of the central region using all three FUV bands of ACS/SBC (PI: W. Sparks) is in preparation.) Under this assumption, the total $H\alpha$ and UV-determined star formation rates are $\lesssim 1.7 - 2.7 M_{\odot} \text{ yr}^{-1}$, with $\sim 0.2 - 0.5 M_{\odot} \text{ yr}^{-1}$ ($\sim 15 - 25\%$) contained in the filaments (Table 2.1). These numbers are ~ 2 orders of magnitude smaller than the predicted *Chandra*- and *XMM*-derived integrated mass

deposition rates from the inner ICM (Ettori et al. 2002; Peterson et al. 2003).

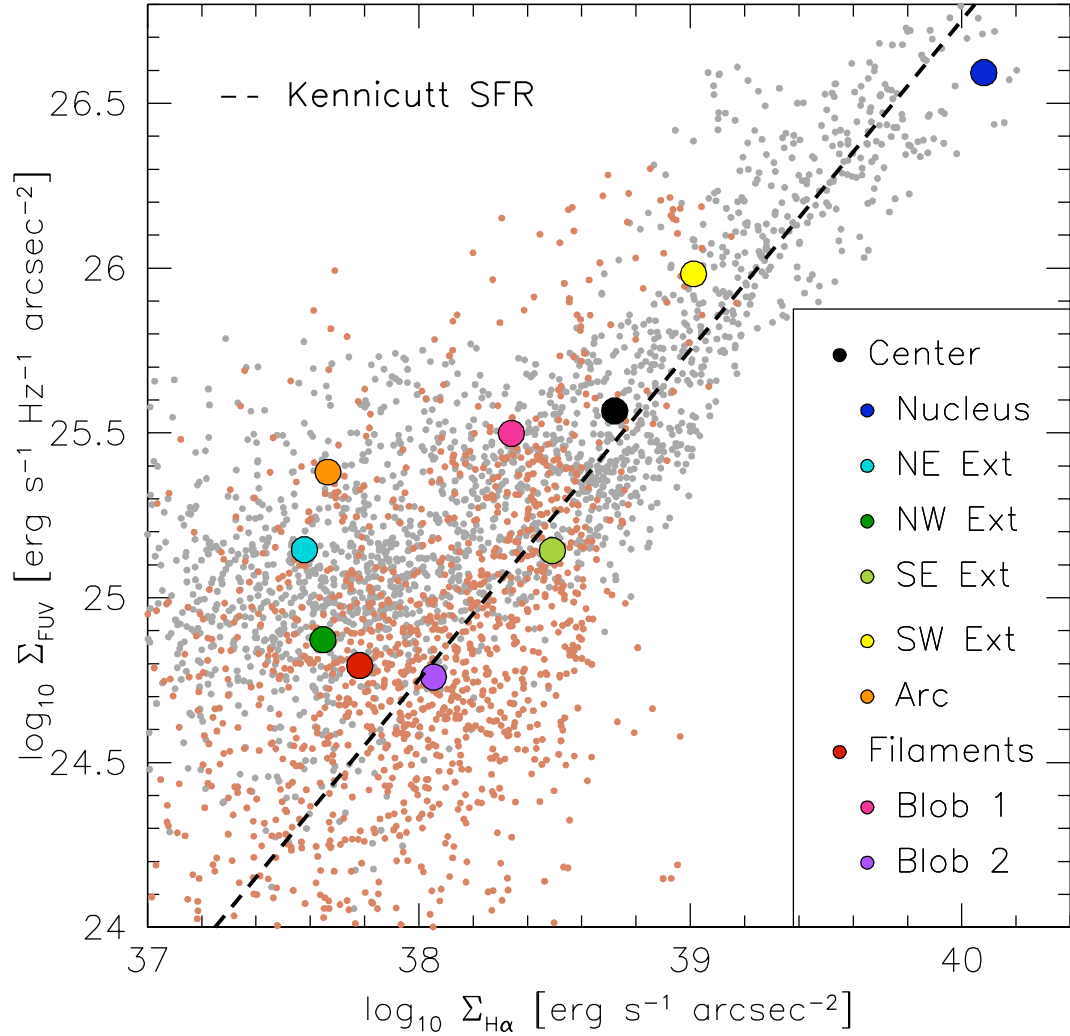


Figure 2.4 FUV surface brightness, Σ_{FUV} , versus $H\alpha$ surface brightness, $\Sigma_{H\alpha}$, in Abell 1795. The dashed line represents the expected relation between the global $\Sigma_{H\alpha}$ and Σ_{FUV} for star-forming galaxies (Kennicutt 1998). The larger symbols show the average surface brightness over the brighter features defined in Figure 2.3. The background distribution of points shows the 2×2 pixel-by-pixel surface brightness measurements for the central region (grey) and filaments (light red).

The integrated $H\alpha$ and FUV quantities discussed so far do not tell the full story: Large spatial variations of the FUV/ $H\alpha$ ratio are seen on smaller scale (see lower middle panel of Figure 2.3 and pixel-to-pixel surface brightness measurements of

Figure 2.4). These spatial variations may be due to a number of effects, including differential dust extinction, variations in star formation history (SFH: age of burst, decay time scale) or initial mass function (IMF), complex geometry of the gas relative to the ionizing stars, and contributions from non-stellar processes to the FUV and $H\alpha$ emission. Extinction corrections would boost the FUV fluxes relative to $H\alpha$ and therefore could account for regions with anomalously small FUV/ $H\alpha$ ratios. Published data on the filaments suggest relatively modest extinctions, however (e.g., Crawford et al. 2005). Variations in the SFH or IMF change the relative importance of ionizing and non-ionizing stars and may account for variations in both directions of the FUV/ $H\alpha$ flux ratio. Our data do not provide strong constraints on these parameters. Geometrical effects are undoubtedly important in some regions, particularly in blobs #1 and #2, where spatial offsets of $\sim 1\text{--}2$ kpc are visible between the $H\alpha$ and FUV emission centroids. In these blobs, the Kennicutt (1998) prescriptions may severely underestimate the number of FUV-bright stars needed to account for the $H\alpha$ emission; processes other than photoionization by hot stars appear needed to account for the observed $H\alpha$ at these locations (the recombination time scale is at least an order of magnitude shorter than the dynamical time scale to move $\sim 1\text{--}2$ kpc, unless the density of the $H\alpha$ filaments is much less than $\sim 1\text{ cm}^{-3}$).

As mentioned in §2.3, additional heating sources also appear needed to explain the unusually strong low-ionization lines detected in the blobs and in between them (e.g., Crawford et al. 2005; Hu et al. 1985, ; Figure 2.3). Two heating processes remain viable: (iv) heat conduction from the ICM to the colder filaments and (vi) collisional heating by cosmic rays. The relative importance of these processes critically depends on the strength of the magnetic field in the filaments. Strong magnetic fields could shield the cooling ICM gas from re-heating by conduction with the hot ICM (scenario (iv)), creating long tubes of cool, dense gas. Runaway star formation

would take place along these magnetic field lines, where the gas is cooling and condensing to high enough density to become Jeans unstable. The long, thin geometry of the H α SE filaments and detection of embedded FUV-bright stellar clusters in these filaments are consistent with this picture.

Ferland et al. (2008, 2009) have recently examined the question of the importance of heating by energetic particles or dissipative magnetohydrodynamic (MHD) waves in the central nebulae of massive clusters. The energetic particles contributing to the heating of the filaments in this scenario may either be produced in-situ by MHD processes or conducted in from the surrounding intracluster medium. Given our previous discussion, we speculate that the optical emission in the SE filaments of Abell 1795 may naturally be explained by these heating processes. The magnetic field in the filaments may represent residual magnetic field originally associated with the radio galaxy but now entrained in the ICM flow. If this is the case, the crisscrossing geometry of the SE filaments may reflect precession of the radio jets or the orbital motion of the cD galaxy in the cluster potential.

Finally, we end with a cautionary note: Our data do not provide quantitative constraints on the strength of the purported ICM magnetic field. The possibility of runaway star formation unaided by magnetic field cannot be ruled out. In fact, the filaments seen in Abell 1795 shares a stunning morphological resemblance with the narrow cold streams seen feeding galaxies in recent high-resolution numerical simulations of the early universe (e.g., Ceverino et al. 2010).

2.5 Concluding Remarks

Using deep, high-resolution $H\alpha$, $[N II] \lambda 6584$, and FUV data, we have discovered that the SE filament in Abell 1795 is in fact two intertwined filaments of ionized hydrogen. The most plausible origin for these filaments is a wake of cooling ICM behind the moving cD galaxy in Abell 1795. The narrowness of the strands suggest highly non-linear runaway cooling of the ICM. Their tangled morphology suggests that the infalling gas may be interacting with stronger than average magnetic field, allowing for less efficient energy conduction and faster cooling in this region. We observe knots of UV-bright point sources along these filament, indicating star formation at a rate of $\sim 0.5 M_{\odot} \text{ yr}^{-1}$ in the filaments. The large spatial variations of the FUV/ $H\alpha$ ratio and enhanced low ionization lines suggest that O-star photoionization is not the sole source of heating of this gas; collisional heating by energetic particles is another likely contributor. A deeper understanding of the origin of the filaments of Abell 1795 will require detailed MHD modeling and observations to constrain the purported magnetic field, both of which are beyond the scope of the present chapter. It is also not clear yet whether this scenario applies to cooling flow clusters in general. We plan to address this issue in upcoming chapters using a representative set of massive clusters.

Table 2.1 Luminosities, flux ratios and inferred star formation rates in the central region of Abell 1795.

Region	$L_{H\alpha}$ [$10^7 L_{\odot}$]	$L_{[NII]}$ [$10^7 L_{\odot}$]	L_{FUV} [$10^7 L_{\odot}$]	[N II]/H α	FUV/H α	SFR(H α) ^(a) $M_{\odot} \text{ yr}^{-1}$	SFR(UV) ^(a) $M_{\odot} \text{ yr}^{-1}$
Total	5.49	1.97	8.07	0.36	14.7	<1.67	<2.66
SE filaments	0.72	0.26	1.47	0.36	20.3	0.22	0.48
Blob 1	0.25	0.09	0.70	0.38	28.4	0.08	0.23
Blob 2	0.16	0.09	0.16	0.53	10.0	0.05	0.05
Central region	4.77	1.72	6.61	0.36	13.8	<1.45	<2.18
Nucleus	0.12	0.10	0.06	0.81	4.4	<0.04	<0.02
NE extension	0.05	0.00	0.36	0.00	73.0	0.02	0.12
NW extension	0.05	0.00	0.16	0.00	33.3	0.02	0.05
SE extension	0.50	0.13	0.44	0.26	8.9	0.15	0.15
SW extension	1.00	0.48	1.85	0.48	18.5	0.30	0.61
Arc	0.03	0.00	0.28	0.00	102.8	0.01	0.09

^(a) Star formation rates derived using the prescriptions in Kennicutt (1998) assuming all of the H α and UV emission, including that from the nucleus, is due to star formation.

Chapter 3

On the Origin of the Extended $H\alpha$ Filaments in Cooling Flow Clusters

3.1 Introduction

The high densities and low temperatures of the intracluster medium (hereafter ICM) in the cores of some galaxy clusters imply massive amounts of gas cooling radiatively out of the ICM. Early studies (see review by Fabian 1994) suggested that cooling flows on the order of $100\text{--}1000 M_{\odot} \text{ yr}^{-1}$ should be depositing massive amounts of cold gas onto the brightest cluster galaxy (hereafter BCG) in the cluster core. The lack of evidence for such large amounts of cold molecular gas or young stars is often referred to as the “cooling flow problem”. More recent studies suggest that the cooling region is much smaller than previously thought (Peres et al. 1998), which implies overall lower estimates on the mass deposition rate. Additionally, it is now generally accepted that some form of heating balances the radiative cooling, leading to cooling

flow rates on the order of $1\text{--}10 M_{\odot} \text{ yr}^{-1}$. Mechanical and radiative feedback from AGN and starbursts (e.g., Peterson & Fabian 2006; Veilleux et al. 2005), gas sloshing in the cluster core (e.g., Zuhone & Markevitch 2009), merger shocks (e.g., Randall et al. 2002) and conduction from the surrounding ICM (e.g., Voigt & Fabian 2004) have all been suggested as possible contributors to ICM heating. However, the relative importance of each process remains unclear.

The presence of optical line-emitting nebulae, found primarily in cooling flow clusters, is a clue that cooler ($\sim 10^4$ K) gas coexists with the ICM and that cooling flows may not be entirely ruled out (Crawford et al. 1999; Hatch et al. 2007; Heckman et al. 1989; Hu et al. 1985; Jaffe et al. 2005). However, while several intriguing ideas have been put forward, the origin of this gas and the mechanism for heating it are, as yet, unknown. While the presence of cool gas could be attributed to the purported cooling flow, one would then naively expect a relatively symmetric geometry and a strong connection of optical emission lines with X-ray properties. However, this is not generally the case. Crawford et al. (2005) investigate a specific scenario, the extended $H\alpha$ filament in Abell 1795, and suggest as an explanation a cooling wake, produced by a symmetric cooling flow falling onto the brightest cluster galaxy (hereafter BCG) which has a high relative velocity at the center of the cluster. Oegerle & Hill (2001) find that $\sim 15\%$ of BCGs are moving with a high peculiar velocity, so an asymmetric distribution of warm gas in this fraction of clusters would be relatively straightforward to explain in this context. Potentially contributing heating/ionization sources in the filaments include (i) the central AGN, (ii) hot young stellar population outside the cD galaxy nucleus, (iii) X-rays from the ICM itself, (iv) heat conduction from the ICM to the colder filaments, (v) shocks and turbulent mixing layers, and (vi) collisional heating by cosmic rays (Crawford et al. 2005; Ferland et al. 2009).

In star forming regions, the presence of ionized hydrogen is a prime indication of the rate and location of star formation. While several cooling flow clusters have been observed to have non-zero star formation rates at their center, based on UV (Hicks & Mushotzky 2005) and infrared (O’Dea et al. 2008) observations, it is not immediately clear whether newly formed stars are fully responsible for the flux and morphology of the observed $H\alpha$ emission. Indeed, there has been very little work done on the spatial correlation between the star forming and warm components in cooling flow cluster centers. What *has* become clear from recent studies is that, in general, the measured star formation rate in the BCG is consistently less than the spectroscopically determined X-ray cooling rate for the cluster by a factor of 3-10 (e.g., O’Dea et al. 2008; Rafferty et al. 2006), implying that not all of the cooling gas is turning into stars with a Salpeter (1955) IMF.

A major problem standing in the way of an explanation of these filaments is that there are still only a small number of known cases with clearly extended emission beyond the nucleus of the BCG. This is due to the paucity of narrow-band filters which can be tuned to cosmological redshifts. Attempts have been made to quantify the fraction of BCGs which exhibit $H\alpha$ emission using the Sloan Digital Sky Survey (e.g., Edwards et al. 2007). However, spectroscopic studies usually only tell us about the very center of the BCG, which can be bright in $H\alpha$ if an AGN is present. What is needed is a deep, wide-field, narrow-band survey of clusters of various richness in order to assess the ubiquity, extent, and topology of the warm gas. Some progress has been made towards this end by Jaffe et al. (2005), using the Taurus Tunable Filter (TTF; Bland-Hawthorn & Jones 1998). The use of a tunable filter allows the observer to tune to a large range in wavelengths with a narrow bandwidth ($\sim 10\text{\AA}$). The ability to tune the wavelength is particularly useful when observing cooling flow clusters, of which there are very few in the local Universe.

In the pilot study leading to this survey (§2), we observed Abell 1795 in $H\alpha$ with the Maryland Magellan Tunable Filter (hereafter MMTF; Veilleux et al. 2010) in $H\alpha$. The well-known southeast filament which extends ~ 50 kpc from the BCG was found to be, in fact, two separate thin strands. These thin filaments were resolved into chains of point sources in the far-UV with the *Hubble Space Telescope* (*HST*) Advanced Camera for Surveys Solar Blind Channel. We suggested that these strands of $H\alpha$ were, in fact, a cooling wake produced by the cooling flow falling onto a cD galaxy which is plowing through the center of the cluster. As the gas cools, it collapses into thinner filaments, eventually leading to star formation which will ionize the gas. The thinness of the filaments suggests that magnetic fields are likely important to prevent turbulence from erasing them, but this is just speculation without any direct evidence of a strong magnetic field in the filaments. Although it is likely more complicated than this (we observe higher-than-expected $[N II]/H\alpha$ ratios, and a slight spatial offset between the UV and $H\alpha$), this scenario can explain the general structure of the $H\alpha$ complex.

In order to have a more complete picture of the extended $H\alpha$ emission in galaxy clusters, we have undertaken a survey of 23 clusters with a wide variety of properties using the MMTF. In the following section we describe our sample selection, as well as the acquisition and analysis of the data. In §3.3, we present the results of the analysis and in §3.4 discuss the various implications of these results. Finally, in §3.5 we present a summary of the results. Throughout this chapter, we assume the following cosmological values: $H_0 = 73 \text{ km s}^{-1} \text{ Mpc}^{-1}$, $\Omega_{matter} = 0.27$, $\Omega_{vacuum} = 0.73$.

3.2 Data Collection and Analysis

In order to have a more complete picture of cool core clusters, we have undertaken a multi-wavelength survey of 23 cooling flow clusters. From an initial sample size of 232 clusters, which cover 2 orders of magnitude in dM/dt and with X-ray temperatures ranging from 1-12 keV, (full sample from White et al. 1997) we enforced the following cuts: $\delta < +35^\circ$ and $0.025 \leq z \leq 0.092$. These cuts ensured that (1) the cluster was visible with Magellan, (2) the appropriate blocking filters were available to observe redshifted $H\alpha$, and (3) the cluster angular size did not exceed that of MMTF ($\sim 30'$). These two cuts removed a total of 44 and 62 clusters from the full sample, respectively, leaving a total of 126 observable clusters. From this list, we selected 23 clusters to cover the full range of properties, from very rich clusters with high cooling rates (e.g., Abell 1795, Abell 2029) to low-density clusters with little or no cooling flow (e.g., Ophiuchus, Abell 3376). A summary of these properties for our sample clusters is given in Table 3.1. As is shown in Table 3.1, the range in classical cooling rates for this sample is from 6.3–431 $M_\odot \text{ yr}^{-1}$, which means that, while we cover a large range in properties, we are examining only cooling flow clusters. This selection criteria should produce a higher fraction of line-emitting BCGs compared to an un-biased cluster sample (see Edwards et al. 2007).

For these 23 clusters, we have data at $H\alpha$ (MMTF; 23/23), red continuum (MMTF; 23/23), near-IR (2MASS; 23/23), UV (*GALEX*, *XMM-OM*; 21/23) and X-ray (*Chandra*; 19/23). For those clusters hosting a radio galaxy, we have also extracted VLA 1.4 GHz fluxes from the NVSS (Condon et al. 1998) survey (17/23). The availability of these data are summarized in Table 3.1.

In the following subsections, we describe in detail the acquisition and reduction of these data.

Table 3.1 Sample of 23 cooling flow clusters with MMTF H α imaging

Name	z	E(B-V)	T_X	\dot{M}_{class}
(1)	(2)	(3)	(4)	(5)
Abell 0085	0.0557	0.038	6.5	108
Abell 0133	0.0569	0.019	3.5	110
Abell 0478	0.0881	0.517	6.8	736
Abell 0496	0.0329	0.132	4.8	134
Abell 0644	0.0704	0.122	6.5	136
Abell 0780	0.0539	0.042	4.7	222
Abell 1644	0.0475	0.069	5.1	12
Abell 1650	0.0846	0.017	5.1	122
Abell 1795	0.0625	0.013	5.3	321
Abell 1837	0.0691	0.058	2.6	12
Abell 2029	0.0773	0.040	7.4	431
Abell 2052	0.0345	0.037	3.4	94
Abell 2142	0.0904	0.044	10.1	369
Abell 2151	0.0352	0.043	2.9	166
Abell 3158	0.0597	0.015	5.3	9.6
Abell 3376	0.0597	0.056	3.5	6.3
Abell 4059	0.0475	0.015	-	-
Ophiuchus	0.0285	0.588	8.6	41
Sersic 159-03	0.0580	0.011	2.4	288
Abell 2580 ^a	0.0890	0.024	4.3	95
Abell 3389 ^a	0.0267	0.076	2.0	22
Abell 0970 ^b	0.0587	0.055	4.1	20
WBL 360-03 ^b	0.0274	0.028	1.8	10

(1) - Cluster name

(2) - NED redshift of BCG (<http://nedwww.ipac.caltech.edu>)

(3) - Reddening due to Galactic extinction from Schlegel et al. (1998)

(4) - Cluster X-ray temperature (keV) from White et al. (1997)

(5) - Classical cooling rates ($M_{\odot} \text{ yr}^{-1}$) White et al. (1997)

^a - No available Chandra data

^b - No available Chandra, GALEX or XMM-OM data

3.2.1 H α : MMTF

The MMTF has a very narrow bandpass ($\sim 5\text{--}12\text{\AA}$) which can be tuned to any wavelength over $\sim 5000\text{--}9200\text{\AA}$ (Veilleux et al. 2010). Coupled with the exquisite image quality at Magellan and the wide field of the Inamori-Magellan Areal Camera & Spectrograph (IMACS), this instrument is ideal for detecting emission-line filaments in distant clusters. During 2008-09, we observed all 23 clusters at both H α ($\lambda=6563\text{\AA}$) and continuum ($\pm 60\text{\AA}$), for a total of 20 minutes each. If H α was detected in a 20-minute exposure, it was followed up for an additional 40 minutes at each wavelength. The typical image quality for these exposures was $0.6 \pm 0.2''$

These data were fully reduced using the MMTF data reduction pipeline¹, which performs bias subtraction, flat fielding, sky line removal, cosmic ray removal, astrometric calibration and stacking of multiple exposures (following Bland-Hawthorn & Jones 1998; Veilleux et al. 2010). The continuum image was then PSF and intensity matched to the narrow-band images to allow for careful continuum subtraction. The stacked images were calibrated using spectrophotometric standards from Oke (1990) and Hamuy et al. (1994, 1992). The error associated with our absolute photometric calibrations is $\sim 15\%$, which is typical for tunable filters and spectrographs. Finally, the data were corrected for Galactic extinction, following Cardelli et al. (1989) using reddening estimates from Schlegel et al. (1998). We do not attempt to correct for intrinsic extinction since the dust content of the optical filaments is not well known. All of these procedures are described in detail in Veilleux et al. (2010).

For systems with complicated morphologies, H α fluxes were measured by creating (by eye) a region which generously traced the H α emission and calculating the total signal within this region. For more symmetric morphologies, a circular aperture

¹<http://www.astro.umd.edu/~veilleux/mmtf/datarred.html>

centered on the emission peak was used, with the radius chosen to contain all of the obvious emission. Our measured $H\alpha$ fluxes (see Table 3.5) agree well with those in the literature (e.g., Cowie et al. 1983; Edge 2001; Jaffe et al. 2005; Owen et al. 1995) for the 12 systems with previously published data. In 9 systems we measure slightly higher ($\sim 1.7\times$) total flux, most likely due to our better sensitivity and larger field-of-view. In all other cases, the published “ $H\alpha$ ” flux also include a contribution from [N II] $\lambda\lambda$ 6548, 6583 and is therefore overestimated. In all cases, the $H\alpha$ emission measured from our data is not contaminated by [N II] emission.

3.2.2 Near-UV: *GALEX* and *XMM-OM*

One possible source of $H\alpha$ ionization in these clusters is photoionization from hot, young stars. In this scenario we would expect to see associated UV emission, perhaps with filamentary morphology as well. In order to properly assess if this is the case, we have used archival *GALEX* (1350-1750Å, 1750-2800Å) and *XMM-OM* (1820-2320Å, 2078-2517Å, 2595-3215Å) data for most of the clusters in our sample. The *GALEX* data for Abell 1795 comes from our own program (GALEX GI Cycle 5 Program 31; PI Veilleux). These data were corrected for Galactic extinction, following Cardelli et al. (1989) using Galactic reddening estimates from Schlegel et al. (1998).

In order to determine the star formation rate (SFR) from the NUV flux, we follow the prescription described in Kennicutt (1998). This technique assumes that $SFR \propto F_\nu$ with no dependence on wavelength (F_ν is flat) over the range of 1500-2800Å. In Figure 3.1, we confirm that this assumption is roughly valid for the clusters in our sample and, thus, if dust is present it does not follow the galactic reddening law. For 18 clusters, we have *GALEX* near-UV (2267Å) data, while the remaining 3 have *XMM-OM* UVW1 (2905Å) data. The difference in flux that we predict between these filters (from Figure 3.1) is $\sim 1.3\times$. Thus, we proceed with merging these two

sources of UV data with the caveat that UV fluxes for Abell 0478, 0496 and 1650 may be $\sim 30\%$ too high.

Accompanying J-band images were also obtained from 2MASS in order to remove the expected NUV emission from the old stellar population. Motivated by the techniques described in Hicks & Mushotzky (2005) and Hicks et al. (2010), we attempt to remove the NUV contribution from old stellar populations, which we infer from the J-band data. The relationship between the GALEX NUV and 2MASS J-band fluxes follow a powerlaw:

$$\log_{10} L_{NUV} = C_1 + C_2 \log_{10} L_J \quad (3.1)$$

Hicks et al. define a non-star forming control sample in order to calibrate this relationship, consisting of 17 cluster ellipticals and 22 BCGs in clusters without measurable cooling flows. The BCGs in this control sample cover a similar range in J-band luminosity and redshift to the clusters in our sample. Hicks et al. (2010) find $C_1 = -0.85 \pm 0.016$ and $C_2 = 0.89 \pm 0.045$, with a scatter of 0.08, based on fluxes measured in $7''$ apertures. Since we are interested in detecting extended emission, we instead use a $30''$ aperture, which has the net effect of changing the zero-point of this relation (due to the NUV-J color gradient). Thus, we adjust the zero-point by hand so that it passes through the points with the lowest NUV/J ratios. We find $C_1 = -0.55$ and note that the observed scatter about this fit matches well that quoted by Hicks et al. (2010). Fig. 3.2 shows this fit, along with that found by Hicks et al. (2010), for the BCGs in our sample. Using this relation, we scaled the measured J-band fluxes to obtain the NUV contribution from the old stellar population, and then subtracted this from the measured NUV flux. Our value of C_1 is slightly larger than that of Hicks et al. (2010), due to our use of a larger aperture. We show in the right-hand panel of Fig. 3.2 that, beyond the $7''$ aperture used by Hicks, the NUV/J ratio is higher at all radii out to $30''$. Thus, a slight increase in C_1 is justified.

We do not attempt to correct for intrinsic extinction, due to the fact that not all of our clusters have reddening estimates, thus the lower envelope in Fig. 3.2 could also contain dusty, star forming galaxies. However, from Crawford et al. (1999), we find that the typical intrinsic extinction in BCGs with strong H α emission is $E(B-V) = 0.29 \pm 0.135$. This would induce a scatter of 0.5 in the NUV-J relation. Since the measured scatter is much lower (0.08), we propose that the majority of the galaxies used in the Hicks et al. (2010) NUV-J relation are relatively dust-free. Furthermore, it is unclear how the dust is distributed in the BCG (e.g., Lauer et al. 2005) and, thus, any intrinsic extinction correction would require a significant amount of guesswork.

3.2.3 X-Ray: *Chandra*

Archival data from the *Chandra X-ray Observatory* were retrieved for 19 of our 23 sample clusters. These data were reprocessed with CIAO (version 4.1.2) and CALDB (version 4.1.1) using the latest time-dependent gain adjustments and maps to create new level 2 event files. Due to the large angular extent of the clusters in our sample, we were required to construct blank-sky background event files, using the ACIS blank-sky background database, to properly account for background flux. The new level 2 event files were cleaned for flares, using the *lc_clean* routine, by examining the light-curve and removing any spurious bursts in intensity. These data cleaning and calibration procedures are all outlined in detail in the CIAO science threads².

In order to separate any filaments or interesting morphology from the X-ray halo, we performed an unsharp masking technique on each image, subtracting a 10'' Gaussian smoothed image from a 1.5'' Gaussian smoothed image. The resulting image highlights any fine structure in the X-ray morphology.

²<http://cxc.harvard.edu/ciao/threads/>

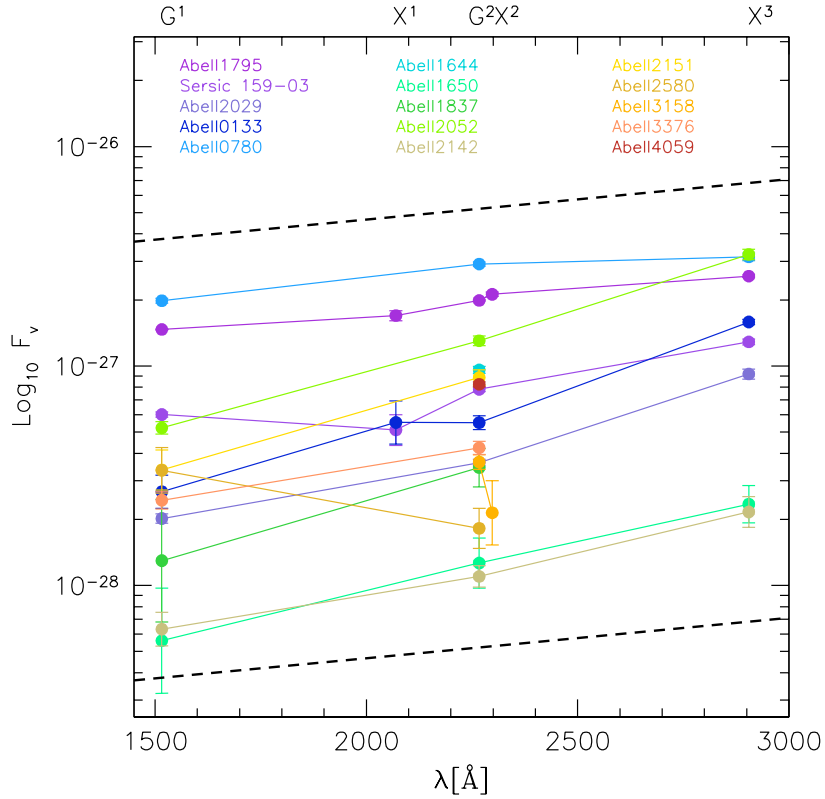


Figure 3.1 UV SEDs for 15 clusters in our sample with observations at multiple wavelengths. All fluxes have been corrected for Galactic extinction. The two *GALEX* filters are denoted by G^1 and G^2 , while the three *XMM-OM* filters are denoted by X^1 , X^2 and X^3 . The dashed lines represent the mean SED slope. These SEDs are sufficiently flat to justify merging our 18 *GALEX* NUV (2267\AA) and 3 *XMM-OM* UVW1 (2905\AA) observations into a single near-UV sample.

For each cluster, background-subtracted spectra were extracted using *dmextract*. Updated response files were created using *mkacisrmf* and *mkwarf*, following the CIAO science threads. Counts were grouped into bins with 20 counts per bin, over the range 0.3 to 11.0 keV. Spectra were extracted in a variety of regions to better understand the relationship between the ICM and the $H\alpha$ emission. These regions are described below, followed by a description of the spectral modeling which we apply to these spectra.

Radial Profiles

For all clusters, spectra were extracted from a series of concentric annuli. The maximum annulus was chosen by eye (typically the largest allowable in the CXO field-of-view) and then the interior annuli were chosen iteratively (following Sun et al. 2009) with $r_{out}/r_{in} = 1.25\text{--}1.6$ so that each annulus contained a minimum of 10,000 counts. This choice of spacing allows for a reliable deprojection and fit to the spectra. The innermost annulus was chosen to have an inner radius of 2 pixels, to exclude any contribution from the AGN. The data in this inner region of 2-pixel radius is used to identify possible AGN emission.

Filaments

In order to properly investigate any possible connection between the ICM and the presence of $H\alpha$ filaments, we also extract X-ray spectra in regions where we detect $H\alpha$ emission. A mask was created from the MMTF images by first registering them to the CXO images using the IRAF *wregister* task. The typical error involved in this process is dependent on the relative astrometric calibrations, which was typically a fraction of a pixel, or $\sim 0.1''$. The registered image was then smoothed by $1''$ using a Gaussian kernel. Finally, all pixels with a flux greater than $3\text{-}\sigma$ above the background and within $R_{H\alpha}$ (defined as the outermost radius of $H\alpha$ emission, measured from the peak of the $H\alpha$ emission, see §3.3.1) were included in the mask. We extracted spectra in four different regions: (1) $0 < r < R_{H\alpha}$, coincident with $H\alpha$, (2) $0 < r < R_{H\alpha}$, anti-coincident with $H\alpha$, (3) $0.3R_{H\alpha} < R < R_{H\alpha}$, coincident with $H\alpha$, (4) $0.3R_{H\alpha} < R < R_{H\alpha}$, anti-coincident with $H\alpha$. These spectra allow for a direct comparison between X-ray derived properties inside and outside of the $H\alpha$ filaments, both near the center and at larger radii. An example of the on-filament extraction regions is shown in Figure 3.3, for Abell 1795 and Abell 0496.

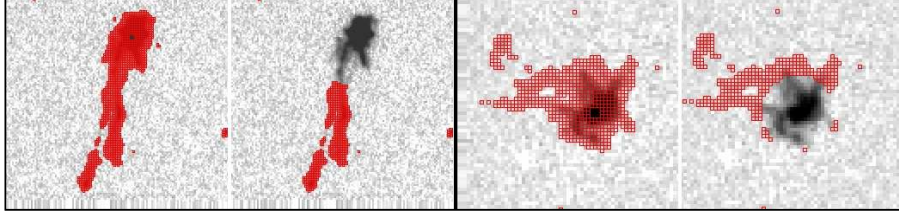


Figure 3.3 Examples of the on-filament extraction area (shown in red) for Abell 1795 (left) and Abell 0496 (right). The left-most frame in each pair covers the full radial range, while the right-most covers the range $0.3R_{H\alpha} < r < R_{H\alpha}$. The off-filament extraction area contains all unmarked pixels in the same radial range.

Spectral Modeling

In order to derive physical quantities from the X-ray spectra, we used the XSPEC spectral fitting package (Arnaud 1996). As mentioned above, spectra in radial annuli have also been extracted. This allows for the computation of various parameters such as T_X and n_e as a function of radius. Since the emission in any given annulus is a combination of emission at that radius and also at larger radii seen in projection, we need to deproject the data in each radial bin. We do this using two different techniques: direct spectral deprojection (DSDEPROJ; Russell et al. 2008) and the PROJCT routine in XSPEC. We find DSDEPROJ to yield more stable radial profiles, in agreement with Russell et al. (2008), who showed that PROJCT produces highly fluctuating radial profiles when applied to a spectrum that represents gas at multiple temperatures. Thus the majority of the analysis uses the results from this deprojection. However, it should be mentioned that all of the relevant quantities which we derive from these profiles are robust to the spectral deprojection method used. Along with the spectral deprojection, we used a photoelectric absorption model (PHABS) multiplied by a model for thermal bremsstrahlung emission from a hot diffuse gas (MEKAL). The elements were assumed to be present in the Solar ratios, as measured by Anders & Grevesse (1989). The free parameters for this

combination of models are the column density of hydrogen, N_H , the plasma temperature in keV, T_X , the metal abundance of the plasma, Z , and the normalization of the model, which is directly related to the electron density in the plasma, n_e . The model normalization (N_{MEKAL}) is related to the electron density by:

$$N_{MEKAL} = \frac{10^{-14}}{4\pi[D_A(1+z)^2]} \int n_e n_H dV \quad (3.2)$$

where D_A is the angular diameter distance to the source, in cm, and dV is the volume of the emitting region. We assume that the X-ray halo is spherical, in order to make the volume calculation straightforward. In order to determine the electron density inside and outside of the ionized filaments, we also need to assume something about their thickness. We discuss this problem further in a later section.

Finally, in order to determine the mass deposition rate in the cooling flow (\dot{M}_{spec}), we also apply a second set of models to the radially-binned spectra. This new set of models consists of the same deprojection and photoelectric absorption mentioned above, multiplied by the combination of a thermal plasma (MEKAL) and a second plasma component that is cooling (MKCFLOW). The MKCFLOW model has two temperature parameters, high T and low T, which we lock to the temperature of the plasma and to 0.1 keV, respectively. The choice of the low temperature is arbitrary - we simply need it to be lower than the Chandra detection limit (~ 0.5 keV) so that this represents gas that has cooled out of the X-ray regime. The metal abundance in the cooling gas is also required to be the same as the plasma. Thus, the only free parameter in this new component is the normalization, which is precisely the spectrally-determined cooling flow rate, \dot{M}_{spec} .

3.2.4 1.4 GHz Radio: NVSS

The total 1.4 GHz radio flux at the center of a cluster is a useful diagnostic of AGN activity. For the 20 clusters with $\delta > -40^\circ$ in our sample, we used the 1.4 GHz fluxes measured from the NRAO VLA Sky Survey (NVSS; Condon et al. 1998).

3.3 Results

3.3.1 Warm Ionized Filaments

This survey is the largest sample of cooling flow clusters with high-resolution, narrow-band imaging to date. The success of this survey has been striking, with multiple extended filaments seen in 8/23 clusters and slightly extended or nuclear emission seen in an additional 7/23 clusters. The remaining 8 clusters have no detectable $H\alpha$ emission. This detection rate of $\sim 65\%$ is consistent with the value of 71_{-14}^{+9} found by Edwards et al. (2007) for BCGs in cooling flow clusters (for BCGs in both cooling and non-cooling clusters, Edwards et al. find the fraction to be $\sim 15\%$). Figure 3.4 shows the unsharp masked X-ray and archival UV data, along with the new MMTF continuum and $H\alpha$ images, centered on the BCG. Upon inspection of these images, the following trends are immediately evident:

- There is a strong correlation between the X-ray and $H\alpha$ morphology. Clusters with ionized filaments tend to have structure in the X-ray. This structure is brightest at lower energies (0.5-2 keV, see Figure 3.5), suggesting that the optical filaments live in or near cooler X-ray structures.
- There does not appear to be a correlation between the presence of filaments and the presence of other galaxies near the BCG. In fact, Abell 2151 and

Abell 2029 each have one or more significant companions within the optical radius of the BCG but exhibit no detectable $H\alpha$ emission. Of the 7 clusters with extended $H\alpha$ filaments, only 3 (Abell 0478, Abell 1644, Abell 2052) have significant companions within the optical radius of the BCG. In a select few cases, the direction of the detected filaments may correlate with the position of nearby galaxies (e.g., Abell 0478, Abell 1644).

- The observed warm filaments are never wider than the MMTF PSF ($\sim 0.6''$), except in the case of Sersic 159-03. At a typical redshift of 0.06 ($d \sim 250$ Mpc), this corresponds to an upper limit on the typical filament width of 0.7 kpc.
- In some cases, where the filaments are very extended (Abell 1644, Abell 1795, Sersic 159-03), there is evidence for matching morphology in the near-UV. This is especially true in the case of Abell 1795, which we have confirmed with much higher resolution near-UV images in §2. However, it is challenging to match the NUV and $H\alpha$ morphologies in general due to the mismatch in the PSF widths.

The properties of the observed $H\alpha$ filaments are summarized in Table 3.5 and a detailed discussion of individual clusters can be found in the appendix. Based on the properties of the $H\alpha$ emission, the sample can be divided into 3 categories: those with complex, extended filaments (type I), those with nuclear emission or only slightly extended (i.e. a few PSF widths) emission (type II) and those with no observable emission (type III). We use this convention throughout the remainder of our discussion to easily identify trends at other wavelengths which could explain both the flux and morphology of the $H\alpha$ emission.

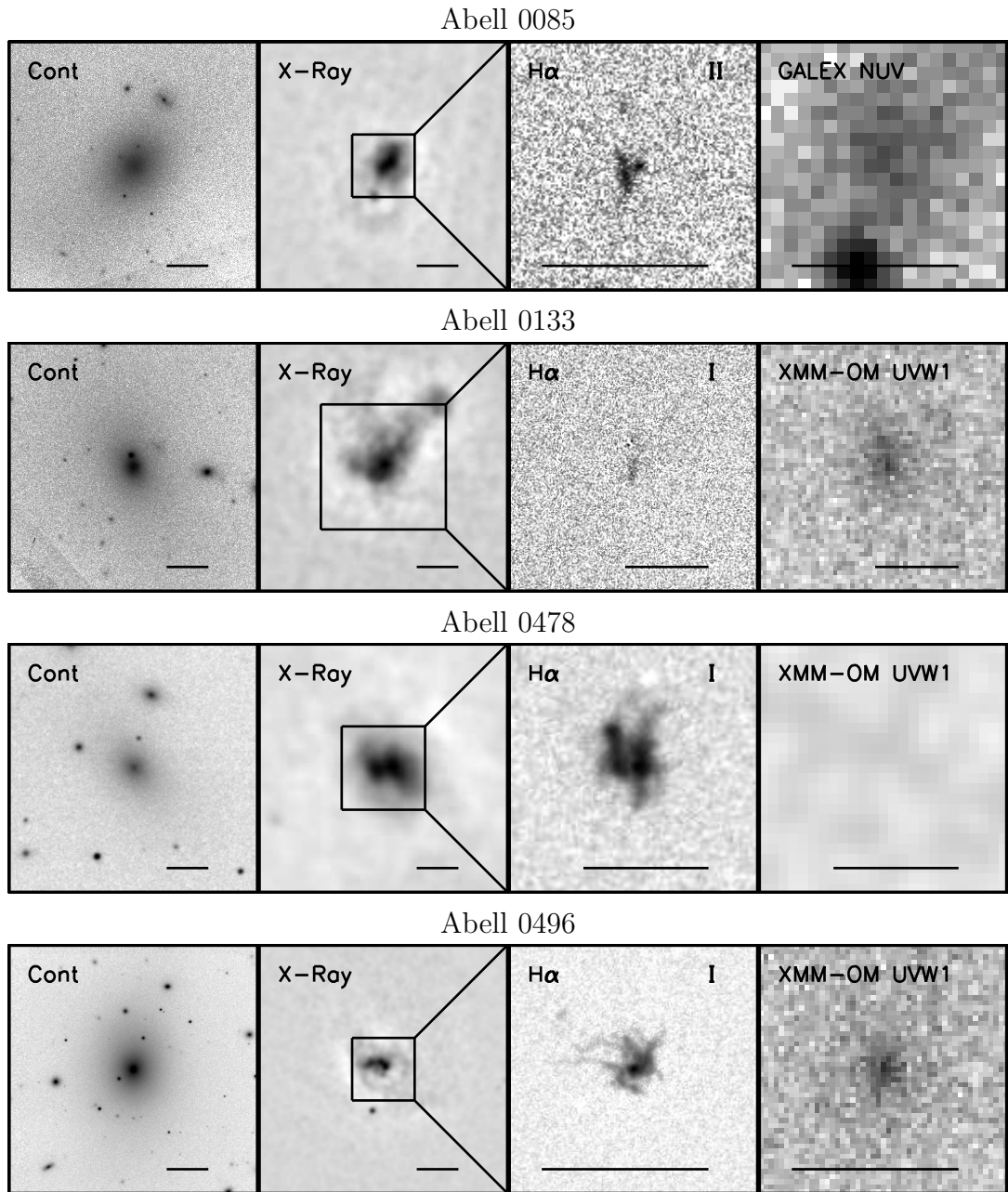
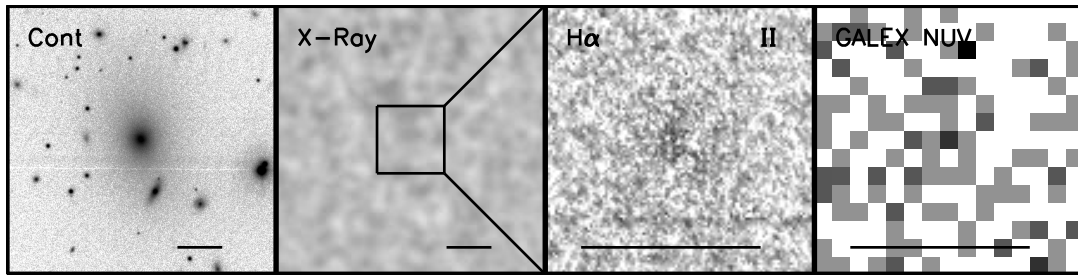
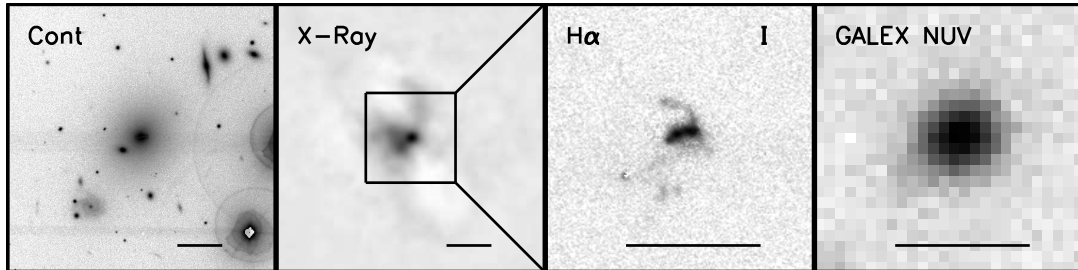


Figure 3.4 Multi-wavelength data for the 21 clusters in our sample with NUV (GALEX, XMM-OM) and H α (MMTF) data. From left to right the panels are: 1) MMTF red continuum image, 2) Unsharp masked CXO X-ray image, 3) MMTF continuum-subtracted H α image, 4) GALEX/XMM-OM NUV image. The horizontal scale bar in all panels represents 20 kpc. The X-ray and red continuum images are on the same scale, and the H α and NUV data are on the same zoomed-in scale. The square region in the X-ray panels represents the field of view for the zoomed-in H α and NUV panels.

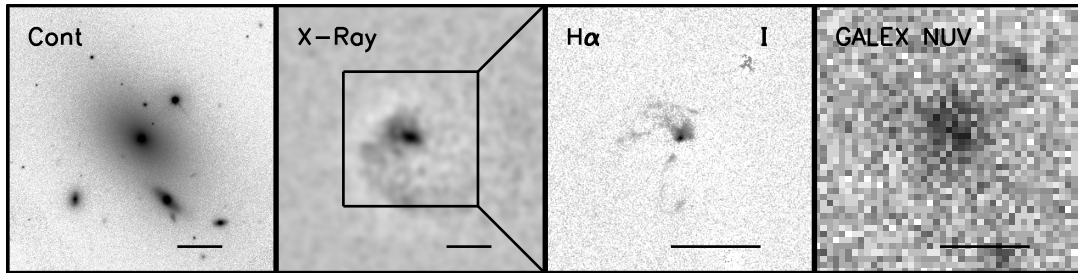
Abell 0644



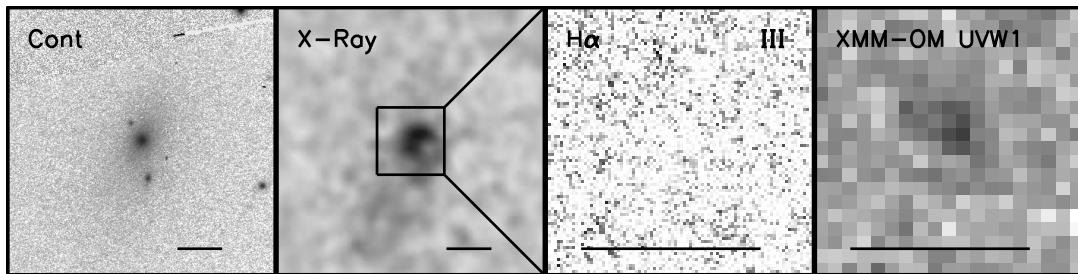
Abell 0780 (Hydra A)



Abell 1644



Abell 1650



Abell 1795

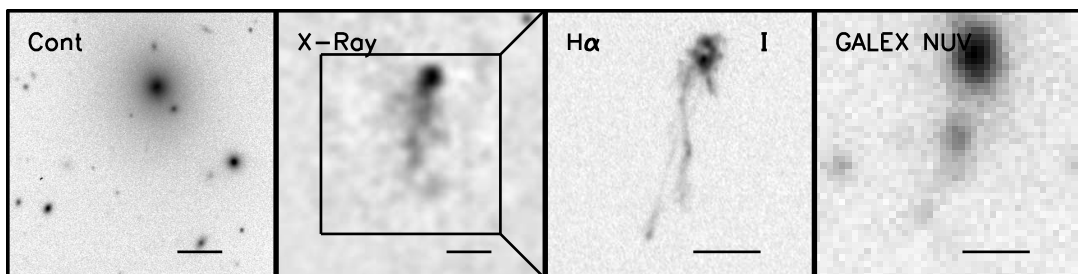
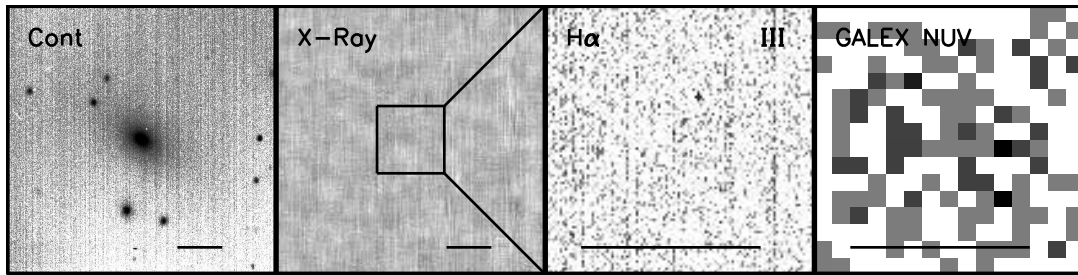
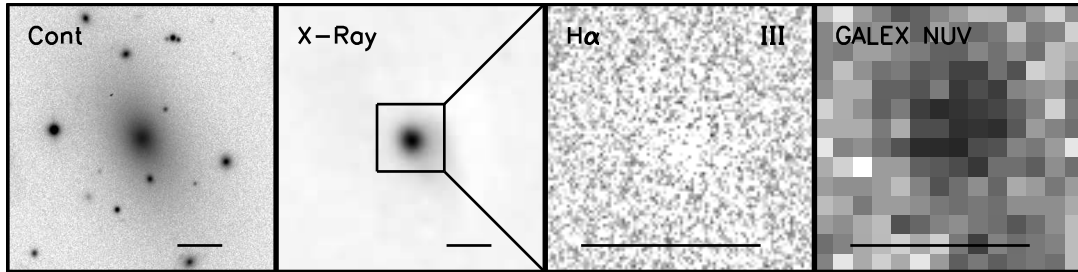


Figure 3.4 Continued.

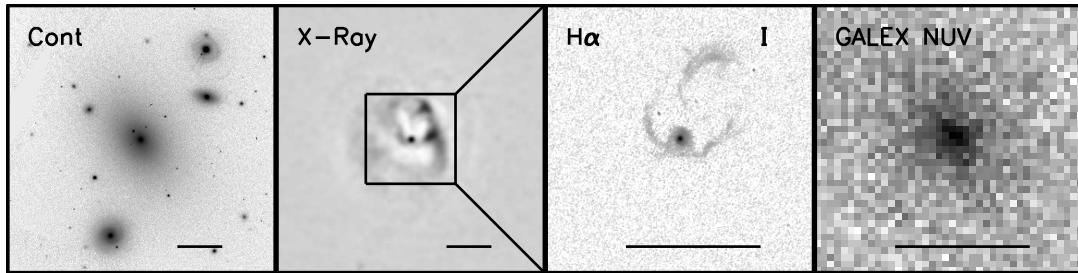
Abell 1837



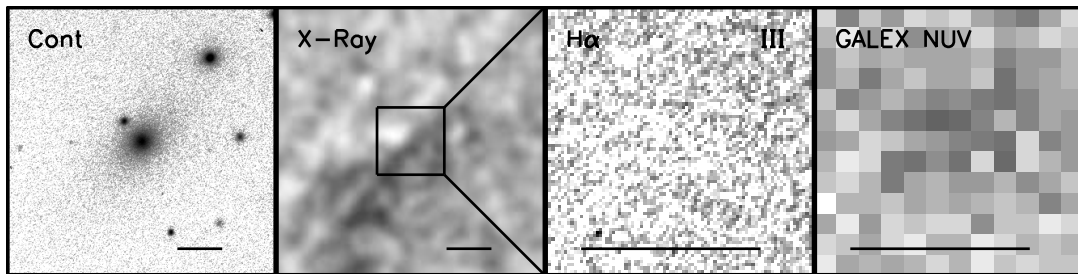
Abell 2029



Abell 2052



Abell 2142



Abell 2151

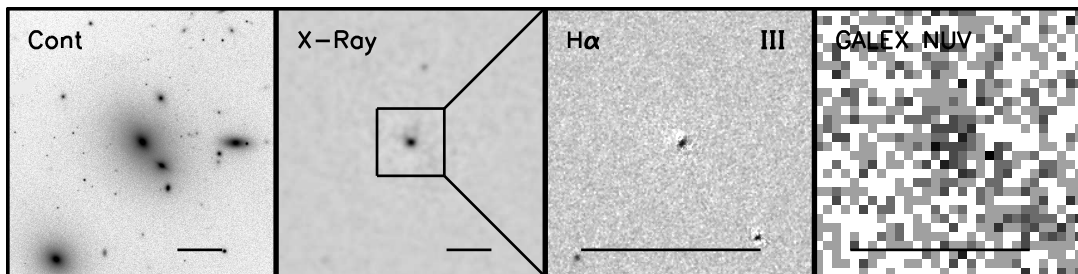
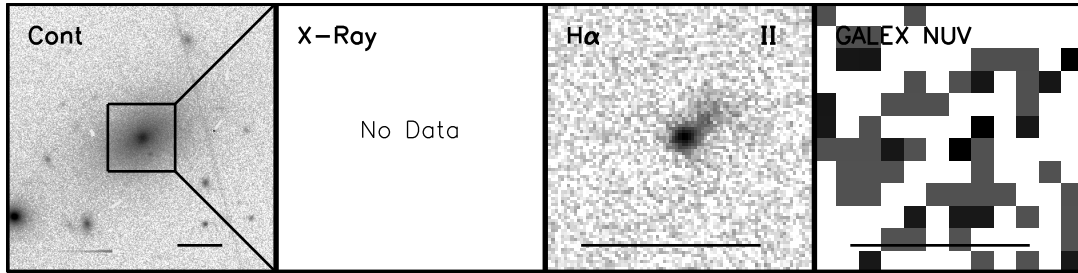
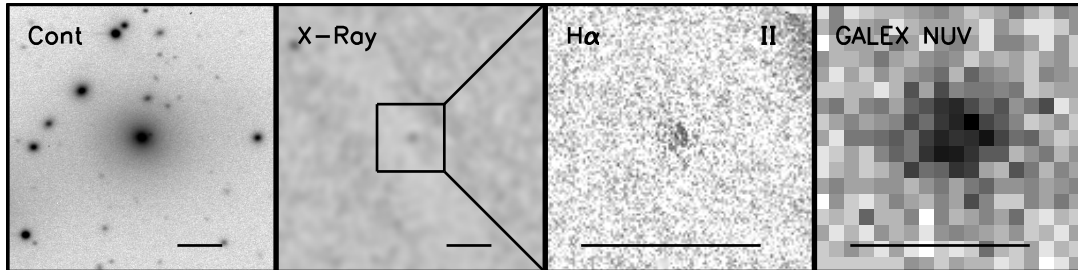


Figure 3.4 Continued.

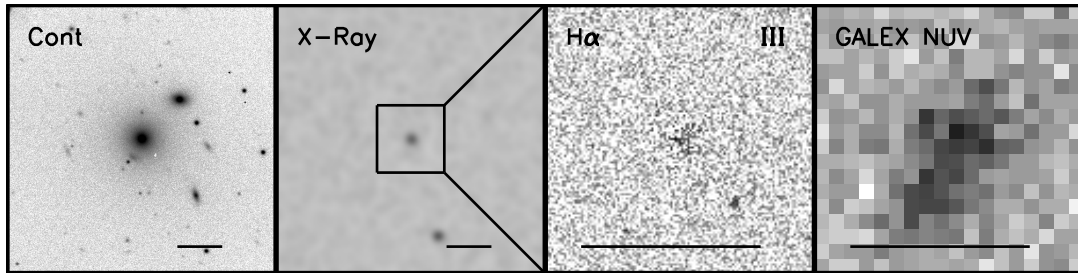
Abell 2580



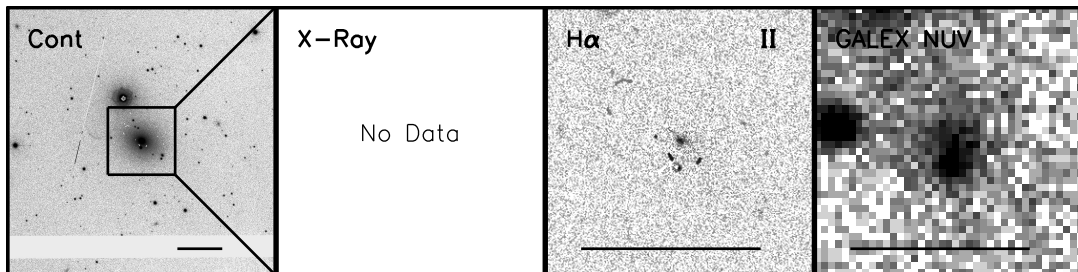
Abell 3158



Abell 3376



Abell 3389



Abell 4059

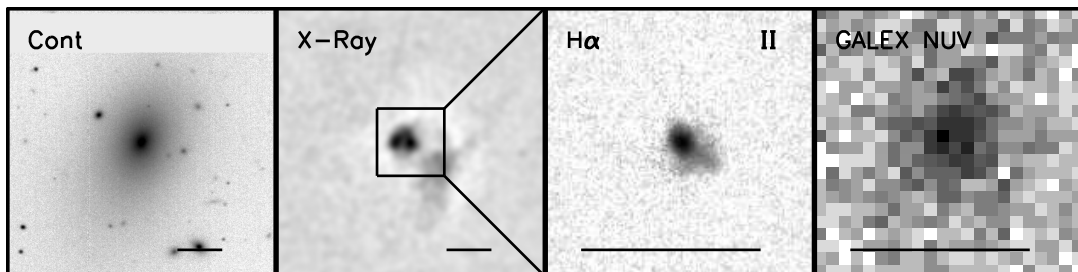


Figure 3.4 Continued.

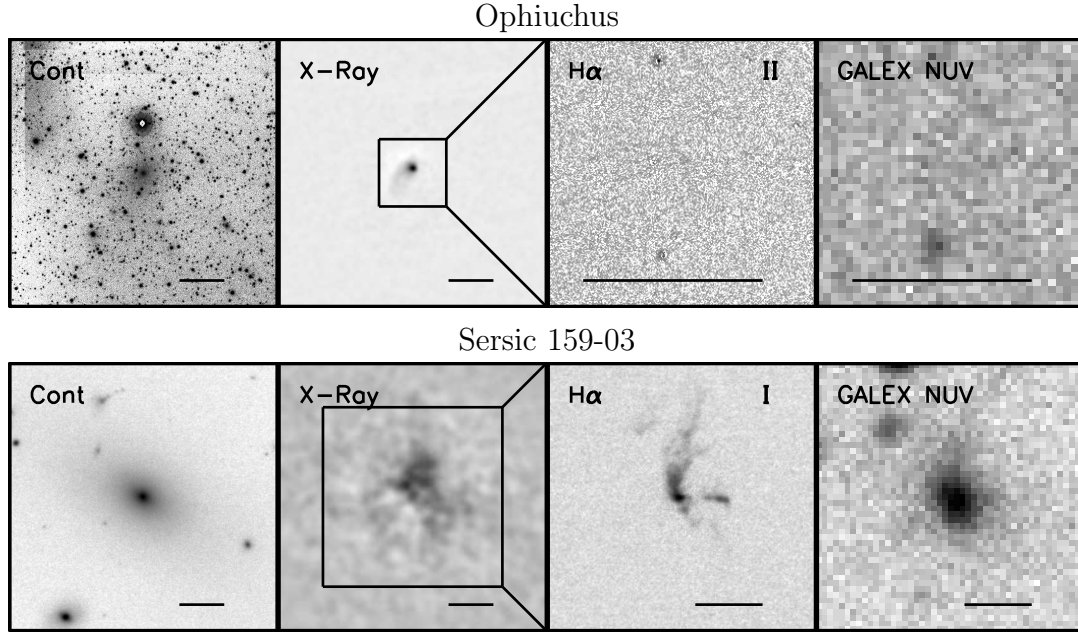


Figure 3.4 Continued.

3.3.2 Star Formation

A likely explanation for the presence of $H\alpha$ emission is photoionization by massive, young stars. However, while several studies to date have found star formation in the central cluster galaxy, very little work has been done on correlating the observed $H\alpha$ filaments with young stars for a large sample of clusters. As mentioned earlier, archival near-UV data from *GALEX* and *XMM-OM* exist for 21 of our 23 sample clusters. Figure 3.6 shows that there is a weak correlation (Pearson $R = 0.51$) between the near-UV and $H\alpha$ luminosities. This result is not surprising since the cooling flow in these systems is allegedly depositing some cold gas onto the BCG and triggering some star formation activity. However, there is considerably more scatter than one would expect if the ionization was purely from continuous star formation, suggesting that modifications to the star formation law (i.e. altering the IMF), or alternative physical mechanisms entirely, may be needed to explain the observed NUV/ $H\alpha$ ratios.

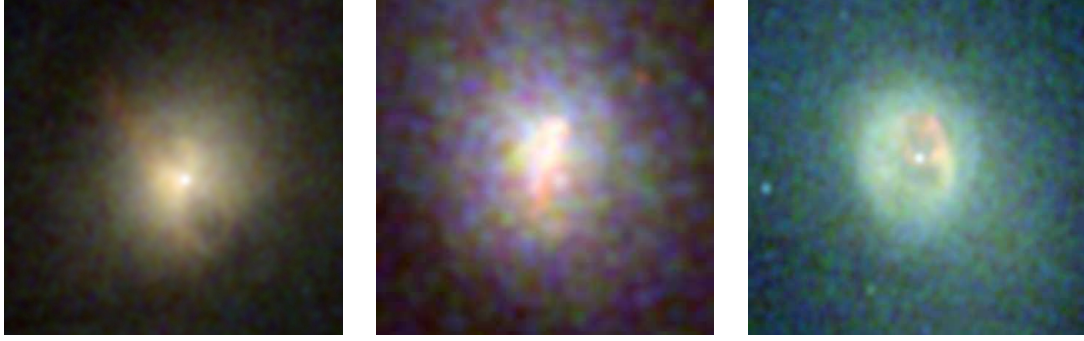


Figure 3.5 False color X-ray images of three clusters in our sample. From left to right, these are Abell 0780 (Hydra A), Abell 1795 and Abell 2052. The colors are 0.5-2 keV (red), 2-4 keV (green) and 4-8 keV (blue). The asymmetry in the X-ray ICM is clearly associated with the coolest (0.5-2 keV) gas.

In Figure 3.6, we also show the NUV/H α ratios for several different processes, including continuous star formation (described by Kennicutt 1998). Using models from Starburst99 (Leitherer et al. 1999) we age a burst of star formation from 1–20 Myr in order to see the evolution of the NUV and H α flux. These models assume a metallicity of $0.4Z_{\odot}$ and a Kroupa IMF (Kroupa 2001) with $\alpha = 3.3$. The NUV/H α ratio is quite sensitive to the IMF assumed, but the overall trends remain the same. As the massive stars die off, the UV/H α ratio increases rapidly. This scenario is promising, since several clusters have NUV/H α ratios above the value predicted by Kennicutt (1998) and there are very few physical mechanisms that can produce such ratios. In this scenario, star formation took place in a burst as gas crosses R_{cool} and the NUV/H α ratio is a direct indicator of the time elapsed since this burst. If this is indeed the reason for the high UV/H α ratios, we would expect higher resolution UV data to show age gradients along the length of any filaments. This trend was not seen in Abell 1795 (§2), although there was a slight offset between the UV and H α emission which made quantifying a gradient difficult. An alternative explanation for the high NUV/H α ratios is the dependence of this quantity as a function of H α surface density (Meurer et al. 2009). For star formation in regions

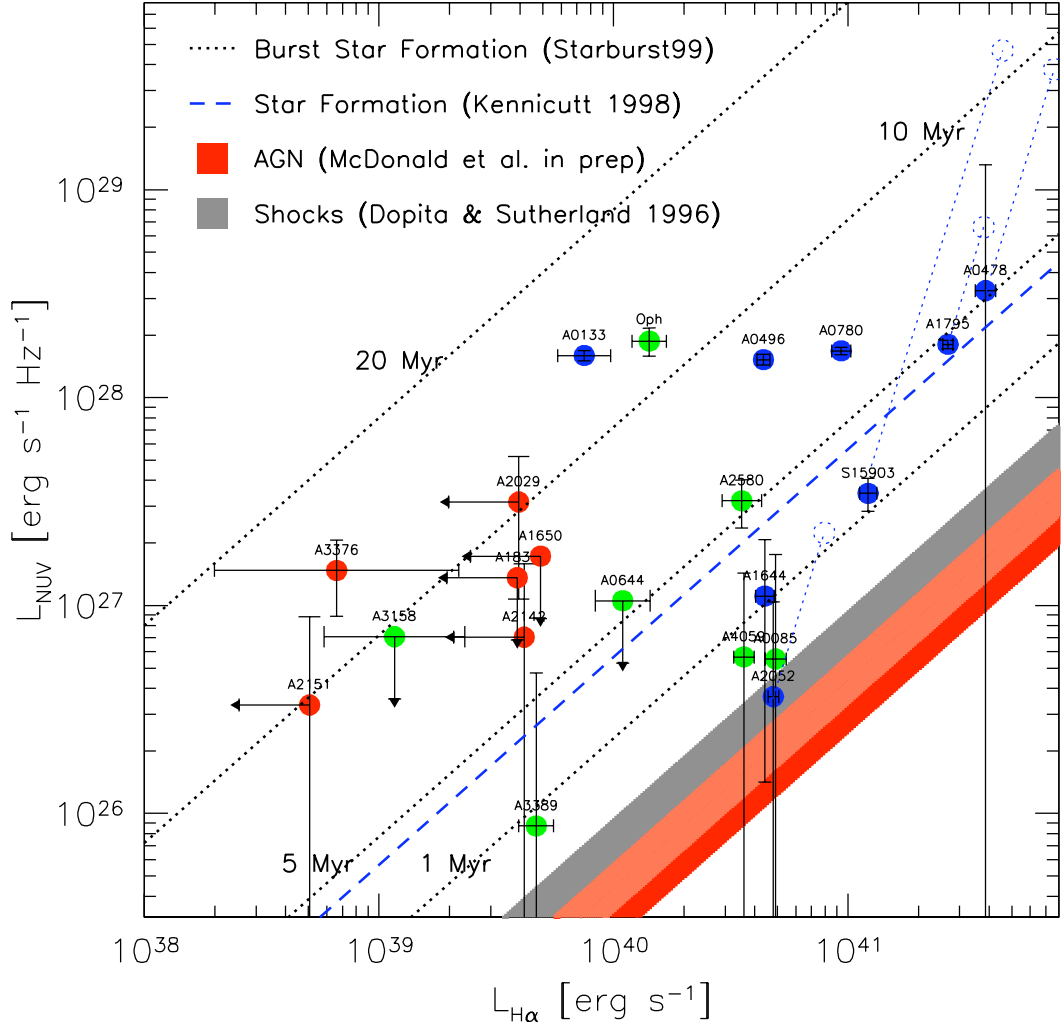


Figure 3.6 Global GALEX NUV versus MMTF $H\alpha$ luminosities for the 21 clusters in our sample with archival GALEX data. The dashed blue line represents ongoing star formation, described by Kennicutt (1998). The dotted black lines describe the evolution of the NUV/ $H\alpha$ ratio as a starburst ages from 1–20 Myr (Starburst99; Leitherer et al. 1999). The shaded grey area shows the range of NUV/ $H\alpha$ ratios expected from shocks (Dopita & Sutherland 1996), while the shaded red area shows the expected NUV/ $H\alpha$ ratio for the AGN, based on HST FUV imaging of cluster cores (§5). The orange area represents the overlap between these two regimes. The point color refers to the classification described in §3.3.1: type I (blue), type II (green) and type III (red). The dotted lines/circles show the effect of correcting for intrinsic extinction, with reddening estimates taken from Crawford et al. (1999) and Jaffe et al. (2005). The large deviations from ongoing star formation (Kennicutt 1998), suggest that non-stellar processes may be responsible for some of the observed $H\alpha$ emission. Contamination from the nucleus likely plays an important role in the observed scatter.

with low $H\alpha$ surface brightness (i.e. UGCA44) the UV/ $H\alpha$ ratio is a factor of $\sim 5\times$ higher than for a region with higher surface brightness (i.e. NGC 1566). Thus, both scenarios of an aging burst of star formation and star formation in low surface density environments can yield the scatter above the Kennicutt relation that we observe. A third potential source of high UV/ $H\alpha$ ratios is intrinsic reddening due to dust in the BCG. We show, in Figure 3.6, the effect of correcting for intrinsic reddening, using extinction measurements from Crawford et al. (1999) and Jaffe et al. (2005). Applying this correction tends to move points *further* above the Kennicutt relation, suggesting that the high UV/ $H\alpha$ ratios we measure are not due to dust in the BCG.

Figure 3.6 presents the *global* NUV and $H\alpha$ luminosities, since the poor spatial resolution of the *GALEX/XMM-OM* data does not allow us to discriminate between filament and nuclear emission. In §2, however, we show that the UV/ $H\alpha$ ratio in the nucleus of Abell 1795 is quite low ($L_{FUV}/L_{H\alpha} \sim 7\times 10^{-14} \text{ Hz}^{-1}$). In §5, we show that this is typical for AGN (central point source) in BCGs based on HST far-UV imaging of cooling flow cluster cores. This means that the effect of including the nuclear contribution in the luminosity calculation would move the data below the Kennicutt relation.

Finally, we show the UV/ $H\alpha$ ratio expected from shock heating (Dopita & Sutherland 1996). Again, this produces low ratios and thus could only be a strong contributor in very few of the clusters. Most notably, Figure 3.6 shows that the NUV/ $H\alpha$ ratio for Abell 2052 is consistent with shock heating, and we observe that the $H\alpha$ emission traces the outer shell of a cavity carved in the ICM by a radio jet seen at 1.4GHz (see Figure 3.4). This is strong evidence for the $H\alpha$ -emitting gas to be shock heated by an AGN outflow in this object.

3.3.3 X-Ray Profiles

Figure 3.7 shows the radial profiles for various parameters derived from the X-ray data: temperature (kT), density (n_e), metal abundance, specific entropy ($K = kT \cdot n_e^{-2/3}$ keV cm²), cooling time ($t_{cool} = 10^8 \cdot (K/10 \text{ keV cm}^2)^{3/2} \cdot (kT/5 \text{ keV})^{-1}$ Gyr) and mass deposition rate (dM/dt). There appears to be very little difference in the shape or absolute normalization of the density profile between clusters with and without optical filaments. Likewise, while there is a large spread in the values, there appears to be very little correlation between the radial abundance profile and the presence of optical emission. Interestingly, there appears to be a very strong correlation between the absolute level of the temperature profile and our filament type classification. That is, for clusters with extended, bright optical filaments (type I), the temperature is lower at all radii. For those with nuclear or no emission (types II or III), the temperature is higher at all radii. Since the presence of H α filaments has been shown to be enhanced in cooling flow clusters (Edwards et al. 2007), one would expect the core temperature to be correlated with the presence of filaments. We find that this correlation extends from the core to much larger radius, such that the temperature at all radii from the very center out to the cooling radius is lower in clusters with extended H α filaments.

The motivation for producing these radial profiles was to look for a correlation between the entropy profile and the presence of optical filaments, which was alluded to by Donahue et al. (2006). However, while previous authors (e.g., Cavagnolo et al. 2008) have found that the central entropy, K_0 , is much lower in clusters with H α emission, we find that the entropy is lower everywhere interior to the cooling radius for clusters with extended H α emission. Naively, one would expect strong AGN feedback and cluster-cluster mergers to raise both the local temperature and entropy,

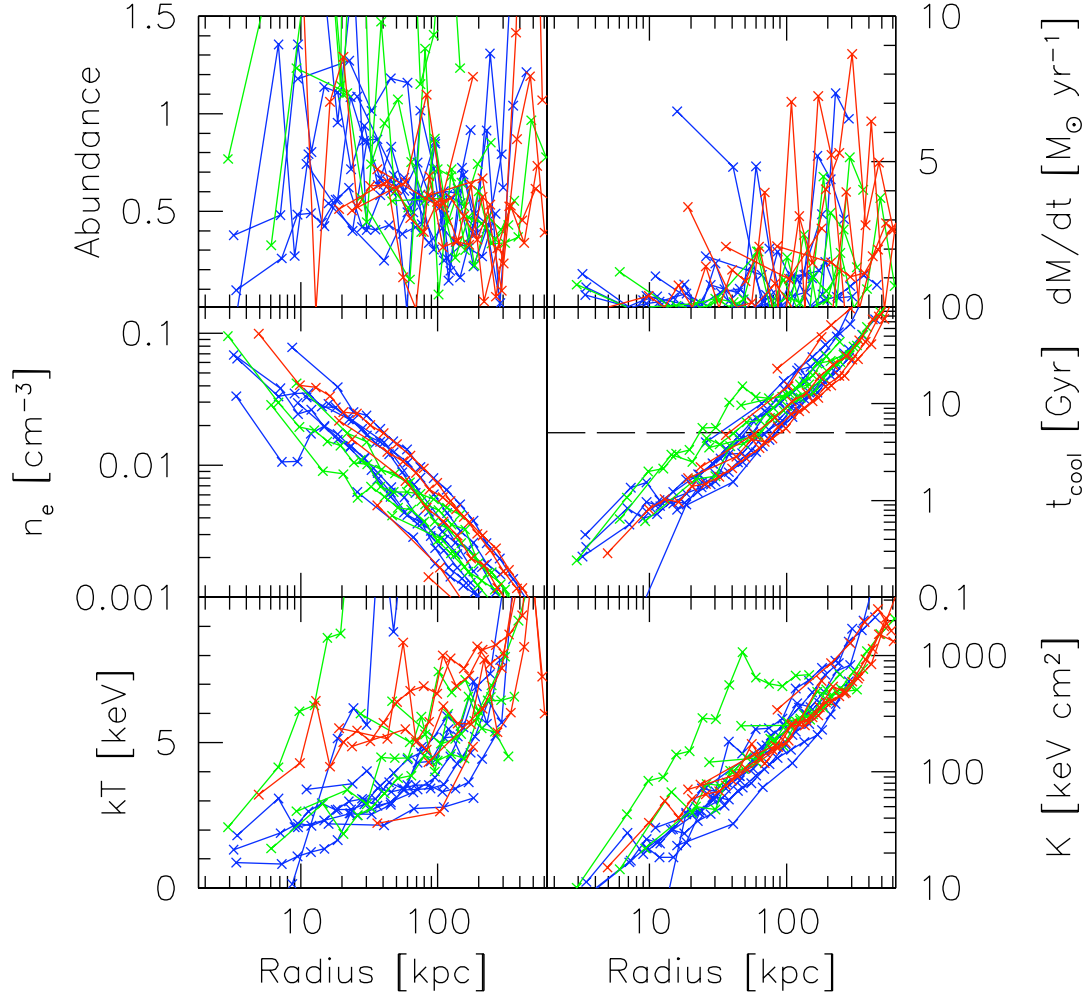


Figure 3.7 X-ray derived radial profiles for abundance, electron density (n_e), temperature (kT), specific entropy ($K = kT \cdot n_e^{-2/3}$ keV cm²), cooling time ($t_{cool} = 10^8 \cdot (K/10 \text{ keV cm}^2)^{3/2} \cdot (kT/5 \text{ keV})^{-1}$ Gyr) and mass deposition rate (dM/dt). The dashed line in the right middle panel represents a cooling time of 5 Gyr. The color scheme here is the same as in Figure 3.6. The lower two panels show clearly that the clusters with H α filaments (blue) have lower temperature and entropy everywhere than those with nuclear or no H α emission (green and red respectively).

thus impeding the formation of $H\alpha$ filaments. However, simulations have found that, under the correct circumstances, AGN feedback can lead to the formation of cold filaments as radio-blown bubbles rise to large radii (e.g., Fabian et al. 2003; Pope 2010; Revaz et al. 2008).

We observe that both the temperature and entropy are lower in the inner ~ 100 kpc for clusters with observable $H\alpha$ filaments (Figure 3.7). In order to quantitatively compare this phenomenon to the presence of ionized filaments, we consider quantities derived with this scale in mind. Figure 3.8 shows the comparison of the NUV and $H\alpha$ luminosities with the average temperature inside of 100 kpc (kT_{100}), the specific entropy at 30 kpc (K_{30}) and the mass deposition rate (dM/dt). The UV and $H\alpha$ luminosities are shown in terms of their inferred star formation rates, derived using Kennicutt (1998), so that the comparison to dM/dt is straightforward. However, these values are linearly proportional to the luminosity and so any observed correlation is independent of this choice of scaling.

In Figure 3.8, we see a strong correlation between the UV or $H\alpha$ luminosity and both the entropy and dM/dt over three orders of magnitude. Previous works (e.g., Cavagnolo et al. 2008) have pointed out that systems with lower core entropy tend to have UV/ $H\alpha$ emission, however we show that the entropy outside of the core is, potentially, an even better tracer of $H\alpha$ emission. We prefer this diagnostic since several of our clusters have relatively low surface brightness X-ray emission, making it difficult to constrain the entropy in the core where the signal-to-noise is low. The lower entropy systems tend to have brighter $H\alpha$ filaments, with Abell 1795, Sersic 159-03 and Perseus A occupying the lowest-entropy and highest $H\alpha$ luminosity regime. The correlation between dM/dt and the $H\alpha$ luminosity suggests a link between the cooling flow and either the presence or ionization of the warm gas. The observed $H\alpha$ luminosity is $\sim 1-2$ orders of magnitude too high for it to be

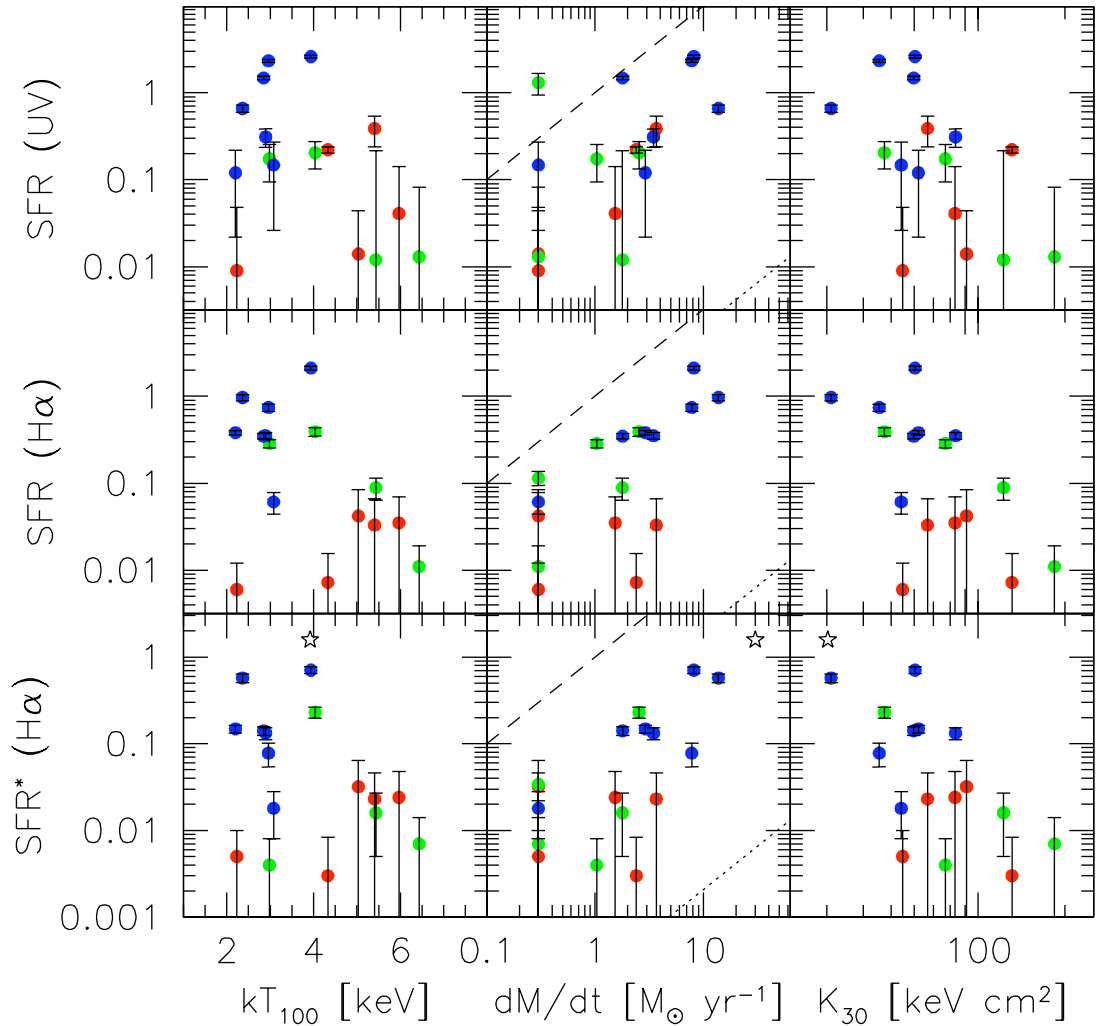


Figure 3.8 UV and $H\alpha$ determined star formation rates, based on Kennicutt (1998), against the average temperature in the inner 100 kpc (kT_{100}), specific entropy at 30 kpc (K_{30}), and the integrated mass deposition rate (dM/dt). The color scheme here is the same as in Figure 3.6. The SFRs in the lower panels have had the nuclear contribution removed (SFR^*). The open star in the lower panels refers to Perseus A (Conselice et al. 2001; Sanders et al. 2004). The four points with $dM/dt = 0.3 M_{\odot} \text{ yr}^{-1}$ have no measurable cooling flow and are plotted as upper limits. The diagonal dashed line represents the limit where all of the cooling X-ray gas turns into stars, while the dotted line is the case where all of the cooling X-ray gas is made up of hydrogen which recombines only once (Fabian et al. 1984). A strong correlation is seen between the $H\alpha$ luminosity in filaments, and both the mass deposition rate and the average cluster entropy.

due to recombination from the hot X-ray gas, assuming a single $H\alpha$ photon per recombination. On the other hand, even if all of the $H\alpha$ is due to star formation, there is not enough ongoing star formation to account for all of the gas in the cooling flow. However, one should be cautious when using the X-ray derived dM/dt since they do not represent the true mass of gas cooling out of the X-ray, since it is still unclear how cooling proceeds below soft X-ray energies (Peterson & Fabian 2006). Note, nevertheless, that there appears to be a temperature threshold of ~ 5 keV for ionized filaments, below which nearly all clusters in our sample have extended $H\alpha$ emission. It is unclear at present whether there is a lower temperature threshold below ~ 2 keV, which is the domain of galaxy groups.

From the radial X-ray profiles and the 2-dimensional $H\alpha$ data, we are also able to derive two interesting scale radii. These are: R_{cool} , the radius at which the cooling time of the X-ray gas is equal to 5 Gyr, and $R_{H\alpha}$, the maximum extent of the $H\alpha$ filaments. The relationship between these radii is shown in Figure 3.9. While there is a large observed range in the radius of the $H\alpha$ emission, there appears to be a hard edge at R_{cool} – we never observe $H\alpha$ emission beyond the radius where the X-ray cooling time is > 5 Gyr. This is a strong indication that the $H\alpha$ emission is intimately linked to the X-ray cooling flow. The fact that the data appear to prefer a certain timescale (5 Gyr) for the cooling radius is a new and puzzling discovery. Interestingly, recent studies have shown that beyond $z \sim 0.5$ the frequency of clusters with cool cores is significantly lower than in the local Universe (see e.g., Santos et al. 2008; Vikhlinin et al. 2007). This redshift corresponds to a lookback time of 5 Gyr, which provides further motivation for our choice of cooling radius. Thus, if cooling flows were unable to begin until 5 Gyr ago as the evidence suggests, we would expect the radius at which $t_{cool} = 5$ Gyr to be a natural boundary for the $H\alpha$ filaments.

Additionally, if we adopt the idea of stars forming in bursts, as indicated by

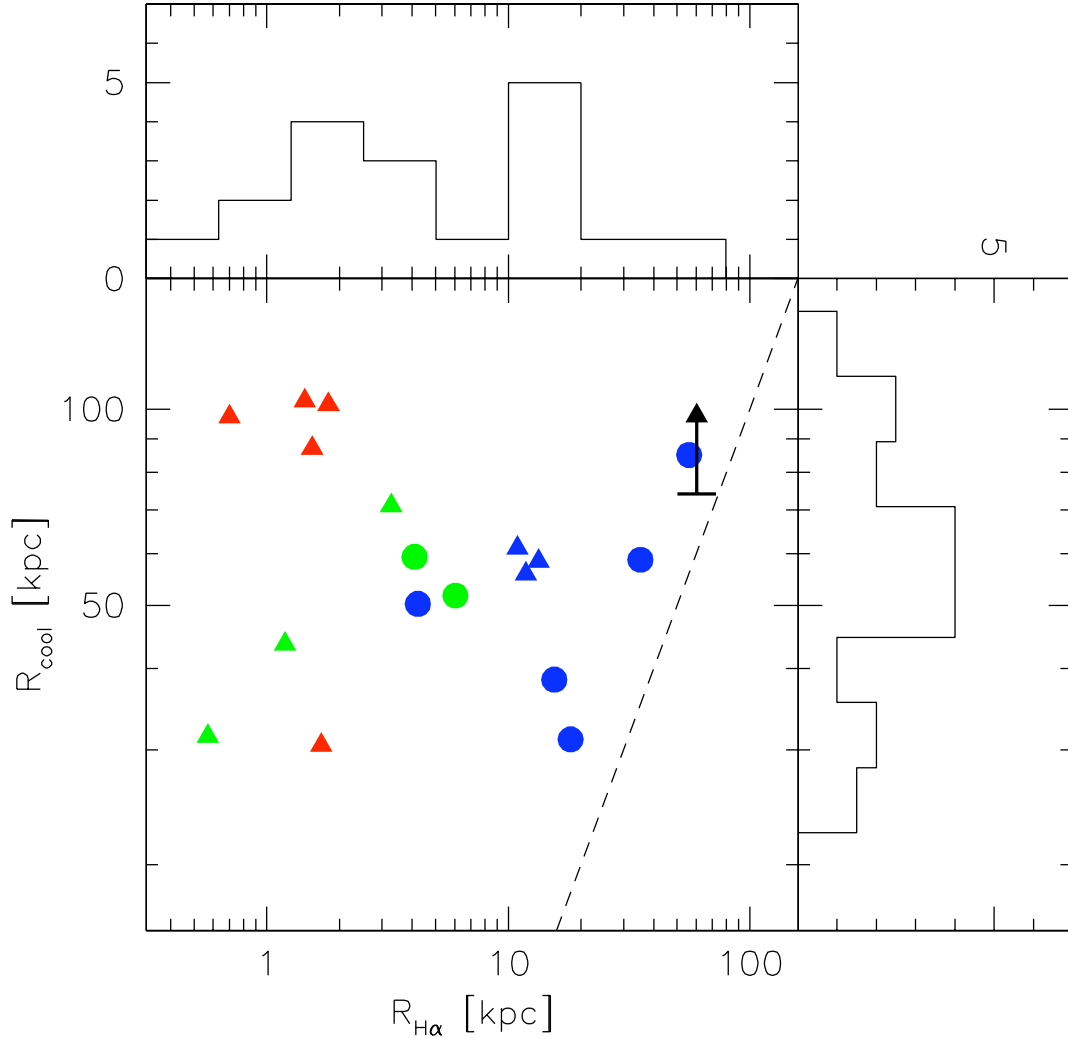


Figure 3.9 Correlation and distributions of R_{cool} , the radius at which the cooling time of the ICM reaches 5Gyr; and $R_{H\alpha}$, the largest radius at which we detect $H\alpha$ emission. For the cases with no detected $H\alpha$ emission an upper limit of the seeing FWHM has been used. The dashed line refers to the one-to-one case, while the point colors are consistent with Figure 3.6. The shapes of the symbols refer to the $NUV/H\alpha$ ratio: circles have $NUV/H\alpha < 10^{-13.2} \text{ Hz}^{-1}$, while triangles have $NUV/H\alpha > 10^{-13.2} \text{ Hz}^{-1}$. Note that, in the burst formation scenario this corresponds to age, with circles representing younger and triangles older stars. There appears to be an upper limit on the radius of $H\alpha$ filaments, corresponding to the cooling radius. The black point represents a lower limit estimate on the cooling radius of Perseus A (Conselice et al. 2001; Fabian et al. 2000). The effect of decreasing the cooling time used to defined R_{cool} is to move points down in this plot.

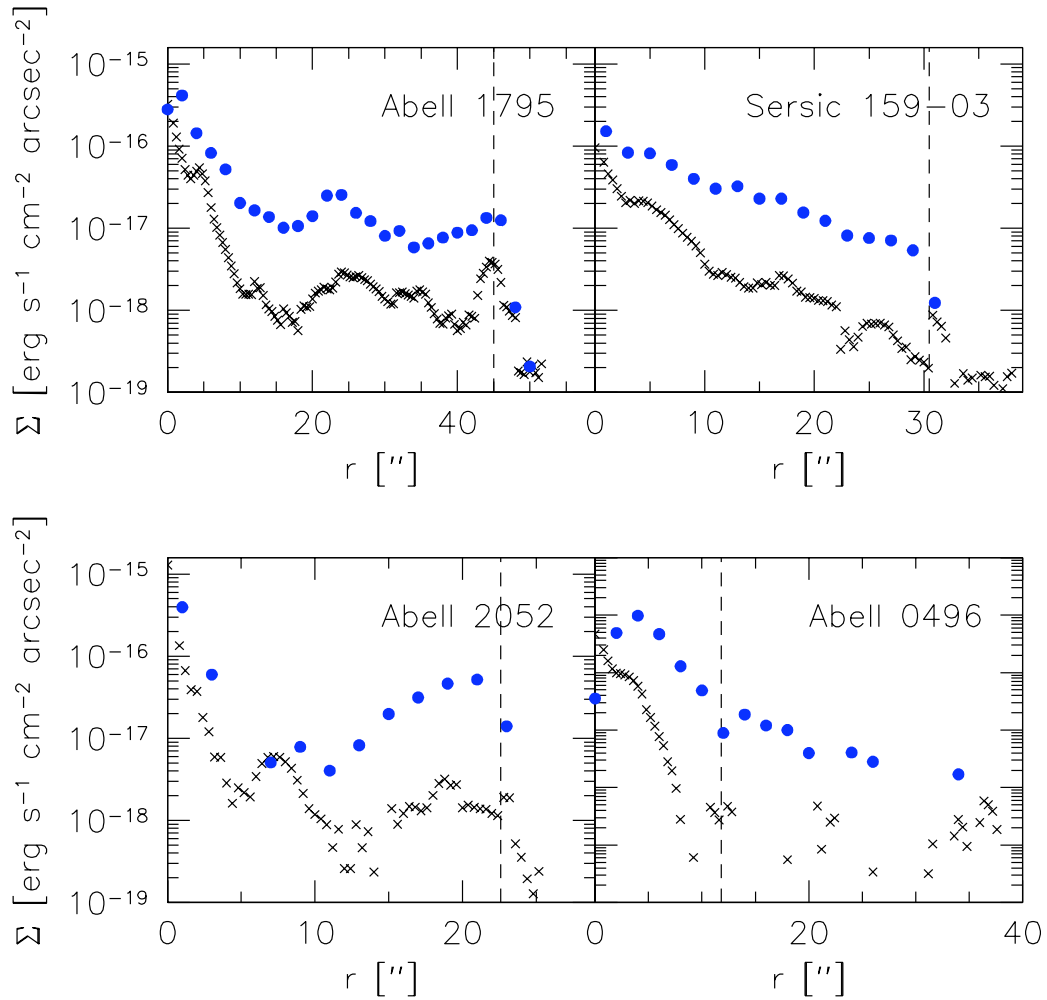


Figure 3.10 $H\alpha$ surface brightness profiles for the three clusters with $R_{H\alpha}/R_{cool} \sim 1$ and one cluster with $R_{H\alpha} \ll R_{cool}$ (Abell 0496). The black crosses represent the azimuthally averaged profile, while the blue circles are the surface brightness along a $\sim 5''$ wide cut, oriented along the most extended filament. The vertical dashed line represents the location of $R_{H\alpha}$, as measured by eye. The sharp drop-off of surface brightness at $R_{H\alpha}$ suggests that this is truly the edge of the filament, independent of the depth of our exposure.

the location of the points in Figure 3.6, our data show that the emission from the youngest stars tends to be much more extended, while the emission from stars formed in a burst ~ 10 Myr ago tend to be concentrated in a nuclear region, lending some support to a radially-infalling scenario.

Since we are claiming a link between the cooling radius and the maximum radius of $H\alpha$ emission, it is important to assess whether we are truly seeing all of the $H\alpha$ emission, or if a deeper exposure would yield $R_{H\alpha}/R_{cool} > 1$. In Figure 3.10, the $H\alpha$ surface brightness profiles of the three clusters with $R_{H\alpha}/R_{cool} \sim 1$ are shown. At $R_{H\alpha}$, there is a clear drop-off in the surface brightness in all three systems, suggesting that this is a real limit, not a function of our exposure depth. For clusters with $R_{H\alpha} < 0.5R_{cool}$ (e.g. Abell 0496, Figure 3.10, the edge of the filament blends into the background much more smoothly, suggesting that these filaments may in fact extend even further.

3.3.4 Properties of X-Ray Gas On and Off of Filament

Using smoothed $H\alpha$ images as masks, we were able to extract CXO spectra on and surrounding the warm ionized filaments, as described in §3.2.3 The off-filament spectra were fit with a single-temperature model, while two cases were considered for the on-filament spectra. In order to quantify the so-called “iron bias” (Boehringer & Werner 2009), which results from fitting a multi-temperature spectrum with a single-temperature model, we try fitting both one-temperature and two-temperature models to the on-filament spectra. A two-temperature model is clearly motivated if we assume that the ICM conditions are different on-filament, since it allows us to account for the ICM seen in projection in front of and behind the filaments. The S/N of the on-filament spectra are typically insufficient to constrain the temperatures, abundances and relative normalization in a two-temperature model, so we opt to

freeze the temperature and abundance for one of the two models to the off-filament conditions.

As we mentioned in §3.2.3, measuring the electron density on-filament requires an assumption about the geometry of the extraction region. For circular annuli, this is straightforward since we assume a spherical cluster. Since we can not be certain about the geometry of the filaments, we consider two limiting cases: 1) the filaments are thin tubes and extend no further than the width of our MMTF PSF (~ 1 kpc) into the plane of the sky; 2) the filaments are sheets seen edge-on with length equal to the observed size of the cluster. For the first case we model the spectrum with a two-temperature plasma to represent the thin filament embedded in the surrounding ICM, while the second case is modeled as a single-temperature slab of gas. The fact that we only see filaments that are unresolved in width suggests that the filaments are indeed thin and not sheets seen in projection. However we proceed under the assumption that both geometries are reasonable, thus bounding the “true” solution somewhere in between.

Fortunately, the assumption of geometry does not affect the calculation of the abundance or temperature. The on-versus-off filament temperature and abundance ratios are shown in Figure 3.11, for both single-temperature and two-temperature models. Immediately obvious from this figure is the fact that the filaments tend to be cooler than the immediate surroundings – the typical temperature in the filament is $\sim 50\%$ of that in the nearby gas. The fact that the X-ray gas near the $H\alpha$ filaments is significantly cooler than the surrounding ICM is further evidence that the $H\alpha$ filaments may be taking part in the cooling flow. Additionally, the on-filament metallicity tends to be significantly lower, reaching values less than $\sim 40\%$ of the off-filament values for about half of our systems. This does not appear to be the case for the 2-temperature model applied to the “outer filament” spectrum, suggesting

that the low on-filament metallicity may be a result of the iron bias Boehringer & Werner (2009). However, this is also the lowest S/N of the four scenarios considered. Thus, deeper data are required in order to say for certain what the true abundance gradient between the on- and off-filament spectra is. There are very few physical processes that decrease metallicity so, if the on-filament abundance is in fact lower with respect to the surrounding ICM, it is more likely that the low-metallicity gas has been transported from elsewhere.

A hint as to the origin of this low-metallicity gas can be found if we look at the 5 clusters with the largest on-off filament metal abundance contrast. With the exception of Abell 2052, all of these clusters have very strong radial abundance gradients. On the other hand, those clusters which do not have a strong on-off filament metal abundance contrast have relatively flat radial abundance gradients. To further drive this home, we show in Figure 3.12 the relationship between the on- and off-filament abundance and the abundance in four regimes: (1) $r \sim 0$, (2) $r < r_{cool}$, (3) $r \sim r_{cool}$ and, (4) $r > r_{cool}$. This figure shows that, in general, the metallicity in the filaments matches best with the metallicity at r_{cool} . For those four clusters with strong on-off filament abundance gradients (excluding Abell 2052), the on-filament abundance matches almost exactly the local abundance at r_{cool} . For the remaining four clusters, the on-filament abundance looks roughly the same as the abundance at all radii, due to the relatively flat abundance gradient. If we consider a two-temperature model for the on-filament spectrum, the correlation between the on-filament metallicity and the metallicity at the cooling radius becomes considerably less significant. Again, more data is needed in order to achieve a high enough on-filament S/N in order to constrain the abundance in a two-temperature model. A direct link between the on-filament metallicity and the metallicity outside of the cooling radius would further strengthen the connection between the H α filaments and the cooling flow. Further-

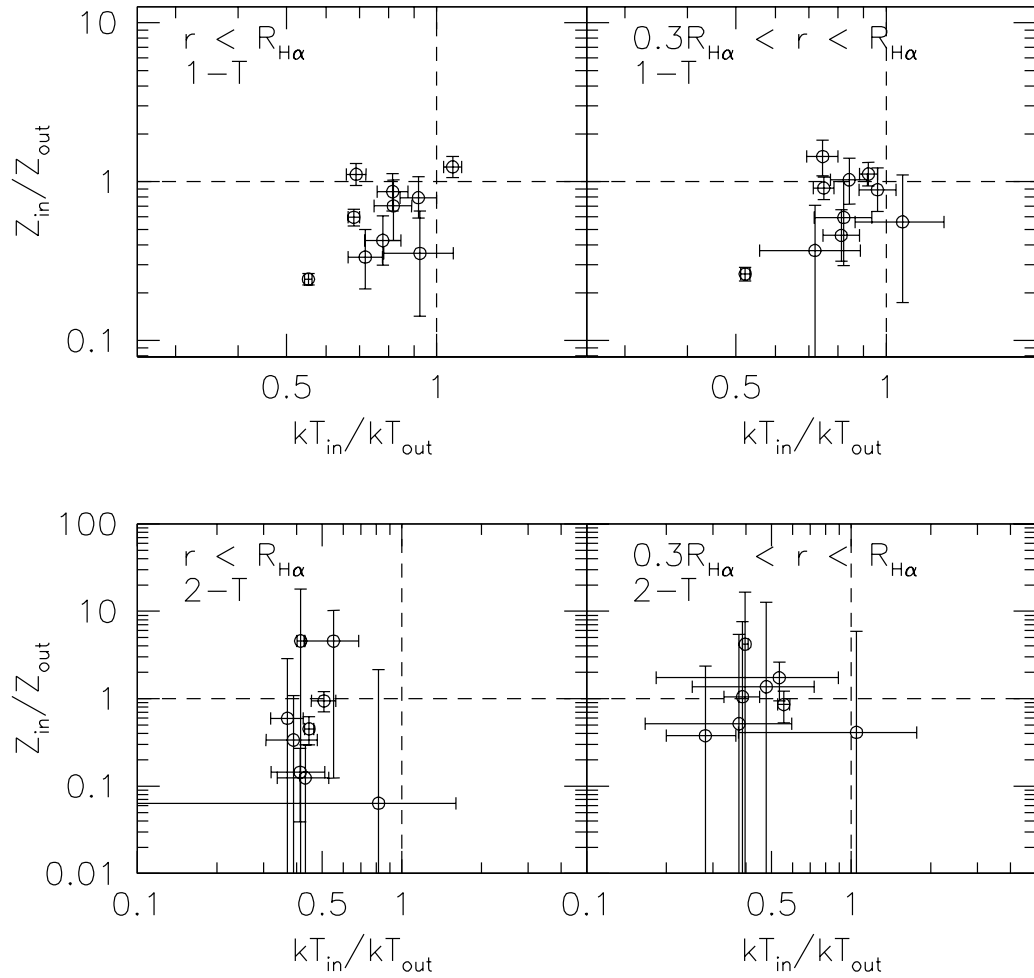


Figure 3.11 Upper left panel: Ratio of metallicity and temperatures of the X-ray gas coincident with $H\alpha$ filaments to that of the surrounding ICM for a single-temperature model. The dashed lines represent equal temperature and abundances inside and outside of the filaments. The filaments tend to have systematically lower temperatures and abundances in all cases with the exception of Abell 0780. Upper right panel: Similar to the left panel, except that only the outer 70% of the filament in radius is considered (see §3.2.3). Lower panels: Similar to the upper panels, except using a 2-temperature model to fit the on-filament spectrum. Note that this results in significantly lower on-filament temperatures and overall larger errors in both fitting parameters.

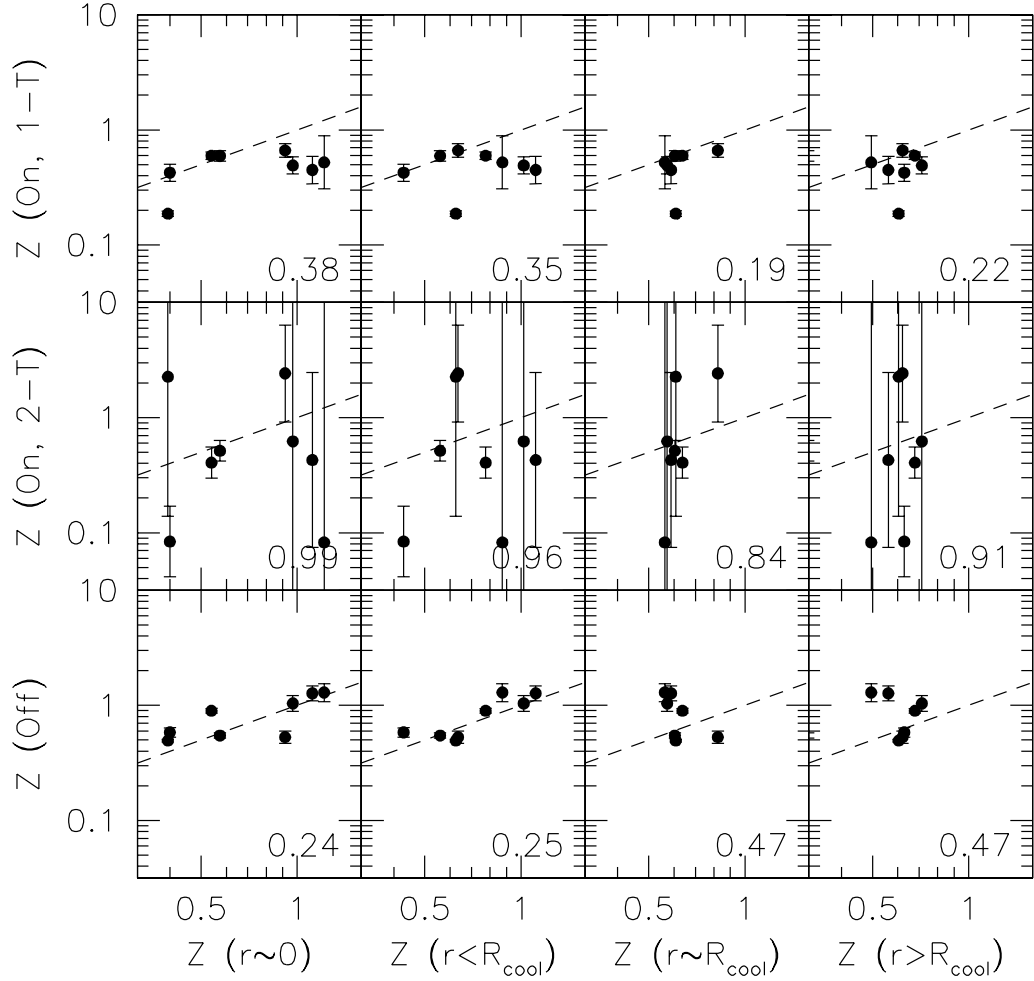


Figure 3.12 Upper panels: Metallicity of X-ray gas coincident with the $H\alpha$ filaments as a function of the metallicity in various radial bins. The number in each panel is the standard deviation around the line of equality. The metallicity of the in-filament gas matches more closely the metallicity of the ICM at the cooling radius than in any other radial region. The lowest point in the upper panels, which is an outlier in all four panels, is Abell 2052. For a discussion of why this cluster is an outlier, see the section on individual clusters in the Appendix. Middle panels: Same as upper panels, but now considering a two-temperature fit to the on-filament spectrum. The additional free parameters yields a poorly constrained in-filament abundance. Again, the abundance at the cooling radius appears to match best the in-filament abundance, but the difference is now only marginal. Lower panels: Same as above, but for the X-ray gas outside of the $H\alpha$ filaments.

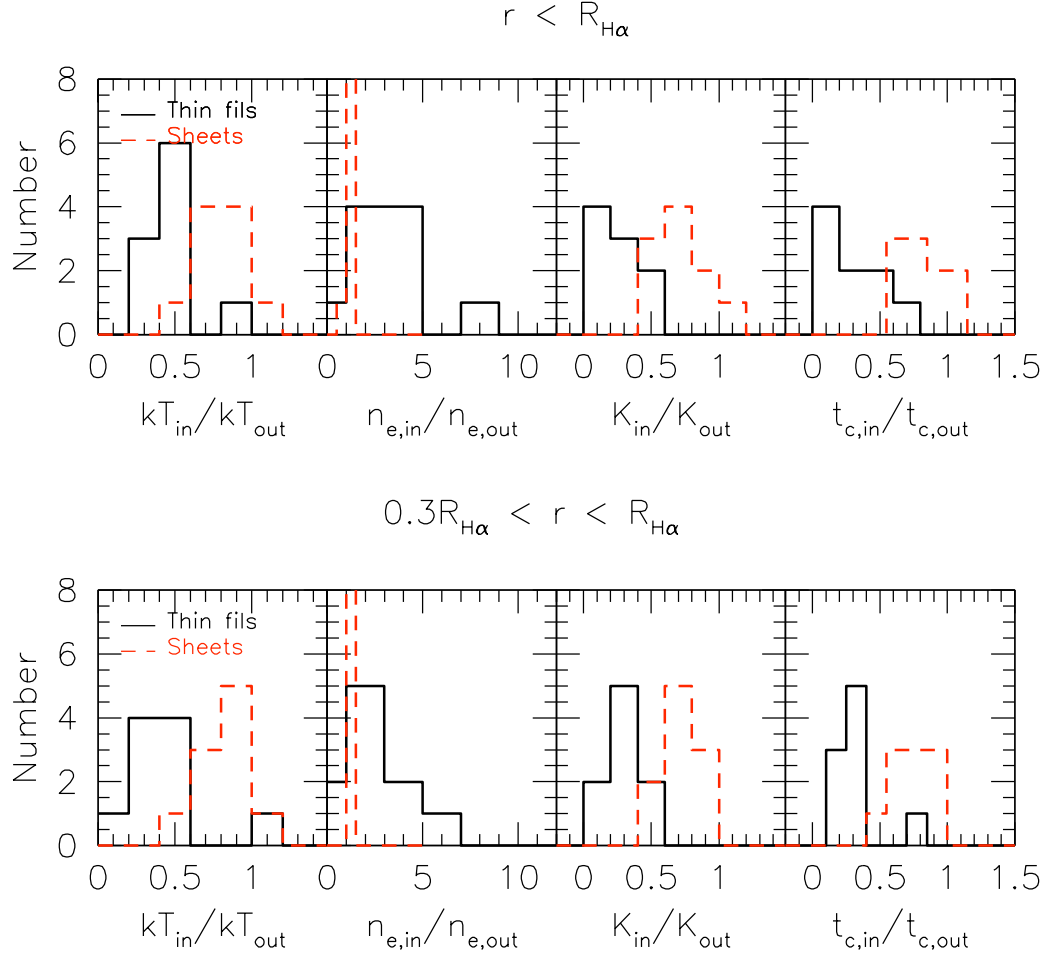


Figure 3.13 Upper panels: Distribution of temperature, electron density, entropy and cooling time ratios in and out of the $H\alpha$ filaments. The two line types bracket the extreme cases of the filament geometry: solid black lines are the thin filament case, which is modeled with a two-temperature plasma, while the red dashed line are the case of single-temperature sheets seen edge-on. The in-filament gas shares similar properties with the cooling flow, namely that the X-ray gas has a cooling time of $\sim 20\%$ that of the surrounding ICM. Lower panels: Similar to the above panels, but now considering only the outer 70% of the filaments in radius.

more, it would offer some evidence against the common hypothesis that the gas in the $H\alpha$ filaments comes from the central region, either from radio-blown bubbles (e.g., Revaz et al. 2008) or from gas sloshing (e.g., Johnson et al. 2010). While in some cases the match between the core and on-filament abundances is good, it is overall worse than the match to the abundance at R_{cool} . However, there are two biases which are likely conspiring to increase the uncertainty in the core abundance measurement. First, we expect the core abundance to be most affected by the iron bias, implying that the core abundances which we quote are likely lower limits. At the same time, our coarse binning in the central region (chosen to ensure a high S/N deprojection) means that any strong dip in the central abundance will be smeared out, leading to a slightly higher measured abundance. As an example, for Abell 4059 we find a dip in the abundance profile in the center, with a central value of ~ 1.0 , while Reynolds et al. (2008) quote a value of ~ 0.3 due to their higher resolution. Using a 2-component model, Reynolds et al. (2008) find that the core abundance dip changes to an excess, with a central value of ~ 2.5 . Thus, it is clear that the value of the central abundance is highly dependent on the model and binning chosen, and is therefore uncertain.

In addition to the X-ray temperature and metallicity in the filaments, we can also measure various additional properties such as electron density, entropy and cooling time, as shown in Figure 3.13. The distribution of these properties offers further evidence for a link between the X-ray cooling flow and the $H\alpha$ emission. Assuming the thin-filament geometry, the density inside of the filament is typically a factor of a few higher than the surrounding ICM. Coupled with the temperature decrease mentioned above, this yields drastically lowered entropy and cooling times inside of the filament. With cooling times ranging from 10%-40% of the surrounding ICM, these regions are, by definition, part of the cooling flow. It should also be noted

that, even if we assume that the geometry is that of single-temperature sheets seen in projection, the cooling time and the entropy are lower overall inside of the filaments.

The overall results from extracting X-ray spectra coincident and anti-coincident with the observed $H\alpha$ filaments tell an interesting story. The $H\alpha$ filaments appear to reside in a portion of the ICM with higher densities that is cooling more rapidly than its surroundings, resulting in lower temperatures. The metallicity inside of the filaments resembles more closely the metallicity at the cooling radius than the adjacent off-filament gas, albeit with a considerable amount of uncertainty. These two results, coupled with the fact that the observed $H\alpha$ emission seems to know about the cooling radius ($R_{H\alpha} \lesssim R_{cool}$), suggests that the observed $H\alpha$ filaments are coupled to the cooling flow.

3.3.5 Properties of BCGs

As a method of probing whether or not these clusters harbor an AGN in their central galaxies, we consider the 1.4 GHz radio power as well as the presence of an X-ray point source in the cluster core. The distribution of radio luminosities for our sample is shown in Figure 3.14. We note that all clusters with filaments have a significant radio detection, while only 5/15 of the clusters without filaments have a significant radio detection. Thus, the presence of radio emission is not predictive of whether there will be extended $H\alpha$ filaments. The two clusters with detected X-ray point sources in the BCG, Abell 0780 (Hydra A) and Abell 2052 have large cavities in their X-ray halos, suggesting that the AGN is strongly influencing the surrounding medium. The $H\alpha$ in these two clusters is very likely linked to this activity. If we consider the remaining clusters, the correlation between radio power and the presence of $H\alpha$ filaments becomes much weaker, suggesting that the two phenomena are not directly tied to one another. Instead, whatever weak correlation

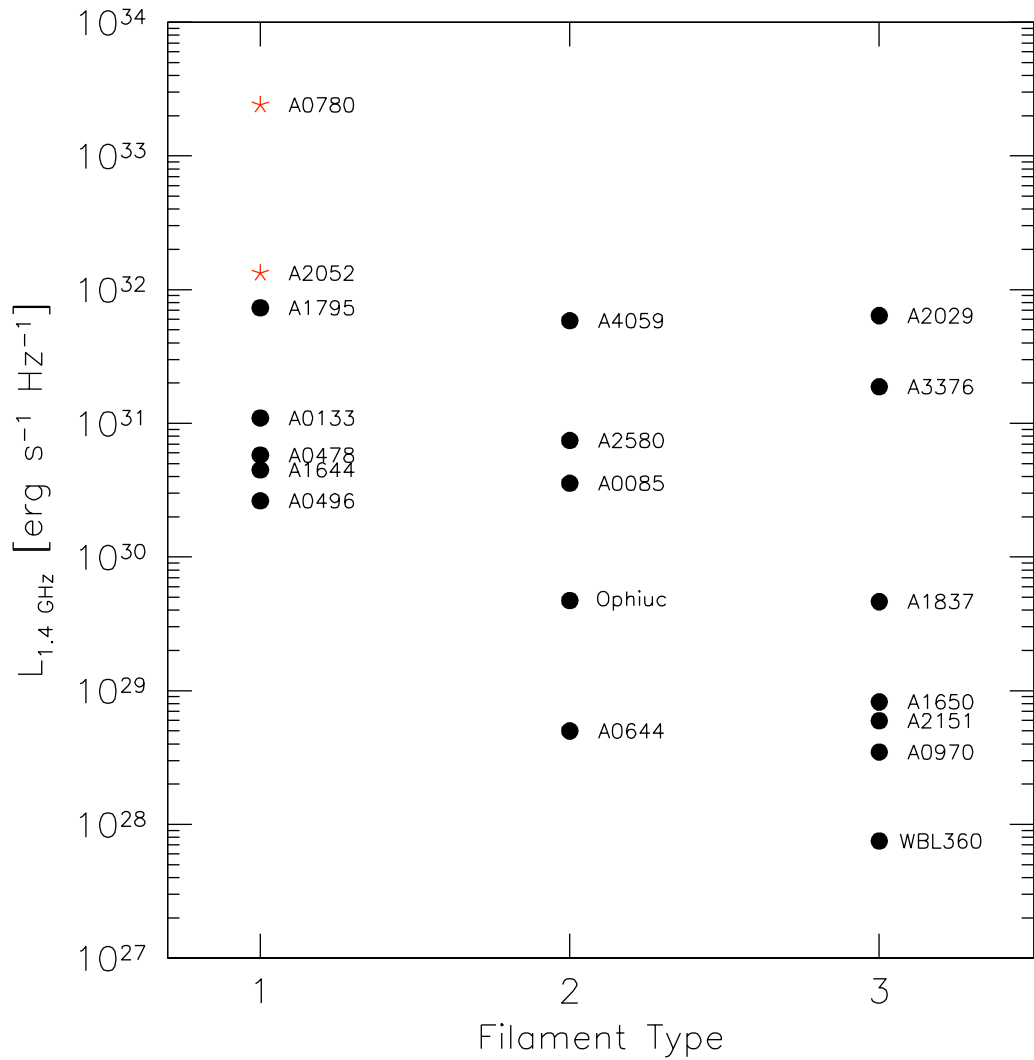
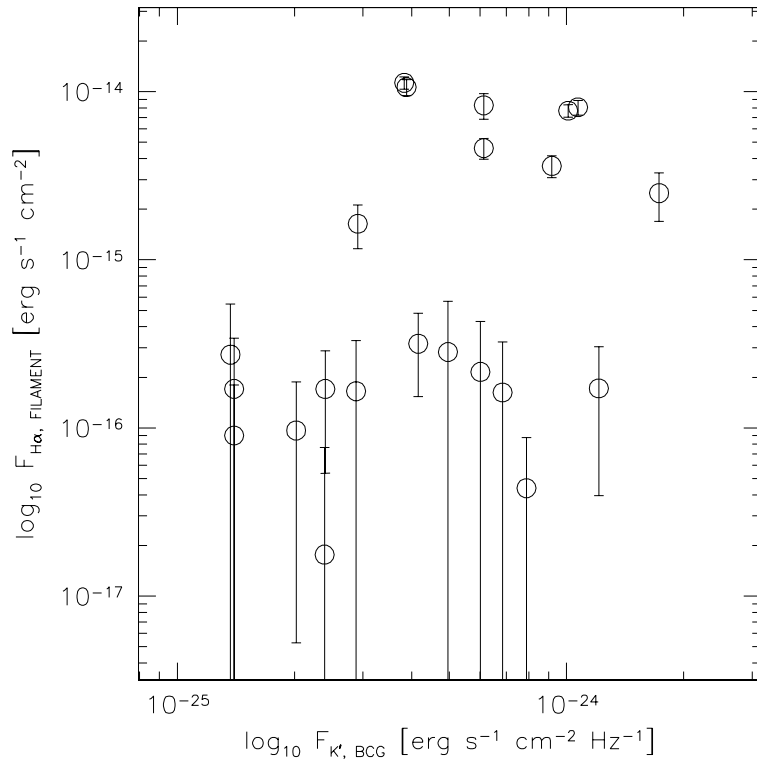


Figure 3.14 1.4 GHz radio luminosity for all clusters detected in the NVSS, as a function of the filament type described in §3.3.1. The red star-shaped points represent the two clusters with an X-ray point source detected in the center, while the filled black circles represent those clusters with no detected X-ray point source. There appears to be little correlation with the radio power and the presence of optical filaments, as 2 of the 6 brightest clusters in radio have no detectable $H\alpha$ emission whatsoever.

that is seen could be due to the fact that cool core clusters, which tend to have $H\alpha$ filaments (Figure 3.8), will also have a more ready supply of fuel for the central AGN, leading to increased radio feedback. Further discussion of the implication of these, and other, results follow in the next section.

We can also consider the relationship between the BCG itself and the presence of optical filaments. Figure 3.15 shows the total K' -band flux for the BCG versus the total $H\alpha$ flux contained in filaments. The K' -band flux is a good approximation to the total stellar mass, with only a very small deviation with galaxy color (Bell & de Jong 2001). There is no obvious correlation between the the galaxy brightness (or stellar mass, approximately) and the presence of $H\alpha$ filaments, suggesting that the observed filaments are related instead to the X-ray properties of the cluster core.



3.4 Discussion: Origin of the $H\alpha$ Filaments

In the previous sections we have provided several new clues to the origin of the observed $H\alpha$ filaments:

- In clusters with filamentary $H\alpha$ emission, we tend to see structure in the cooler (0.5–2.0 keV) X-ray gas. If there is no structure in the X-ray gas, there is typically no accompanying $H\alpha$ emission (Figures 3.4, 3.5).
- There is a strong correlation between the $H\alpha$ flux in filaments and both the X-ray determined cooling flow rate, dM/dt , and cluster entropy over 3 orders of magnitude (Figure 3.8).
- The extent of the $H\alpha$ filaments never exceeds the cooling radius. This appears to be a hard limit to the radius of these filaments (Figure 3.9).
- The metallicity of the X-ray gas coincident with the $H\alpha$ filaments is often lower than the non-coincident ICM at the same radii. The on-filament X-ray metallicity is consistent with that measured near the cooling radius or beyond (Figure 3.12).
- The temperature and cooling time of the X-ray gas coincident with the $H\alpha$ filaments is significantly lower than that of the surrounding ICM (Figure 3.13).

These results suggest a direct link between the hot ICM and the warm ionized filaments. However, before we discuss their implications, we would be remiss if we did not mention the spectacular $H\alpha$ filaments detected in the nearby cooling flow cluster, Perseus. A great deal of literature has been devoted to the study of these filaments, which are seen in molecular gas (Salomé et al. 2008), warm ionized hydrogen (Conselice et al. 2001) and X-ray (Fabian et al. 2006). However, while the

observed filaments are indeed impressive, we would argue that they are “typical” among what we classify as our type I clusters. In Figure 3.16 we show the effect of placing Perseus A at larger redshift, and simulating a 20-minute exposure using the MMTF under typical observing conditions. By a redshift of 0.06, which is roughly the mean redshift of our sample, the majority of the fine structure has been washed out, leaving only a small number of detectable filaments. These redshifted images look similar in morphology to our detections of filaments in the 7 clusters which we label as type I. Additionally, we show in Figure 3.8 that Perseus A occupies a similar space to the other clusters with filamentary $H\alpha$ in temperature, cooling rate and temperature. The total luminosity in $H\alpha$ is significantly higher than in all other clusters, however this is probably again partially due to its proximity: if a filament completely disappears into the background we will choose a smaller aperture and, thus, measure a smaller total luminosity.

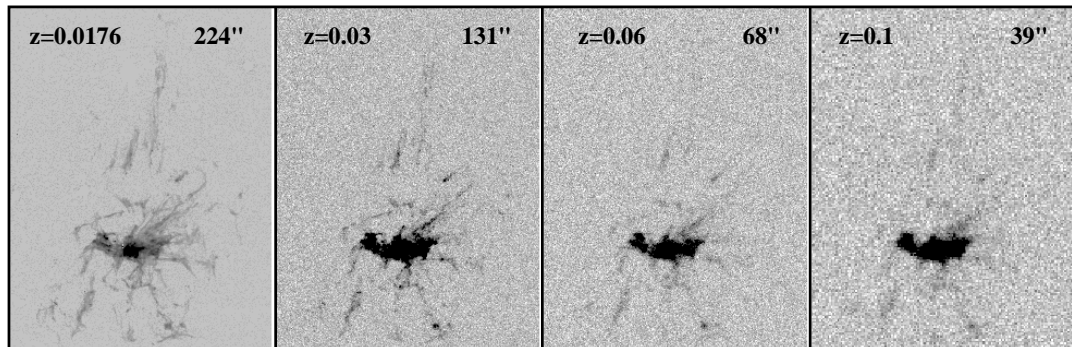


Figure 3.16 Image of Perseus A from Conselice et al. (2001). The image quality has been degraded to simulate the effect of observing this cluster at varying distances. The redshift of observation is in the upper left corner, while the apparent size of the image in the horizontal direction is in the upper right. By the mean redshift of our sample, $z \sim 0.06$, most of the spectacular filaments have been lost, leaving only a few unresolved structures.

We finish by discussing the results summarized above in the context of several current theories which attempt to explain the presence of the observed $H\alpha$ filaments: buoyant radio bubbles, gas sloshing in the central potential, accretion of gas-rich

galaxies, filamentary cooling flows, ICM conduction and magnetic fields.

3.4.1 Origin of the Cool Gas

Buoyant Radio Bubbles

In an effort to explain how an AGN can deposit energy into the ICM and quench cooling, much work has been focused on the evolution of bubbles blown in the ICM by radio jets (e.g., Churazov et al. 2001; Revaz et al. 2008; Reynolds et al. 2005; Vernaleo & Reynolds 2007). Due to the local density contrast, these bubbles are buoyant and will rise to larger radius, transporting energy from small radii to large. While rising, the shape of the bubble evolves and can leave behind a trail of cooler gas that morphologically matches the observed $H\alpha$ filaments in Perseus A (Revaz et al. 2008; Reynolds et al. 2005). Radio bubbles have been observed in several clusters to date, including some in our sample (e.g. Abell 0780, Abell 2052), which lends further support to this scenario.

This scenario is consistent with the low temperatures seen in the X-ray ICM coincident with the $H\alpha$ filaments and with the fact that all of the clusters with extended filaments have non-zero 1.4 GHz flux. Some clusters (e.g. Abell 0780, Abell 2052) show $H\alpha$ emission along the edges of known radio-blown bubbles lending further support to this scenario. It is unclear exactly how the strong correlation between the $H\alpha$ radius and the cooling radius fits in this scenario, although it could be that this relation is tied to the ionization and not to the source of the gas. The low ICM abundance coincident with the $H\alpha$ filaments appears to match well with the abundance beyond the cooling radius, but it may also match the core abundance, which previous works (e.g., Sanders & Fabian 2002, 2007) have found to be metal-poor in several nearby clusters.

Gas Sloshing

The gravitational disruption of a cluster core by mergers or interactions with other clusters or galaxies can lead to the ICM “sloshing” about the central potential, creating cold fronts that have been observed in several clusters to date (e.g., Johnson et al. 2010; Zuhone & Markevitch 2009). While this is certainly an important mechanism for heat transport and is very likely ongoing in several clusters with observed cooling fronts, it does not seem to be a plausible general explanation for the presence of warm filaments. The morphology of the $H\alpha$ filaments in our sample tends to be radial, with very few exceptions. The gas sloshing scenario predicts cool, low-entropy gas along fronts which are aligned perpendicular to the radial direction. The process of sloshing in the cluster core should also smooth out any abundance gradients, however we detect possible abundance contrasts between the X-ray gas on-filament and off-filament. Finally, the magnitude of the gas sloshing should be dependent on the strength of the merger or disruption event. However, we see a clear limit to the length of the filaments ($R_{H\alpha} < R_{cool}$), which is inconsistent with the sloshing picture.

Accretion of Younger Galaxies/Groups

While the direction of some of the observed filaments seemingly coincides with the location of smaller galaxies (e.g. Abell 0478, Abell 0496, Abell 0780), it is unlikely that the warm gas has been stripped from these galaxies. If this were the case, one would expect the filaments to extend all the way to the satellite galaxy, in some cases, which is not seen. Likewise, we would not expect a single galaxy, or small group of galaxies, to have a strong effect on the distribution of the hot X-ray gas. However, much of the structure seen in $H\alpha$ is seen also in the Chandra X-ray images. Additionally, the strong correlation between the mass deposition rate and cluster

entropy would be unexplained by such a formation method.

A back-of-the-envelope calculation seems to rule out this mechanism as the source of the observed $H\alpha$ filaments. The typical $H\alpha$ luminosity that we observe in filaments is $\sim 5 \times 10^{40}$ erg s^{-1} , which corresponds to $\sim 3.7 \times 10^{52}$ recombinations per second (assuming case B recombination). If we assume that the diffuse ionized medium in the stripped galaxy is pure hydrogen and is being stripped from a galaxy like our Milky Way, and then recombining only once as it cools in the absence of ionizing radiation, this corresponds to $\sim 950 M_{\odot} \text{ yr}^{-1}$ of recombining gas. Assuming a total diffuse HII mass of $10^9 M_{\odot}$ for a typical massive spiral (Lequeux 2005), this implies that all of the stripped gas would recombine in ~ 1 Myr. Thus, in order to consistently produce warm ionized filaments via gas stripping, the BCG would have to strip the gas disk from a spiral galaxy every few Myr, which is unreasonably short, given the typical cluster crossing times of ~ 1 Gyr. Alternatively, if we invoke an additional ionization source once the gas has been stripped from the galaxy (e.g. X-ray conduction from the ICM), a smaller amount of stripped gas could lead to the observed fluxes of $H\alpha$. We will revisit this issue in much greater detail in subsequent chapters.

Filamentary Cooling Flows

In this scenario, the observed $H\alpha$ filaments directly trace the cooling flow (e.g., Cowie et al. 1980; Fabian et al. 1984; Heckman et al. 1989). The X-ray ICM begins to cool dramatically at the cooling radius, while falling inwards at roughly the free-fall speed. As the gas cools, small density contrasts in the ICM grow and thin, high-density filaments form. Once sufficiently cool, the gas in these filaments can be re-ionized via star formation, collisional heating (e.g., Ferland et al. 2009) or drag heating (e.g., Pope et al. 2008). This scenario is consistent with $H\alpha$ filaments

extending to R_{cool} , with the observed correlation between X-ray and $H\alpha$ properties and with the low metallicity and high cooling rates found in the X-ray gas coincident with $H\alpha$ filaments. Additionally, the fact that we only see $H\alpha$ filaments out to a radius where gas can cool in 5 Gyr agrees well with observations that the frequency of cool cores beyond a lookback time of 5 Gyr is significantly lower than the local Universe. Thus, the cooling flow scenario is our preferred formation scenario for the optical filaments.

The thinness of the observed $H\alpha$ filaments relative to their extent (Table A.1) is reminiscent of the thin, filamentary structure seen in hydrodynamic simulations of cool gas flows (e.g., Ceverino et al. 2010; Hattori et al. 1995; Pope et al. 2008; Sharma et al. 2010). Figure 3 from Ceverino et al. (2010) shows long (> 50 kpc), thin (< 10 kpc) filaments of cold gas which resemble our observations of $H\alpha$ filaments. While the physical scales are slightly different, they describe the process which cool ($< 5 \times 10^4$ K) filaments embedded in a spherical halo of hot ($> 3 \times 10^5$ K) gas may form. The formation of these cool filaments is used by the authors to explain how star formation proceeds in spiral galaxies at high redshift, but the physical processes should be similar for gas cooling from the hot phase to the cool phase, regardless of whether we are considering gas streaming onto an isolated spiral galaxy or a central cluster galaxy.

In §2 we argued that the most plausible scenario for the creation of the long, thin filament in Abell 1795 was a cooling wake caused by a cooling flow occurring around the moving cD galaxy. This claim was made based on the observation by Oegerle & Hill (2001) that Abell 1795 has a significant peculiar velocity relative to the cluster. However, we find that the second most asymmetric case, Abell 0496, which also has filaments extending only in one direction, has a negligible peculiar velocity. Likewise, several BCGs with no $H\alpha$ emission (e.g., Abell 2029, Abell 2151) or nuclear-only

H α emission (e.g. Abell 2580) have a peculiar velocity as high, or higher, than Abell 1795. Thus, while this may play a role in determining the direction of the filaments, it is not likely the most important factor in their formation.

This scenario makes the prediction that the filament material should be in near free-fall. The jury is still out on this issue, as several works (e.g., Hatch et al. 2007; Oonk et al. 2010) argue against radial infall in H α filaments, while others (e.g., Lim et al. 2008; Wilman et al. 2009) argue for it. Thus, a homogenous sample of kinematic measurements is needed to complement this census of the warm and hot medium and provide a strong argument either for or against the radially-infalling cooling flow.

3.4.2 Evidence for Conduction

Conduction from the X-ray ICM is a promising scenario which could provide the energy necessary to ionize the cooling gas. Nipoti & Binney (2004) predict that, if conduction is responsible for ionizing the H α filaments, there should be an excess of soft X-rays surrounding the filaments. This is consistent with our findings that the soft X-ray morphology matches well with the H α morphology and that the temperature of the X-ray gas coincident with the warm filaments is significantly cooler than the surrounding ICM. In an attempt to address the plausibility of this scenario for ionizing the observed H α filaments in our sample, we turn to a study of thermal conduction in 16 cooling-flow clusters by Voigt & Fabian (2004). Of these 16 clusters, there are 5 which overlap with our sample: Abell 0478, Abell 0780, Abell 1795, Abell 2029 and Sersic 159-03. Of the five clusters in this overlapping sample, four show very extended, filamentary H α emission. The conductivity inside of the cooling radius for these four clusters ranges from $\kappa_{eff}/\kappa_S = 0.3\text{--}2.3$, while for the lone overlapping cluster with no H α emission, the effective conductivity is

$\kappa_{eff}/\kappa_S = 0.2$ (Voigt & Fabian 2004). Estimates of the minimal value required for conduction to transport heat from the hot ICM to cooler regions varies from ~ 0.01 (Malyskin 2001) to 0.3 (Narayan & Medvedev 2001).

The fact that we observe cooler X-ray gas coincident with the H α filaments, coupled with the relatively large conductivity measurements in clusters with filaments (albeit with a small sample size) suggests that conductivity may be responsible for much of the energy required to ionize these filaments. However, future work is needed to expand on the number of clusters with effective conduction measurements and to determine if the energetics of the warm filaments match what we would expect from ICM conduction.

3.4.3 Role of Magnetic Fields

Given the typically large axial ratio of the H α filaments (length/thickness ~ 30 , according to Table A.1), magnetic fields likely play a role in the formation of these filaments, in one or more of several ways: (i) by channeling the inflow of clumps of gas along field lines, giving them coherent structure (Fabian et al. 2003), (ii) preventing the hot, turbulent ICM from shredding the filaments (Hatch et al. 2007), (iii) to help the growth of thermal instabilities, leading to thin high-density filaments (Hattori et al. 1995), and (iv) suppressing conduction of heat from the ICM to the cooling gas (Voigt & Fabian 2004).

High-resolution X-ray spectra of these clusters could constrain the level of turbulence in the ICM (e.g., Sanders et al. 2010). These measurements, combined with the observed thinness of the H α filaments and MHD models could constrain the strength of the intracluster magnetic field required to sustain such filaments, in a similar manner to Loewenstein & Fabian (1990). This would be a nice consistency check on the magnetic field strengths derived from rotation measures.

3.5 Summary and Future Prospects

This study represents the highest resolution survey of warm ionized filaments in cooling flow clusters beyond 100 Mpc to date. Complex, filamentary morphologies are seen in 8/23 (35%) of our clusters, with slightly extended or nuclear emission seen in additional 7/23 (30%). We find a weak correlation between the total H α luminosity and the near-UV luminosity from young stars, which suggests that photoionization from young stars may play a role in producing the observed H α . UV imaging of higher spatial resolution is needed to spatially correlate the H α and UV emission, and to remove the contribution to the UV luminosity from the AGN and/or central starburst. While the H α and X-ray data support the buoyant radio bubble hypothesis as a source of cool gas in some cases, we believe that the cooling flow model does a better job of explaining the properties of the ensemble of clusters. We observe correlations between the soft X-ray morphology and the H α morphology, the X-ray cooling rate and the H α luminosity contained in filaments. We find evidence for a correlation between the X-ray metal abundance of gas coincident with the H α filaments and at the cooling radius, however more data are required in order to obtain reliable on-filament abundance measurements. The maximum radial extent of the H α emission and the cooling radius appear to be linked, such that $R_{H\alpha} < R_{cool}$, where R_{cool} is the radius at which the X-ray gas can cool in less than 5 Gyr. This radius appears to be physically motivated, as the choice of timescale agrees well with the lookback time at which cooling flow clusters begin to emerge. Additionally, we find that the X-ray gas coincident with observed H α filaments is cooling on a much shorter ($\sim 20\%$) timescale than the surrounding ICM. These results suggest that the H α filaments trace the X-ray cooling flow, and that this flow is initiated at the cooling radius. There does not appear to be a strong corre-

lation between the presence of filaments and the structural properties of the BCG, suggesting that the $H\alpha$ filaments are not related to any feedback processes from the central galaxy. Based on our results, we propose that the gas is cooling out of the X-ray ICM in clumps at roughly the cooling radius and collapsing into thin streams as it falls onto the BCG. The observed asymmetry is likely due to the cooling flow being channeled along magnetic field lines. Based on the X-ray and $H\alpha$ correlations, as well as the high effective conductivity in clusters with $H\alpha$ filaments, it is likely that this cool gas is conducting heat from the surrounding ICM in order to remain ionized. Several questions remain unanswered in this scenario, such as the cooling process for the hot gas below ~ 0.5 keV, and the exact ionization mechanism for the warm gas. Upcoming chapters will carefully address these and other issues.

Table 3.2 H α , X-Ray, NUV, and radio properties of 23 cooling flow clusters

Name	File Type	$F_{H\alpha,tot}$	$F_{H\alpha,fil}$	$R_{H\alpha}$	Axial Ratio	kT ₁₀₀	K ₃₀	R_{cool}	M_{spec}	kT _{in} /kT _{out}	Z_{in}/Z_{out}	$R_{X,nuc}$	F_{NUV}	F_{NUV}^c	$F_{1.4}$
(1)	(2)	(3)	(4)	(5)	(6)	(7)	(8)	(9)	(10)	(11)	(12)	(13)	(14)	(15)	(16)
Abell 0133	I	0.11(0.03)	0.03(0.02)	4.2	32.0	3.1	54	50.3	0.0	2.08/2.54	0.95/1.35	3.37	0.41(0.01)	0.04(0.09)	167
Abell 0478	I	2.46(0.25)	0.83(0.14)	13.3	15.9	7.8	68	58.4	0.0	5.28/5.75	0.66/0.84	2.41	3.99(2.56)	3.82(0.04)	37
Abell 0496	I	2.00(0.13)	0.81(0.08)	11.8	23.7	2.8	60	55.9	1.5	1.72/2.52	0.60/1.00	2.24	5.46(0.18)	4.93(0.12)	121
Abell 0780	I	1.60(0.15)	0.16(0.05)	10.9	22.0	3.0	45	61.2	7.5	3.21/2.99	0.66/0.53	0.77	3.24(0.03)	2.84(0.09)	40800
Abell 1644	I	0.97(0.09)	0.36(0.05)	18.1	33.3	2.9	83	31.1	3.2	1.79/2.48	0.45/1.34	1.82	0.97(0.04)	0.51(0.11)	98
Abell 1795	I	3.39(0.17)	1.13(0.10)	56.0	63.7	3.9	60	85.0	7.8	2.99/4.33	0.59/0.53	1.43	2.64(0.01)	2.32(0.07)	925
Abell 2052	I	2.01(0.11)	0.77(0.07)	15.5	41.4	2.2	62	38.5	2.6	1.07/1.94	0.19/0.77	0.64	0.99(0.01)	0.09(0.21)	5500
Sersic 139-03	I	1.79(0.15)	1.06(0.12)	35.3	41.5	2.4	31	58.7	13.4	1.97/2.42	0.42/0.49	1.25	0.97(0.01)	0.71(0.06)	-
Abell 0085	II	0.79(0.08)	0.46(0.06)	4.1	5.9	4.0	47	59.3	2.2	2.65/2.86	0.52/1.48	4.11	0.56(0.02)	0.20(0.08)	57
Abell 0644	II	0.11(0.03)	0.02(0.01)	3.3	1.0	5.4	122	71.1	1.5	-/-	-/-	-	0.02(0.05)	-0.27(0.07)	0
Abell 2580	II	0.22(0.04)	0.01(0.01)	8.0	2.8	-	-	-	-	-/-	-/-	-	0.19(0.01)	0.03(0.04)	46
Abell 3158	II	0.02(0.01)	0.00(0.01)	1.0	2.8	6.4	184	43.6	0.0	-/-	-/-	0.50	0.34(0.01)	0.06(0.07)	-
Abell 3389	II	0.33(0.06)	0.02(0.02)	1.2	1.0	-	-	-	-	-/-	-/-	-	1.66(0.04)	0.50(0.27)	-
Abell 4059	II	0.79(0.08)	0.00(0.00)	6.0	4.5	3.0	77	51.8	0.7	1.59/2.04	0.49/1.15	1.21	0.70(0.02)	0.18(0.12)	1280
Ophiuchus	II	0.87(0.15)	0.25(0.08)	0.1	1.0	13.4	284	31.5	0.0	-/-	-/-	1.63	6.56(1.54)	5.42(0.27)	29
Abell 0970	III	0.01(0.01)	0.01(0.01)	0.2	1.0	-	-	-	-	-/-	-/-	-	-(-)	-(-)	0
Abell 1650	III	0.03(0.03)	0.03(0.03)	0.1	1.0	5.0	91	30.5	0.0	-/-	-/-	1.33	0.13(0.01)	-0.12(0.06)	0
Abell 1837	III	0.04(0.04)	0.03(0.03)	0.3	1.0	-	-	-	-	-/-	-/-	-	0.34(0.06)	-0.07(0.10)	5
Abell 2029	III	0.03(0.03)	0.02(0.02)	0.2	1.0	5.4	67	87.1	3.4	-/-	-/-	2.10	0.54(0.01)	0.17(0.09)	528
Abell 2142	III	0.03(0.03)	0.02(0.02)	0.1	1.0	6.0	83	101.6	1.2	-/-	-/-	-	0.12(0.01)	-0.02(0.03)	0
Abell 2151	III	0.02(0.02)	0.02(0.02)	0.8	1.0	2.2	55	97.3	8.4	-/-	-/-	1.74	0.51(0.02)	0.07(0.11)	2
Abell 3376	III	0.01(0.01)	0.00(0.00)	1.4	1.0	4.3	130	85.7	2.1	-/-	-/-	0.48	0.43(0.02)	0.22(0.05)	261
WBL 360-03	III	0.03(0.03)	0.02(0.02)	0.1	1.0	-	-	-	-	-/-	-/-	-	-(-)	-(-)	0

- (1) Cluster name (2) Filament type, following the convention set out in §3.3.1 (3) Total H α flux, in units of 10^{-14} erg s $^{-1}$ cm $^{-2}$ (4) H α flux contained in filaments, in units of 10^{-14} erg s $^{-1}$ cm $^{-2}$ (5) Maximum radius of H α emission, in units of kpc (6) Ratio of filament length to width, where the width is typically taken to be the PSF FWHM ($\sim 0.6''$) (7) Average X-ray temperature of the cluster in the inner 100 kpc, in units of keV (8) Specific entropy of the gas coincident with the H α filaments to the surrounding ICM derived from a single-temperature plasma model (12) Ratio of flow rate, in units of M_{\odot} yr $^{-1}$ (11) Ratio of X-ray temperatures of the gas coincident with the H α filaments to the surrounding ICM derived from a single-temperature plasma model (13) FWHM of the X-ray metal abundance of the gas coincident with the H α filaments to the surrounding ICM derived from a single-temperature plasma model (14) Total GALEX NUV flux coincident with the BCG, in units of 10^{-27} erg s $^{-1}$ cm $^{-2}$ Hz $^{-1}$ (point source has $R_{X,nuc} \sim 0.7''$). Nucleii which are consistent with point sources are shown in bold. (15) Total GALEX NUV flux coincident with the BCG, with the contribution from old stars removed (following §3.2.2), in units of 10^{-27} erg s $^{-1}$ cm $^{-2}$ Hz $^{-1}$ (16) Radio flux, from the NVSS, in units of mJy.

Chapter 4

The Effect of Environment on the Formation of $H\alpha$ Filaments and Cool Cores in Galaxy Groups and Clusters

4.1 Introduction

The high X-ray surface brightness in the cores of some galaxy clusters suggests that, in the absence of any feedback, radiative cooling should become a runaway process, leading to “cooling flows” of $10\text{--}100 M_{\odot} \text{ yr}^{-1}$ (see review by Fabian 1994). A distinguishing characteristic of cool core clusters is the presence of warm, optical line-emitting gas (Crawford et al. 1999; Hatch et al. 2007; Heckman et al. 1989; Hu et al. 1985; Jaffe et al. 2005). Typically observed at $H\alpha$, this warm gas generally exhibits either a nuclear or filamentary morphology and has been shown to correlate with several properties of the cool core, such as cooling rate and cluster entropy (§3).

Despite the near ubiquity of optical line-emitting nebulae in cool core clusters, their origins remain unclear. In §3 we considered several processes for producing the observed H α morphology, and found that the observations were consistent with two formation scenarios: 1) the warm gas cooled out of the X-ray, and 2) the warm gas was entrained behind buoyant radio bubbles arising from AGN feedback (e.g., Churazov et al. 2001; Revaz et al. 2008; Reynolds et al. 2005; Vernaleo & Reynolds 2007). The high H α surface brightnesses measured in these systems indicate that additional ionization sources are present, allowing the ionized gas to recombine more than once. Crawford et al. (2005) describe potential sources of ionization, the most promising of which are: 1) cosmic ray ionization, 2) heat conduction from the ICM to the colder filaments, and 3) photoionization by hot young stars. In §2 and §3 we provide evidence for both star formation and conduction, respectively, but were unable to rule in favor of a dominant ionization mechanism.

While much effort has gone into quantifying and explaining the presence of warm filaments in clusters, very little work has been done on the environmental dependence of this phenomenon. While massive clusters of galaxies are dominated by gravitational and thermal processes, their low-mass counterparts, galaxy groups, may be dominated by non-gravitational processes such as winds, cooling flows or AGN feedback (Sun et al. 2009). Thus, by considering low-mass systems we can hope to find out whether the observed phenomena are more closely related to global, gravitational processes or more local, baryon physics. In §3, we showed that the properties of the H α filaments were strongly correlated with the properties of the cluster core, such as the cooling rate, cooling radius, entropy and temperature. However, most of these trends only cover a small range in X-ray properties, since §3 only considered clusters.

In an effort to properly evaluate the dependence of the H α filaments on environ-

ment, we have conducted a survey of 10 galaxy groups using the Maryland Magellan tunable filter (hereafter MMTF; Veilleux et al. 2010). We combine this sample of 10 groups with a subset of 17 clusters drawn from §3. In §4.2, we describe this sample in more detail, along with the data acquisition and analysis. In §4.3, we present the results of this study, re-examining several trends found by §3, and also exploring new issues. In §4.4 we discuss the implications of these results and postulate on the origin and power source of these warm filaments. Finally, in §4.5 we conclude and discuss prospects for future studies.

Throughout this chapter, we assume the following cosmological values: $H_0 = 73$ km s⁻¹ Mpc⁻¹, $\Omega_{matter} = 0.27$, $\Omega_{vacuum} = 0.73$.

4.2 Data Collection and Analysis

4.2.1 Sample Selection

The goal of this study is to extend our investigation of H α filaments (§3) from the cluster to group environment. Thus, we begin with a sample drawn from §3, of 17 cool core clusters. These clusters were originally chosen from the larger sample of White et al. (1997). This large sample, much like any X-ray selected sample, is inherently biased towards cool cores due to their higher surface brightness. The full sample of 207 clusters (White et al. 1997) was reduced based on the following criteria: 1) visible with the Magellan telescope ($\delta < 35^\circ$); 2) appropriate redshift to be imaged at H α with MMTF ($0.0 \leq z \leq 0.09$). From this reduced sample, we choose 17 clusters with high-quality Chandra imaging, covering three orders of magnitude in classical cooling rate. These clusters were chosen to yield a relatively flat distribution of cooling rates, ensuring that we covered the full gamut of cool core and non cool core clusters. This selection technique will, of course, introduce a

significant bias, the effects of which will be discussed later in §4.4. The 17 selected clusters all have deep H α imaging from MMTF, as presented in §3.

From the sample of 43 galaxy groups defined by Sun et al. (2009), we chose at random 10 groups which obey the same criteria as above, with average temperatures ranging from 0.7–3 keV, to add to this sample. Unlike the White et al. (1997) sample, this collection of 43 galaxy groups is not based solely on X-ray detections of clusters. Sun et al. (2009) include AGN-selected and optically-selected groups, removing much of the bias towards cool cores that affects X-ray selected catalogs. Thus, the 10 groups in our sample should be relatively unbiased in mass, temperature and cooling rate.

The full sample is listed in Table 4.1. We discuss below the processing of the new MMTF H α observations and the archival Chandra X-ray data.

4.2.2 H α : MMTF

MMTF has a very narrow bandpass ($\sim 5\text{--}12\text{\AA}$) which can be tuned to any wavelength over $\sim 5000\text{--}9200\text{\AA}$ (Veilleux et al. 2010). Coupled with the exquisite image quality at Magellan and the wide field of the Inamori-Magellan Areal Camera & Spectrograph (IMACS), this instrument is ideal for detecting emission-line filaments in galaxy groups and clusters. In §3 we presented deep MMTF H α observations of 23 clusters (17 of which have high-quality CXO data). As a follow-up to that project, we have observed an additional 10 groups during 2009-10 at both H α ($\lambda=6563\text{\AA}$) and continuum ($\pm 60\text{\AA}$), for a total of 40 minutes each with the largest available bandpass ($\sim 12\text{\AA}$). The typical image quality for these exposures was $0.6 \pm 0.2''$. These data are a significant improvement on previous narrow-band imaging of cluster cores due to the very narrow ($\sim 10\text{\AA}$) bandwidth of the MMTF. This allows us to isolate and measure the flux of the H α line without making any assumptions

Name	RA	Dec	z	E(B-V)	kT
(1)	(2)	(3)	(4)	(5)	(6)
<u>Clusters</u>					
Abell 0085	00h41m50.470s	-09d18m11.26s	0.0557	0.038	5.6 ⁽¹⁾
Abell 0133	01h02m41.760s	-21d52m55.50s	0.0569	0.019	3.5 ⁽¹⁾
Abell 0478	04h13m25.274s	+10d27m54.80s	0.0881	0.517	7.1 ⁽¹⁾
Abell 0496	04h33m37.850s	-13d15m42.73s	0.0329	0.132	4.8 ⁽¹⁾
Abell 0644	08h17m25.610s	-07d30m44.94s	0.0704	0.122	6.5 ⁽¹⁾
Abell 0780	09h18m05.671s	-12d05m43.51s	0.0539	0.042	4.7 ⁽¹⁾
Abell 1644	12h57m11.608s	-17d24m33.94s	0.0475	0.069	5.1 ⁽¹⁾
Abell 1650	12h58m41.512s	-01d45m41.05s	0.0846	0.017	5.1 ⁽¹⁾
Abell 1795	13h48m52.491s	+26d35m33.85s	0.0625	0.013	5.3 ⁽¹⁾
Abell 2029	15h10m56.113s	+05d44m41.81s	0.0773	0.040	7.3 ⁽¹⁾
Abell 2052	15h16m44.501s	+07d01m18.21s	0.0345	0.037	3.4 ⁽¹⁾
Abell 2142	15h58m20.026s	+27d14m00.42s	0.0904	0.044	10.1 ⁽¹⁾
Abell 2151	16h04m35.825s	+17d43m17.81s	0.0351	0.043	3.7 ⁽¹⁾
Abell 3158	03h42m52.995s	-53d37m52.40s	0.0597	0.015	5.3 ⁽¹⁾
Abell 3376	06h02m09.717s	-39d56m59.20s	0.0597	0.056	3.5 ⁽¹⁾
Abell 4059	23h57m00.716s	-34d45m32.70s	0.0475	0.015	3.0 ⁽²⁾
Ophiuchus	17h12m27.691s	-23d22m10.41s	0.0285	0.588	8.6 ⁽¹⁾
<u>Groups</u>					
Abell 0744	09h07m20.518s	+16d39m06.70s	0.0729	0.034	2.5 ⁽³⁾
Abell 1139	10h58m11.004s	+01d36m16.49s	0.0398	0.031	2.2 ⁽³⁾
Abell 1991	14h54m31.512s	+18d38m32.57s	0.0587	0.025	2.9 ⁽³⁾
MKW4	12h04m27.082s	+01d53m45.92s	0.0200	0.017	1.8 ⁽³⁾
NGC 1132	02h52m51.830s	-02d43m30.97s	0.0231	0.055	1.1 ⁽³⁾
NGC 3402	10h50m26.093s	-13d09m17.89s	0.0153	0.039	0.8 ⁽³⁾
NGC 4325	12h23m06.665s	+10d37m16.43s	0.0257	0.023	1.0 ⁽³⁾
RBS 461	03h41m17.544s	+15d23m47.80s	0.0290	0.150	2.2 ⁽³⁾
Sersic 159-03	23h13m58.627s	-42d43m38.64s	0.0580	0.011	2.7 ⁽³⁾
UGC 842	01h18m53.621s	-02d59m52.91s	0.0452	0.040	1.8 ⁽³⁾

Table 4.1 Properties of our sample of galaxy groups and clusters. X-ray temperature measurements (last column) are all from the literature – the superscript identifies the source: (1) Spatially averaged temperature (White et al. 1997), (2) Spatially averaged temperature within 100 kpc (§3), and (3) Temperature at r_{2500} (Sun et al. 2009). This sample covers a broad range in temperature, with values ranging from 1–10 keV.

about the $[\text{N II}]/\text{H}\alpha$ ratio.

These new data were fully reduced in exactly the same way as the §3 data, using the MMTF data reduction pipeline¹, which performs bias subtraction, flat fielding, sky line removal, cosmic ray removal, astrometric calibration and stacking of multiple exposures (following Bland-Hawthorn & Jones 1998; Veilleux et al. 2010). The continuum image was then PSF and intensity matched to the narrow-band images to allow for careful continuum subtraction. The stacked images were calibrated using spectrophotometric standards from Oke (1990) and Hamuy et al. (1994, 1992). The error associated with our absolute photometric calibrations is $\sim 15\%$, which is typical for tunable filters and spectrographs. Finally, the data were corrected for Galactic extinction, following Cardelli et al. (1989) using reddening estimates from Schlegel et al. (1998). We do not attempt to correct for intrinsic extinction since the dust content of the optical filaments is not well known. All of these procedures are described in detail in Veilleux et al. (2010).

For systems with complicated morphologies, $\text{H}\alpha$ fluxes were measured by creating (by eye) a region which generously traced the $\text{H}\alpha$ emission and calculating the total signal within this region. For more symmetric morphologies, a circular aperture centered on the emission peak was used, with the radius chosen to contain all of the obvious emission. We show in §3 that this technique yields fluxes that agree relatively well with those in the literature.

¹<http://www.astro.umd.edu/~veilleux/mmtf/datared.html>

4.2.3 X-Ray: *Chandra*

Archival data from the *Chandra X-ray Observatory* were retrieved for all 10 of our sample groups. In order to ensure a homogeneous treatment of the X-ray data, the clusters data were re-reduced alongside the groups data. These data were re-processed with CIAO (version 4.1.2) and CALDB (version 4.1.1) using the latest time-dependent gain adjustments and maps to create new level 2 event files. Due to the large angular extent of some of the groups and clusters in our sample, we were required to construct blank-sky background event files, using the ACIS blank-sky background database, to properly account for background flux. The new level 2 event files were cleaned for flares, using the *lc_clean* routine, by examining the light-curve and removing any spurious bursts in intensity. These data cleaning and calibration procedures are all outlined in detail in the CIAO science threads².

In order to separate the filaments or other substructures from the X-ray halo, we applied an unsharp mask to each image, subtracting a 10'' Gaussian smoothed image from a 1.5'' Gaussian smoothed image. The resulting image highlights any fine structure in the X-ray morphology (see Figure 4.1).

For each object, background-subtracted spectra were extracted using *dmextract*. Updated response files were created using *mkacisrmf* and *mkwarf*, following the CIAO science threads. Counts were grouped into bins with 20 counts per bin, over the range 0.3 to 11.0 keV. Spectra were extracted in a variety of regions to better understand the relationship between the ICM and the H α emission. These regions include: i) circular annuli, with spacing chosen so that $r_{out}/r_{in} = 1.25\text{--}1.6$ (following Sun et al. 2009, and §3 of this thesis), ii) Coincident with the H α -emitting filaments, and iii) the regions surrounding, but not overlapping with, the

²<http://cxc.harvard.edu/ciao/threads/>

H α -emitting filaments.

In order to derive physical quantities from the X-ray spectra, we used the XSPEC spectral fitting package (Arnaud 1996). For the circular annuli, we first deproject the data in each radial bin using the direct spectral deprojection method (DSDEPROJ; Russell et al. 2008). We then model the spectra with a combination of photoelectric absorption (PHABS) and thermal brehmsstrahlung emission from a hot diffuse gas (MEKAL). This combination of models has 3 free parameters which describe the state of the ICM: T_X , n_e , and Z . In order to measure the strength of the ICM cooling, we also allow for an additional component which represents gas cooling over a range of temperatures (MKCFLOW), which has an additional free parameter, dM/dt .

For a more complete description of the spectral extraction and modeling techniques, the reader is directed to §3.

4.3 Results

4.3.1 Warm Ionized Filaments

The primary strengths of MMTF are its large field of view and excellent angular resolution. These make it ideally suited to search for thin, extended filaments in the cores of clusters, as we showed in §3. Our previous study of galaxy clusters (§3) revealed a wide variety of filament morphologies, leading us to develop a classification scheme to help with the analysis of such a diverse sample. We found that 35% of clusters exhibited thin, extended H α filaments (type I), 30% had nuclear or only marginally extended H α emission (type II), and 35% had no detectable H α emission at all. We adopt this same nomenclature for our new sample of 10 galaxy groups, finding very similar ratios between the three types (30% : 30% : 40%). The similar frequency with which we detect H α filaments in groups compared to clusters

suggests a similar formation mechanism.

In Figure 4.1 we show the new data for 10 galaxy groups. For all 10 groups in this sample we show the MMTF red continuum, smoothed CXO, unsharp masked CXO, and MMTF H α images. Just as we saw for clusters, the presence of complex morphology in the X-ray appears to correlate with the presence of H α filaments. We find that all three clusters with strongly asymmetric residuals in the unsharp masked X-ray images have extended H α filaments. We will investigate this relationship between the X-ray and H α data further in the following sections.

Of particular interest in Figure 4.1 is the morphology of the H α emission for Abell 1991 and NGC 4325 (Sersic 159-03 was discussed in §3). Abell 1991 has an arrow-shaped morphology, extending north from the BCG nucleus. This morphology is reminiscent of a bow-shock. We find that the arrow-head corresponds to a bright blob of soft X-rays, while the peak of H α emission at the base of the arrow has no X-ray counterpart. The second interesting group, NGC 4325, exhibits several distinct, radial filaments. This complex morphology strongly resembles the core of the Perseus cluster. Unlike Perseus, the central galaxy in NGC 4325 is almost completely isolated and the total X-ray mass is an order of magnitude lower. This suggests that the global properties of the group/cluster plays only a minor role in the presence and morphology of H α emission.

4.3.2 Global and Core X-Ray Properties

In order to compare properties of groups and clusters, we adopt a scale radius at which we measure quantities such as temperature, density, entropy and enclosed mass. The radius we use, r_{2500} , is the radius at which the average enclosed density is 2500 times the critical density of the Universe. This radius is considerably smaller than the more commonly used value of r_{500} , however we prefer using r_{2500} due

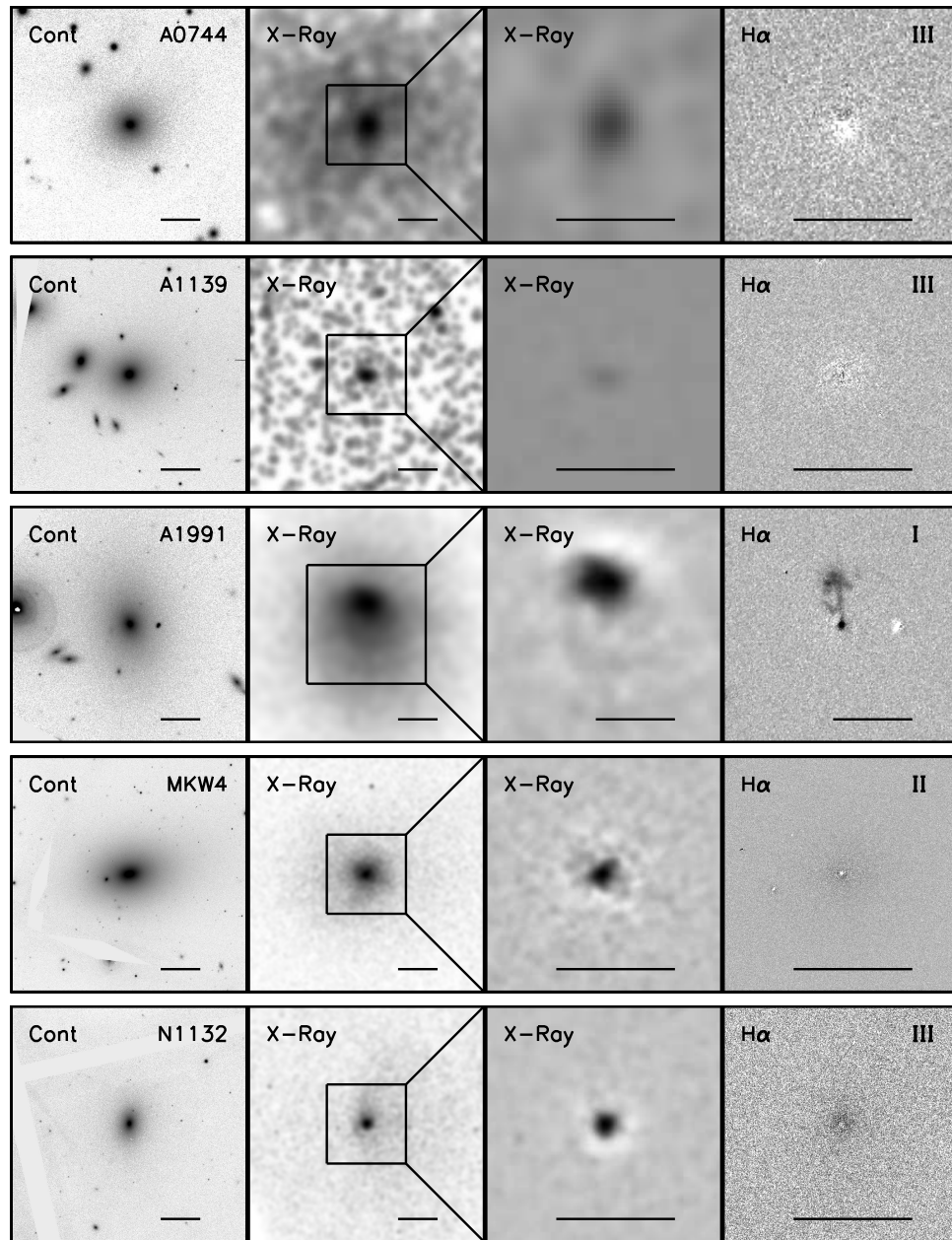


Figure 4.1 X-ray and optical data for the 10 groups in our sample. From left to right the panels are: 1) MMTF red continuum image, 2) CXO X-ray image, 3) Unsharp masked CXO X-ray image, 4) MMTF continuum-subtracted $H\alpha$ image. The horizontal scale bar in all panels represents 20 kpc. The X-ray and red continuum images are on the same scale, and the unsharp masked and $H\alpha$ images are on the same zoomed-in scale. The square region in the X-ray panels represents the field of view for the zoomed-in panels. The grayscale in all images is arbitrarily chosen in order to enhance any morphological features.

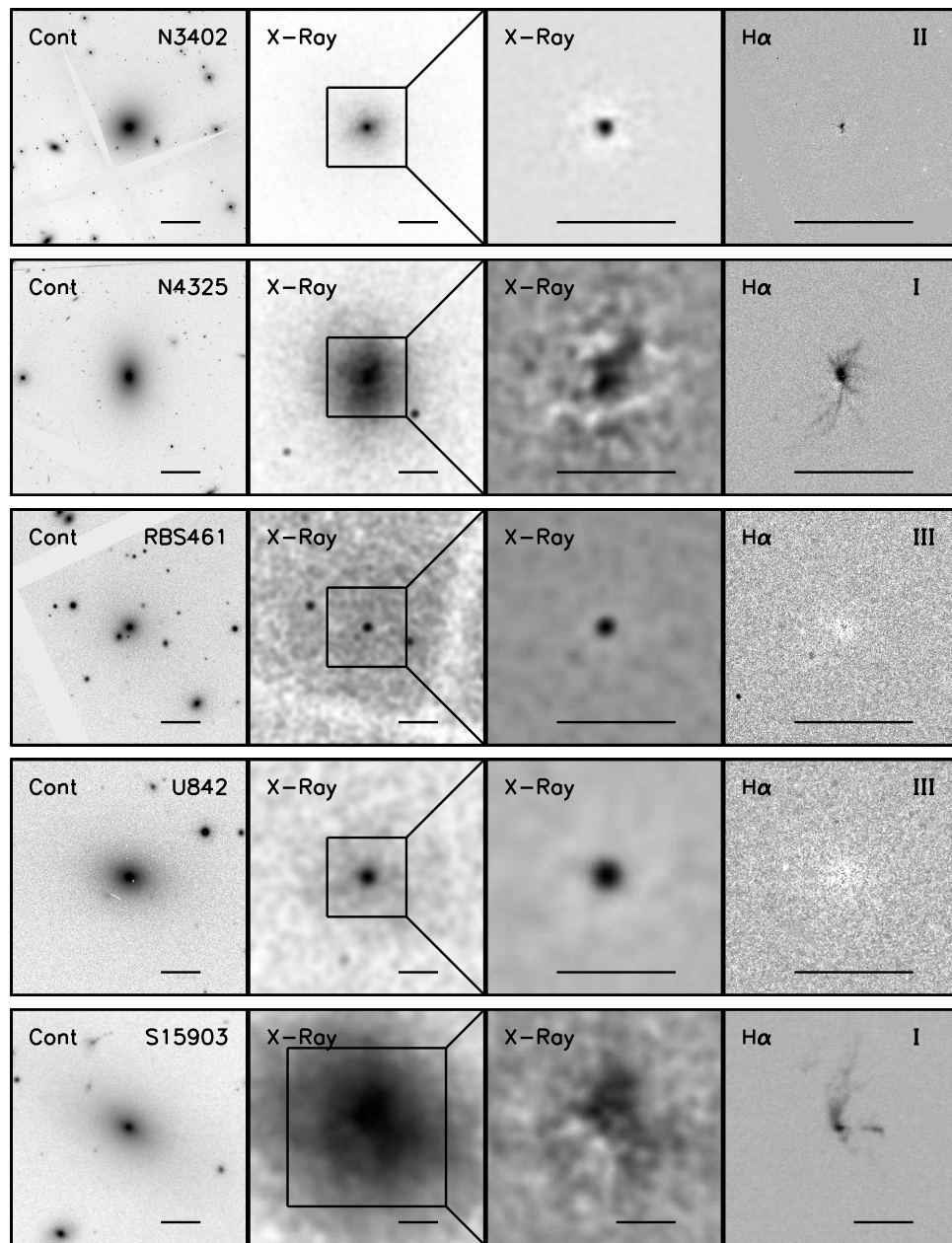


Figure 4.1 Continued.

to our ability to directly measure quantities at r_{2500} (which we will refer to as “global” parameters), rather than infer them indirectly from other measurements. The typical value of r_{500} for the groups in our sample is ~ 600 kpc (Sun et al. 2009), which corresponds to a diameter of $\sim 20'$ at a typical redshift of 0.05 – larger than the typical *CXO* field of view. Thus, we choose a smaller radius at which we can measure various properties for all of the groups and clusters in our sample.

In Figure 4.2 we plot various X-ray scaling relations for our full sample. For systems in hydrostatic equilibrium, we expect a direct correlation between the total enclosed mass and the gas temperature for a given radius, which we observe in general. However, we also find several systems which deviate from this relation. This is because clusters are often not fully in hydrostatic equilibrium due to processes such as AGN feedback or mergers. Nevertheless, these scaling relations show the broad range in parameters covered by the groups and clusters in this sample.

At a glance, Figure 4.2 offers no new insight into the presence of $H\alpha$ filaments. We detect $H\alpha$ in systems at all temperature, mass and entropy, with no obvious bias. To further quantify this, we consider both the fraction of systems with non-zero $H\alpha$ flux and those with extended $H\alpha$ filaments as a function of global X-ray properties in Figure 4.3. We have chosen the binning such that the number of systems in each bin are roughly equivalent. In each panel, we show the F-test likelihood that the histogram is flat, compared to monotonically increasing or decreasing. This statistic confirms that, at the 87% confidence level, the presence of $H\alpha$ emission is uncorrelated with the global temperature. Additionally, we find only a weak correlation between the presence of $H\alpha$ emission and system mass (52% confidence level).

We note that, in higher mass/temperature systems, the fraction of systems with $H\alpha$ emission is likely an upper limit, due to our bias towards cool cores in these

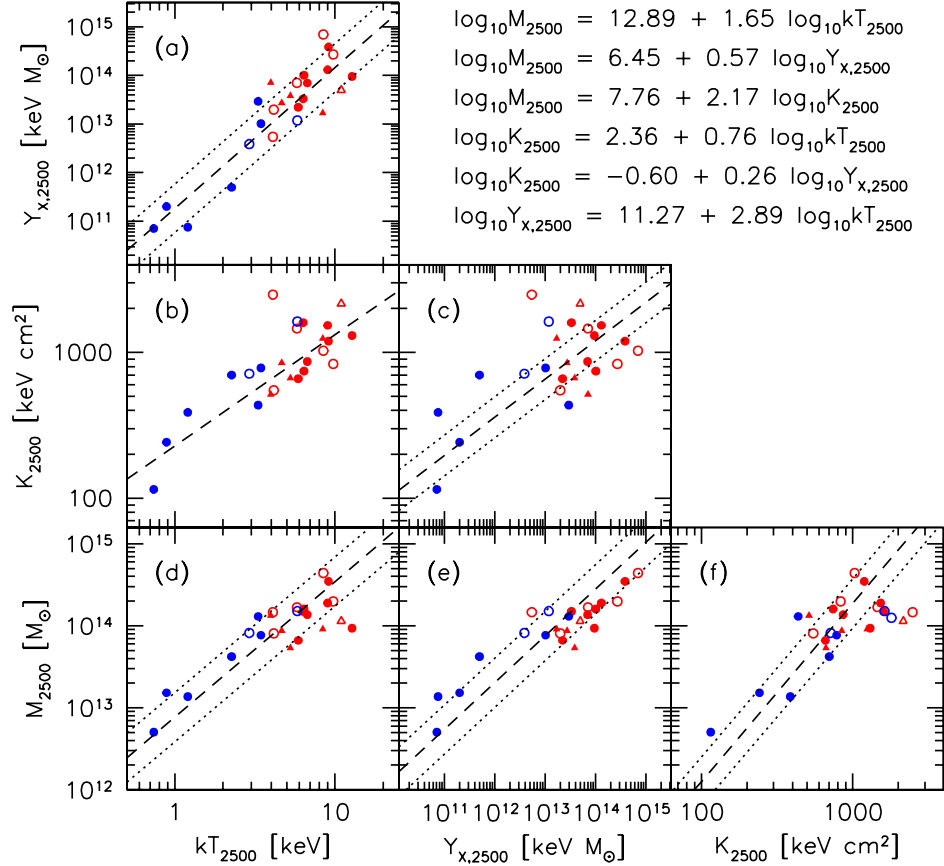


Figure 4.2 X-ray scaling relations for the 10 groups (blue) and 17 clusters (red) in our sample. The addition of groups to our sample allows us to probe the low temperature, mass and entropy regime. We differentiate between systems with $H\alpha$ emission (filled circles) and those without (open circles). Systems that are clearly disturbed either by mergers or AGN feedback are depicted by triangles and typically have under-estimated M_{2500} . The high-temperature, undisturbed outlier in panel (d) is Ophiuchus, which lies in the Galactic plane and, thus, suffers from heavy extinction. The high-entropy outlier in panels (b), (c) and (f) is Abell 2151, which requires the largest extrapolation from the last data point to r_{2500} , and thus has the least constrained properties. For comparison, we show relations derived from Sun et al. 2009a for several of the same systems (dashed lines). We show the functional form of these relations in the upper right corner. The scatter in these relations (dotted lines) represents our uncertainty in converting quantities from r_{500} to r_{2500} . For panel (b), we plot the exact relation quoted by Sun et al. 2009a.

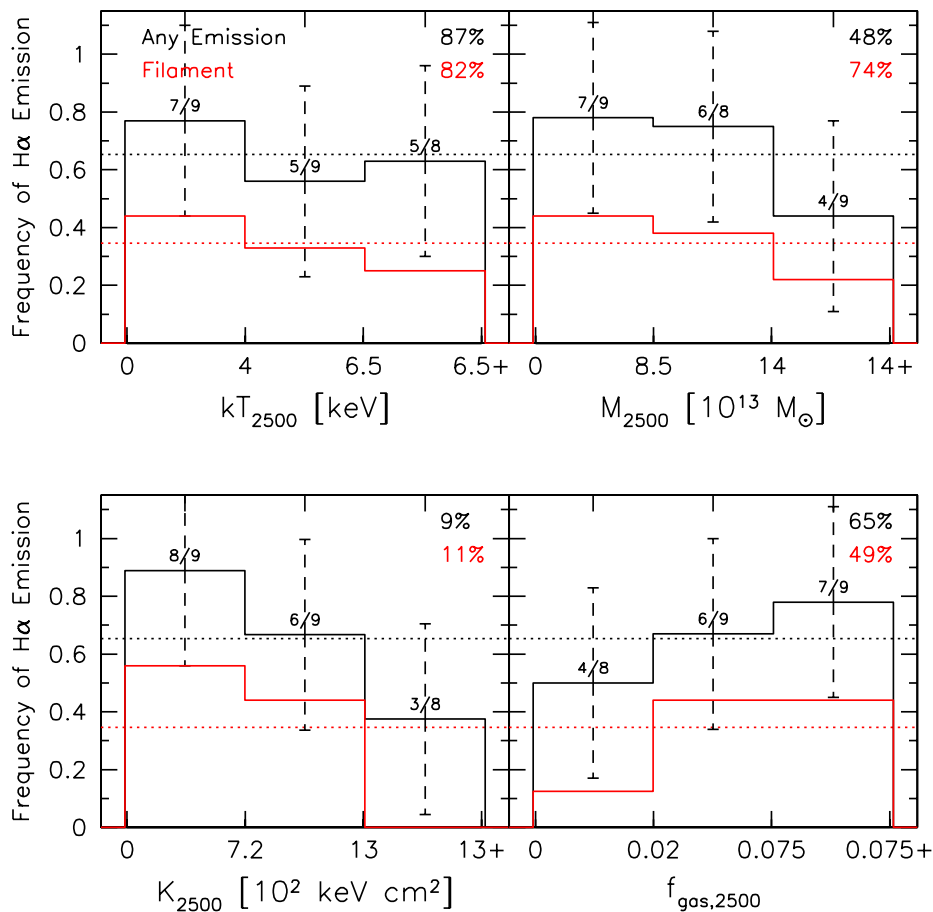


Figure 4.3 Frequency with which we observe H α emission in clusters and groups, as a function of the global X-ray properties. The black histograms show the frequency with which we detect any H α emission whatsoever, while the red histograms show the frequency with which we detect extended H α filaments. The horizontal lines represent the overall detection rate, while the vertical errorbars represent the 1- σ uncertainty in a given bin. The absolute number of systems in each bin are shown above the black histograms. We find that there is no measurable correlation between the global temperature and the presence of H α emission. There is a weak correlation between the presence of H α and the global mass, and stronger correlations with both entropy and gas mass fraction, however these are at the $< 1\text{-}\sigma$ level. The black and red numbers represent the F-test confidence with which we can reject the hypothesis of a steadily rising/falling distribution in favor of a flat distribution, for all H α emission and emission in filaments, respectively.

systems. Thus, while there is only a weak correlation between the presence of $H\alpha$ emission and the global mass, the trend would likely be strengthened by the inclusion of high mass, non cool-core systems which we would not expect to emit at $H\alpha$ based on our previous work (§3).

The bottom two panels of Figure 4.3 show the distribution of the entropy and the gas mass fraction for systems with non-zero $H\alpha$ flux or with extended $H\alpha$ filaments. We find a correlation between entropy and the presence of $H\alpha$ filaments (89% confidence level). We find that 12 of the 15 systems with $K < 900 \text{ keV cm}^2$ show filaments, while only 5 of the 11 systems with $K > 900 \text{ keV cm}^2$ show filaments. This is consistent with findings by previous studies (Cavagnolo et al. 2008, §3 of this thesis) which show that low-entropy systems tend to have more star formation and optical line emission. Finally, we observe very few systems with $H\alpha$ filaments and very low X-ray gas mass fractions, suggesting that the two gas phases are related (51% confidence level). This seems to favor the hypothesis that the warm ionized gas is intimately linked to the hot gas – a certain threshold amount of hot gas is needed in order for $H\alpha$ filaments to exist. In summary, Figure 4.3 suggests that the presence of $H\alpha$ emission is only weakly dependent on the global mass (and thus, temperature) of the system. However, the state of the ICM (i.e. entropy, fractional gas mass) may help dictate whether these filaments can exist.

In §3, we provided evidence that the observed $H\alpha$ filaments were intimately linked to the X-ray cooling. Thus, we re-examine the properties of the group/cluster cores, where the gas is cooling on a short timescale. Figure 4.4 provides similar histograms to those described above, but now considering only measurements taken in the group/cluster core. We calculate the frequency of $H\alpha$ emission as a function of the 1.4 GHz radio power, which traces AGN feedback, the X-ray cooling rate, the average temperature within the central 100 kpc, and the entropy at a radius

of 50 kpc. We find a weak correlation between the 1.4 GHz luminosity and the presence of H α filaments (56% confidence level). In contrast, the correlation with the X-ray cooling rate is significantly stronger (72%), as we also found in §3. This suggests that the ionized filaments are linked more closely to the cooling ICM than to the radio-loud AGN. In the lower panels, we see a much stronger dependence on temperature and entropy when we move to smaller radius. There appear to be very few systems with H α filaments and high temperature/entropy in the inner regions. This confirms our findings from §3 that the presence of H α filaments correlates with the temperature (55% confidence level) and entropy (84% confidence level) inside of the cooling radius. The results of Figure 4.4 are not strongly affected by our selection biases. The missing clusters, which should be high-mass with no cool core, should have high entropy and temperature in the inner 100 kpc. Since we expect these non-cooling systems to lack H α emission, the trends would remain the same.

The combination of Figures 4.3–4.4 suggests that the presence of H α filaments is a function of the state of the ICM inside of $\sim r_{cool}$ and is largely independent of the global properties much beyond this.

4.3.3 X-Ray – H α Correlations

In §3 we provided several pieces of evidence which link the observed H α filaments to the X-ray cooling. With the addition of 10 additional low-mass systems, it is relevant to return to these results and ensure that they are still significant.

In Figure 4.5 we plot both the total H α luminosity and the H α luminosity in filaments as a function of various X-ray properties of the cool core. In §3 we found that systems with warm cores ($kT_{100} > 4.5$ keV) do not emit at H α , while systems with cool cores can have H α emission, but not always. This trend is preserved by including cooler systems (blue points). Additionally, we saw correlations between

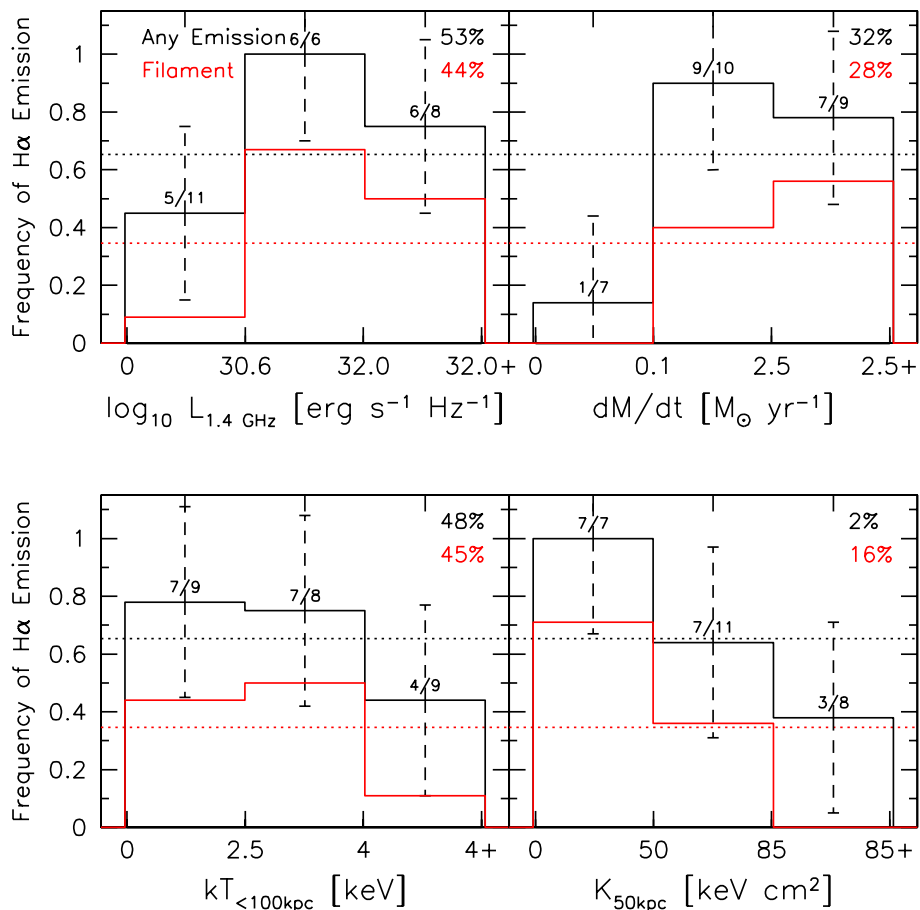


Figure 4.4 Frequency with which we observe H α emission in clusters and groups, as a function of the X-ray properties in the group/cluster core. The black histograms show the frequency with which we detect any H α emission whatsoever, while the red histograms show the frequency with which we detect extended H α filaments. The horizontal lines represent the overall detection rate, while the vertical errorbars represent the 1- σ uncertainty in a given bin. The absolute number of systems in each bin are shown above the black histograms. We find that the correlation between H α and 1.4 GHz flux to be slightly weaker than between the H α flux and the X-ray cooling rate. We also see anti-correlations between the presence of H α emission and the core temperature and entropy, as reported in §3. The black and red numbers represent the F-test confidence with which we can reject the hypothesis of a steadily rising/falling distribution in favor of a flat distribution, for all H α emission and emission in filaments, respectively.

the $H\alpha$ luminosity in filaments and the X-ray cooling rate and core entropy values. These trends are strengthened by the addition of low-mass systems, which exactly follow the distribution of high-mass systems. The strong correlation between the $H\alpha$ luminosity and the X-ray cooling rate suggests a direct link between the cooling ICM and the warm gas.

In addition to a correlation between the mass of gas cooling below the hot phase and the mass of warm gas, we also found, in §3, a correlation between the extent of the warm gas and the cluster cooling radius. The addition of 10 additional groups to this result (Figure 4.6) further strengthens our claim that the size of the $H\alpha$ filaments do not exceed the cluster cooling radius. Since the location of the cooling radius is dependent on an arbitrarily-assigned cooling time, we have tested cooling times of both 3Gyr and 5Gyr. While §3 showed that a cooling radius based on $t_{cool} = 5\text{Gyr}$ matched the data well, we show in Figure 4.6 that $t_{cool} = 3\text{Gyr}$ does a significantly better job of defining the maximum radius of $H\alpha$ emission. The fact that we do not see $H\alpha$ emission beyond the radius at which the hot ICM is cooling in less than 3Gyr suggests a natural timescale for the formation of these filaments.

In §4.2.3, we discussed the procedure of extracting X-ray spectra coincident to and surrounding the observed $H\alpha$ filaments. Since we are unable to determine the 3-dimensional shape of these filaments, we attempt to model them using two different geometries: 1) thick slabs of gas extending into the sky for the full length of the cluster, modeled with a single-temperature plasma, and 2) thin, cylindrical filaments that are modeled with a two-temperature plasma to account for the background/foreground gas seen in projection. In Figure 4.7, we show the results of this exercise for the groups and clusters in our sample which exhibit extended filaments. As we found in §3, the X-ray gas coincident with the $H\alpha$ filaments (labeled “in”) appears to be cooling faster than the surrounding ICM (labeled “out”). Assuming

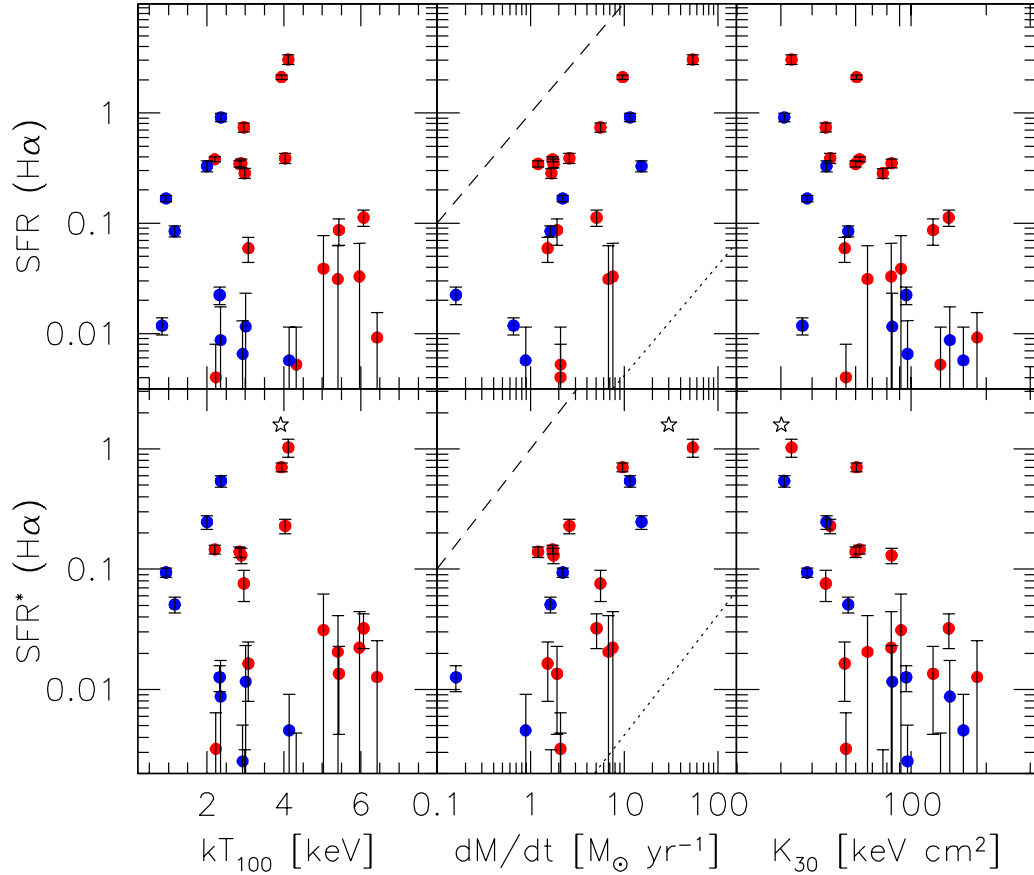


Figure 4.5 $H\alpha$ luminosity, quoted as a star formation rate based on Kennicutt (1998), plotted against the average temperature in the inner 100 kpc (kT_{100}), specific entropy at 30 kpc (K_{30}), and the integrated mass deposition rate (dM/dt). Red points in this plot represent clusters from §3, while the blue points refer to the groups sample in this chapter. The SFRs in the lower panels have had the nuclear contribution removed (SFR^*). The open star in the lower panels refers to Perseus A (Conselice et al. 2001; Sanders et al. 2004). The diagonal dashed line represents the limit where all of the cooling X-ray gas turns into stars, while the dotted line is the case where all of the cooling X-ray gas is made up of hydrogen which recombines only once (Fabian et al. 1984).

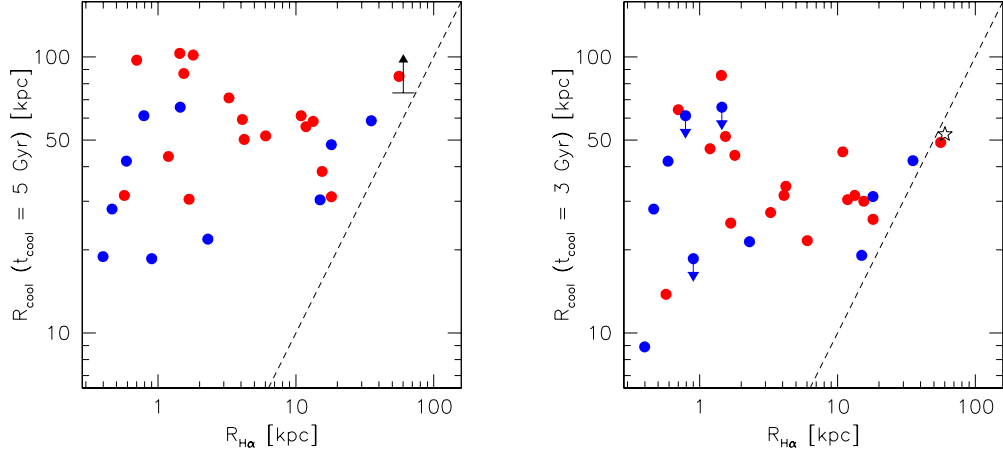


Figure 4.6 Left: Correlation of R_{cool} , the radius at which the cooling time of the ICM reaches 5Gyr; and $R_{H\alpha}$, the largest radius at which we detect $H\alpha$ emission. When there was no detected $H\alpha$ emission an upper limit of the seeing FWHM has been enforced. The dashed line refers to the one-to-one case, while the point colors refer to the clusters from §3 (red) and the groups from this chapter (blue). There appears to be an upper limit on the radius of $H\alpha$ filaments, corresponding to the cooling radius. The black point represents a lower limit estimate on the cooling radius of Perseus A (Conselice et al. 2001; Fabian et al. 2000). Right: Similar to plot on the left, but using a cooling time of 3Gyr to define the cooling radius. Perseus, Abell 1795, and Sersic 159-03 lie almost exactly on the 1-to-1 line in this case.

thin-filament geometry, the X-ray temperature of the filaments is $\sim 20\text{--}50\%$ that of the off-filament gas at the same radius for most of the systems. Additionally, both the entropy and cooling time of the filaments is roughly an order of magnitude smaller for gas in the filaments than off-filament gas at similar radii. Even if we assume that the “filaments” are sheets seen in projection, we infer a cooling time half as long for in-filament gas. We find no significant difference in the filament properties between groups and clusters, suggesting that they share the same formation mechanism.

Figure 4.7 offers unique evidence for a link between the hot and warm gas phases. The fact that the hot gas is cooling an order of magnitude faster in the filaments

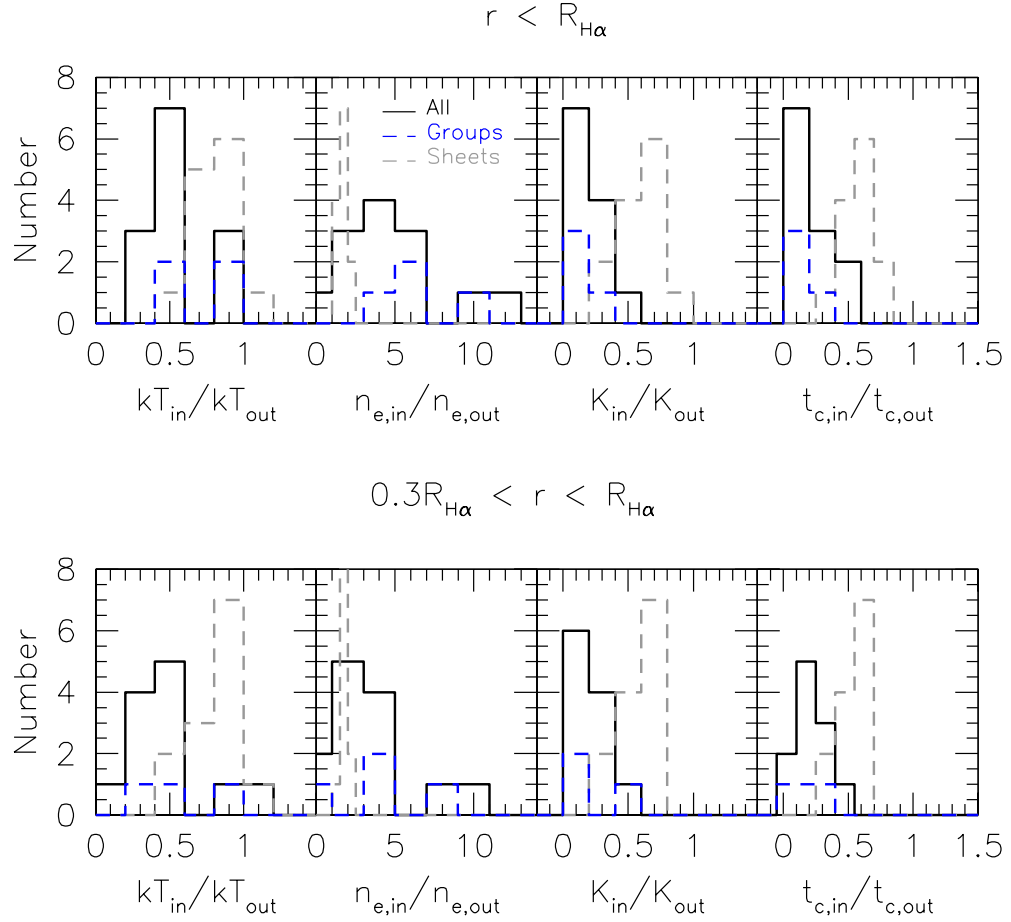


Figure 4.7 Upper panels: Distribution of temperature, electron density, entropy, and cooling time ratios in and out of the $H\alpha$ filaments. The solid black and dashed grey lines bracket the extreme cases of the filament geometry: solid black lines are the thin-filament case, which is modeled with a two-temperature plasma, while the grey dashed lines are the case of single-temperature sheets of gas seen edge-on. The blue, dashed lines show the contribution to the total histogram from galaxy groups. The in-filament gas shares similar properties with the cool core, namely that the X-ray gas has a cooling time of $\sim 10\%$ that of the surrounding ICM. There appears to be no difference in the properties of the filaments in groups and clusters. Lower panels: Similar to the above panels, but now considering only the outer 70% of the filaments in radius, in order to remove the contribution from the central, circularly symmetric, region.

provides a direct connection between the X-ray cooling flow and the H α filaments. Coupled with the correlation between the cooling rate and H α flux contained in filaments, the evidence for a link between the H α filaments and the X-ray cooling flow is further strengthened. The fact that we see no obvious differences between the properties of the filaments in groups and clusters suggests that the formation mechanisms for these filaments are the same. We discussed formation scenarios in depth in §3, but the addition of the lower mass systems now provide new insights in the discussion (next section).

4.4 Discussion

4.4.1 Groups vs Clusters: Differences and Similarities

Despite the smooth transition in mass and temperature from groups to clusters, the former are not simply scaled down versions of the latter. We summarize the most relevant differences between the two below.

- Feedback processes such as radio jets, starburst-driven winds, and merging with other bound systems will dominate in the group environment, while they play second fiddle to gravitational processes in the cluster environment. At $M \lesssim 10^{14} M_{\odot}$ the total radio heating energy of the BCG AGN (assuming $\epsilon = 0.1$; Sun 2009) becomes larger than the total potential or thermal energy of the ICM.
- While clusters form at late cosmological times ($z \lesssim 1$), groups have been forming over almost the entire age of the universe ($z \lesssim 10$; Fakhouri & Ma 2010). Since age roughly correlates with several X-ray observables (entropy, gas fraction) one would expect groups to have a much broader range of properties due

to their substantial spread in ages.

- In galaxy clusters, the ratio of the total mass in gas to dark matter is roughly 1:10, with a negligible contribution from light in stars using standard mass-to-light ratios. However, in galaxy groups, the stellar mass fraction is an order of magnitude higher, leading to significantly lower mass to light ratios (Giodini et al. 2009). Additionally, the gas fraction decreases as a function of total mass, such that groups can have stellar to dark matter ratios of roughly 1:10, with a negligible contribution from the ICM. Clearly this limits the influence that the ICM can have on the rest of the system.

Remarkably, although there are such vast differences between clusters and groups, we find very little dependence of $H\alpha$ emission on the global mass or temperature of the group/cluster. The fact that we see similar cooling rates and optical line flux in systems with orders of magnitude less gas implies that groups are more efficient in their cooling. In order to pursue this notion, we consider the cooling properties of the group/cluster as a function of the system mass (M_{2500}). In Figure 4.8 we first show the X-ray mass deposition rate, dM/dt , as a function of the group/cluster mass, M_{2500} . In order to improve the mass coverage, we have added 6 additional groups from the Sun et al. (2009) sample – these systems do not have $H\alpha$ imaging. We observe a steady increase of the cooling rate as a function of total mass, which is not surprising since there is more gas available for cooling. In order to remove this dependence on system mass, we next consider the amount of gas cooling out of the X-ray, per solar mass of material in the group/cluster (upper right panel of Figure 4.8). We see no observable trend between these two quantities. However, we do detect what looks like an upper limit to the cooling rate per unit mass, such that the maximum cooling is $\sim 0.02\%$ of the cluster mass per Gyr.

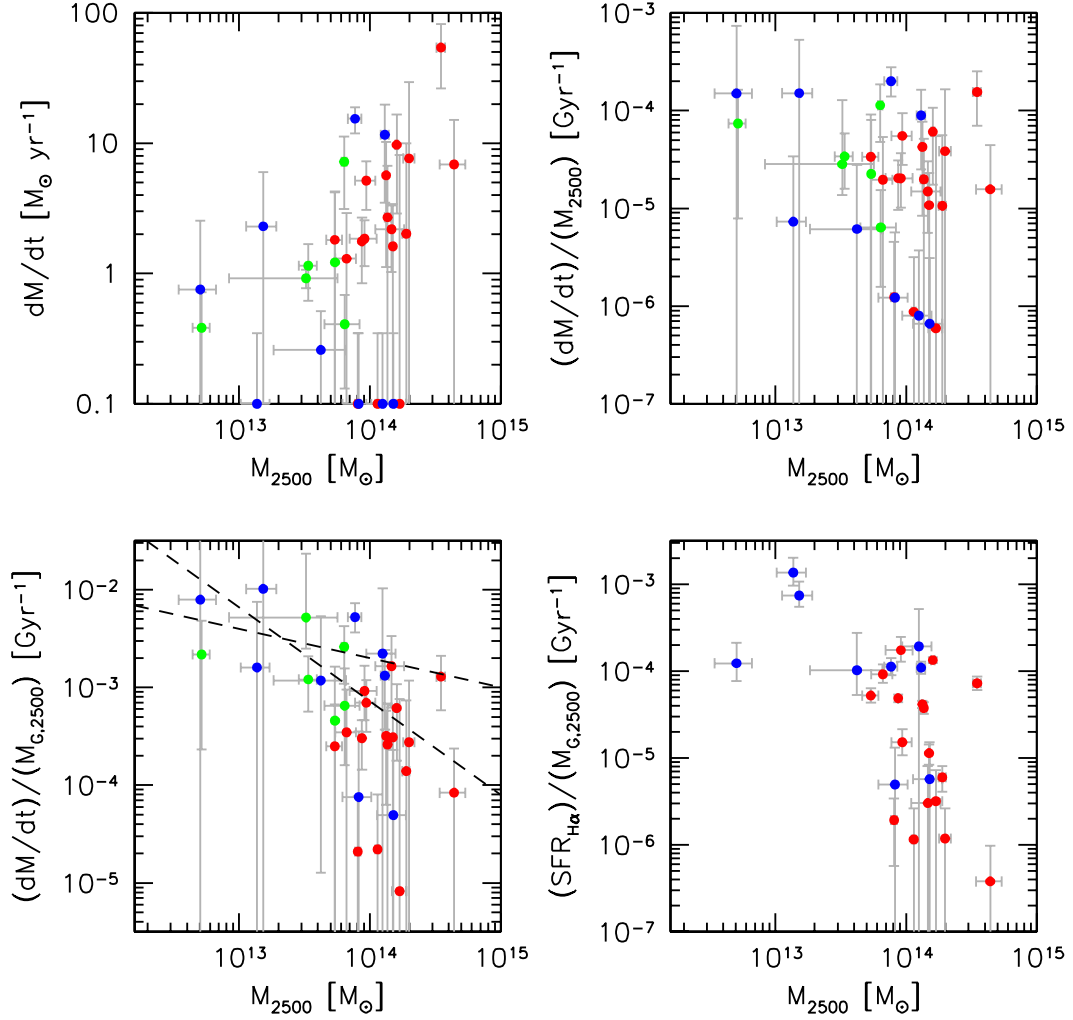


Figure 4.8 Upper left: X-ray cooling rate (dM/dt) as a function of M_{2500} , the mass enclosed within r_{2500} . Red and blue points refer to the cluster and group samples, respectively. Green points are six new groups taken from the Sun et al. (2009) sample in order to better sample the X-ray properties of the groups. Upper right: X-ray cooling rate per unit total mass as a function of M_{2500} . We note an apparent upper limit on this scaled cooling rate at $\sim 2 \times 10^{-4} \text{ Gyr}^{-1}$. Lower left: ICM cooling efficiency (cool rate per unit gas mass) as a function of M_{2500} . The dashed lines reflect the expected slopes for Bremsstrahlung (-0.3) and line cooling (-0.96). The zeropoints for these lines were adjusted to best fit the data. The fact that the data matches the general predicted trend suggests that the effect of feedback must either be negligible or scale with total mass, otherwise the trend would be altered. Lower right: $H\alpha$ -determined star formation rate per unit gas mass versus M_{2500} . Similar trends are noted here since $L_{H\alpha}$ is an excellent proxy for dM/dt (§3).

If, instead, we consider the *ICM cooling efficiency*, defined as the amount of gas cooling out of the X-ray per solar mass of *gas* in the group/cluster, we see a correlation (Pearson R=0.71). We can understand this correlation by considering the following: (1) The presence of cool cores is only weakly dependent on mass (Figure 4.3); (2) The total amount of gas is strongly dependent on mass. Combining these two points naturally leads to a correlation between the ICM cooling efficiency and the system mass. Similarly, we can show the same trend using the H α -derived star formation rate (directly proportional to L $_{H\alpha}$), instead of the X-ray cooling rate, since these two quantities are strongly correlated. As we discussed in §4.2, this sample is biased against massive, non-cool core clusters. We point out that the correction of this bias would introduce additional high-mass, low effective cooling rate points to Figure 4.8. As with Figure 4.3, this correction would act to strengthen the observed correlation. This correlation suggests that groups are more efficient at cooling than clusters, despite the fact that feedback processes dominate in this region.

To better understand this trend, we can approximate the expected relationship of the ICM cooling efficiency with total mass:

$$\left(\frac{dM}{dt} \frac{1}{M_G}\right) \sim \left(\frac{M_G}{t_{cool}} \frac{1}{M_G}\right) \sim \frac{1}{t_{cool}} \sim \left(\frac{kT}{n\Lambda}\right)^{-1} \propto \frac{\Lambda}{kT} \quad (4.1)$$

$$\Lambda \propto \left\{ \begin{array}{ll} T^{1/2} & (T > 4 \times 10^7 \text{ K, Bremsstrahlung}) \\ T^{-0.6} & (T < 4 \times 10^7 \text{ K, Line cooling}) \end{array} \right\} \quad (4.2)$$

Equation 1 makes the assumption that the local ICM density is roughly independent of the temperature, which we have confirmed for the groups/clusters in our sample. If we couple equations 1 and 2 with the relation between M and T found by Sun (2009, ; $M \propto T^{1.7}$), we find the dependence of the ICM cooling efficiency on mass matches well with the observations (see Figure 4.8). While this derivation

is overly simplistic, the confirmation with observation is reassuring. A major issue with such a simple derivation is that it ignores the role of feedback. In low-mass systems, one would expect the relative energy contribution from the AGN to increase substantially, yielding *less* efficient cooling. The fact that we observe the opposite suggests two possible scenarios for cool core clusters: i) AGN feedback plays a negligible role in countering ICM cooling, or ii) AGN feedback scales with environment. The former explanation is in opposition to a rich literature on the subject, both theoretical (e.g., Brighenti & Mathews 2003; Cattaneo & Teyssier 2007; Croton et al. 2006; McCarthy et al. 2010) and observational (e.g., Birzan et al. 2004; Donahue et al. 2006; Rafferty et al. 2008; Sun 2009), which offers significant evidence for AGN feedback playing a dominant role in the heating of galaxy group/cluster cores. The second explanation, that AGN feedback scales with environment, is more plausible. This scenario was recently investigated by Sun (2009), who found that, in cool core groups and clusters, the radio luminosity of the central AGN scales with the cooling luminosity. Sun found that cool cores in groups have consistently lower 1.4 GHz luminosity AGN than in clusters and suggested that the lower-pressure intragroup medium may not be able to sustain the radio-loud AGN seen in the cores of massive clusters. We elaborate on this idea in Figure 4.9.

Motivated by Figure 1 from Sun (2009), Figure 4.9 shows the 1.4 GHz luminosity ($L_{1.4GHz}$) as a function of the soft X-ray luminosity ($L_{0.5-2keV}$) inside of the cooling radius ($L_{0.5-2keV}$). We show in light grey points the distribution of groups and clusters from Sun (2009), while the red ellipses show the loci of these distributions. Sun identified two classes of system: coronae, which show no correlation between the cool X-ray and radio luminosities, and luminous cool cores, which have cool X-ray luminosity correlated with radio luminosity. We show in Figure 4.9 our proposed, simplified evolution of these systems. Luminous cool cores are experiencing

feedback-regulated cooling, such that both the AGN and cool core are able to grow slowly over timescales on the order of Gyr, based on measured cooling times in the central 100kpc. However, once the radio luminosity of the AGN reaches a certain threshold, it has enough energy to equal the PdV work required to evacuate the cool gas from the central 10kpc – this threshold radio luminosity is depicted by a dotted horizontal line for three different mass regimes. Thus, systems experiencing sufficiently strong radio-mode feedback have disrupted cool cores where the radio and X-ray luminosities are decoupled, yielding a corona-class object. Given the relatively few objects occupying the space between corona and cool core systems, the disruption of the cool cores must happen relatively quickly (\ll Gyr). With no cooling flow to fuel the central AGN, the radio luminosity will eventually drop until cooling is allowed again. Assuming the cool core is fully disrupted, it should take a few Gyr for gas which was originally at the cooling radius to form a new cool core. At this point, the central black hole becomes active once more and the feedback loop is re-established.

In Figure 4.9 there are three systems with radio luminosities sufficiently higher than the threshold for their mass – Hydra A, Abell 2052, and Abell 4059. These systems are all known to be experiencing higher-than-normal radio-mode feedback and have severely disrupted cool cores (e.g., Blanton et al. 2009; Reynolds et al. 2008; Wise et al. 2007). These systems all lie slightly off of the locus of points for luminous cool cores, suggesting that they may be in the midst of evolving from cool core to corona class via a disruption of the cool core.

In summary, Figures. 4.8–4.9 tell an interesting story about the cool cores of groups and clusters. The evidence suggests that groups are more efficiently converting the hot ICM into cool gas, as we detect $H\alpha$ filaments and cool cores with similar luminosity in systems with orders of magnitude difference in gas mass. It is unsur-

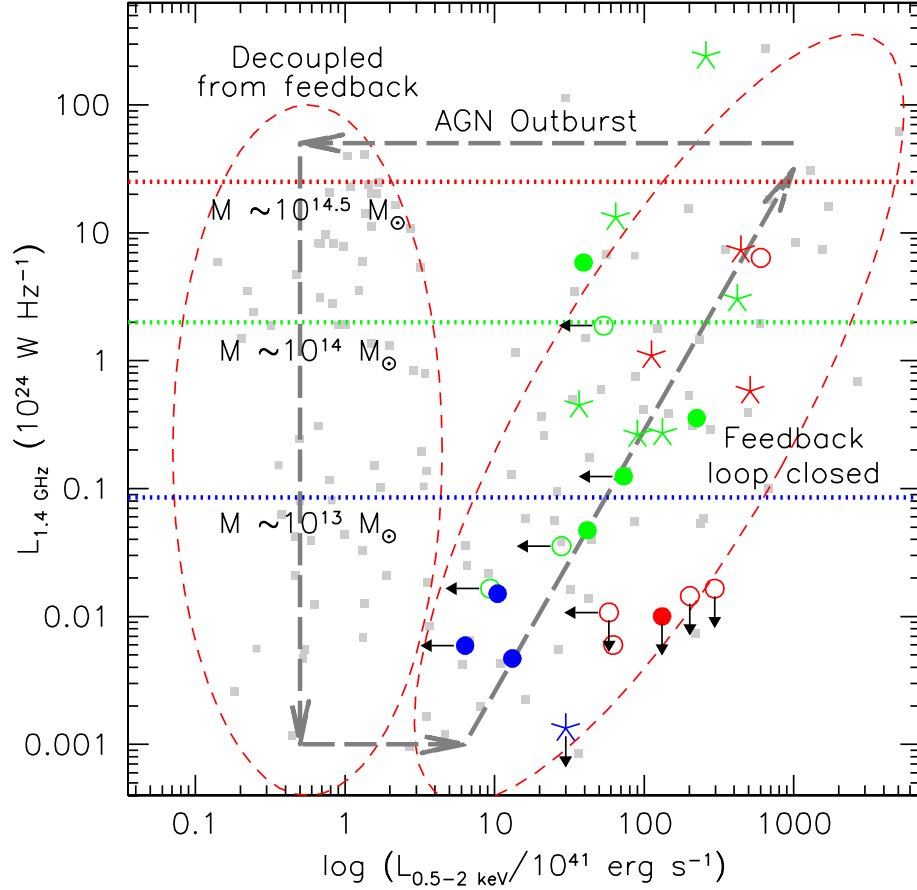


Figure 4.9 1.4 GHz radio luminosity versus integrated soft X-ray luminosity within the cooling radius. Color refers to the system mass, with blue, green and red referring to systems with $M_{2500} \sim 10^{13} M_{\odot}$, $10^{14} M_{\odot}$, and $10^{14.5} M_{\odot}$, respectively. Stars, closed circles and open circles are systems with filamentary, nuclear or no $H\alpha$ emission. Grey points are groups and clusters from Sun (2009) and the red ellipses describe the two loci identified by Sun. The grey arrows show the proposed evolution of systems from cool, feedback-regulated cores (right ellipse) to X-ray faint corona (left ellipse). If the radio luminosity exceeds a certain threshold, depicted by horizontal dotted lines, the amount of feedback exceeds the required pdV work needed to disrupt the cool core. This simple picture seems to have some merit, as the three clusters in our sample with extremely disrupted cores (Hydra A, Abell 2052, Abell 4059) all have radio luminosities exceeding the allowable threshold for their mass and are significantly offset to the left of the cool core locus. This plot provides an explanation for the fact that groups with cool cores tend to have low-luminosity AGN when compared to their high-mass counterparts.

prising that groups are cooling more efficiently, since the majority of the intragroup gas is already at low temperature. However, the fact that this cooling is allowed to proceed as expected suggests that AGN feedback, which we assume regulates the cooling process, scales with system mass as well. We confirm the findings by Sun (2009) that this is indeed the case, with cool cores in groups harboring radio-quiet AGN, while cool cores in massive clusters tend to have radio-loud AGN. This scaling of feedback strength with environment is a result of cool cores in low mass systems being more easily disrupted than those in high-mass systems.

4.4.2 The Origin of $H\alpha$ Filaments in Groups and Clusters

As discussed in §3, we find strong evidence for a link between the cool core and the observed $H\alpha$ filaments. Summarized briefly, the main pieces of evidence in favor of this scenario are:

1. The soft X-ray and $H\alpha$ morphologies are correlated (Figure 4.1)
2. There is a correlation between the $H\alpha$ luminosity and the X-ray cooling rate (Figure 4.5)
3. $H\alpha$ filaments extend all the way to the X-ray cooling radius, but never beyond (Figure 4.6).
4. The ICM coincident with the $H\alpha$ filaments is cooling an order of magnitude faster than in the immediately surrounding regions (Figure 4.7).

We find that all of these trends, originally quoted in §3, are seen in groups as well. This argues strongly in favor of a common origin and suggests that the cooling process may be detached from the global properties of the system.

The link between the X-ray cooling properties and the optical emission suggests that the $H\alpha$ filaments trace the cooling flow. This is not to say that the $H\alpha$ emission is due to the cooling ICM recombining at 10^4 K, but rather that the morphology of the $H\alpha$ filaments is reminiscent of magnetohydrodynamic simulations of gas cooling. As the ICM cools, it may be experiencing thermal instability along magnetic field lines, causing it to collapse into thin, dense filaments resembling the observed $H\alpha$ morphology (e.g., Sharma et al. 2010). Once the cool filaments have been established, they require an ionization source to produce the high $H\alpha$ surface brightnesses which are observed. This heating may be due to a combination of photoionization by young stars, conduction with the hotter ICM and cosmic rays (see §3 for a more detailed discussion).

An alternative hypothesis is that of buoyant radio bubbles (e.g., Revaz et al. 2008; Reynolds et al. 2005). In this scenario, bubbles are blown in the dense ICM by the radio-loud AGN. Due to their buoyancy these bubbles will be transported to larger radius, possibly entraining cool gas along the way. This model produces thin, radial filaments of cool gas reminiscent of the $H\alpha$ filaments in many cluster cores. While radio-mode feedback is likely responsible for the optical emission in a few systems (e.g., Hydra A, Abell 2052), it is hard to imagine how multiple filaments with similar surface brightnesses at a variety of orientations can be produced by this process.

4.5 Summary and Future Prospects

This study extends the work presented in §3 to include galaxy groups in order to determine the role of environment in the formation of $H\alpha$ filaments in cool cores. In summary, we find:

- The morphology and detection frequency of H α filaments in groups is similar to those seen in clusters.
- There is no obvious dependence between H α emission and the temperature of the system. There is a weak correlation between the H α emission and the mass of the system, as measured at r_{2500} . This weak correlation may be strengthened by the inclusion of high-mass, non-cooling clusters, which are underrepresented in our sample.
- There is a weak correlation between the presence of H α filaments and the global ICM gas fraction (51% confidence level) and a strong correlation with global entropy (89% confidence level), such that H α filaments are more frequently detected in systems with low entropy and high gas fractions.
- There is a correlation between the presence of H α filaments and the properties of the cool core, namely the X-ray cooling rate (72% confidence level), the average temperature in the inner 100 kpc (55% confidence level) and the entropy at a radius of 50 kpc (84%). The correlations between the H α emission and the cooling rate and entropy in the cool core confirm previous results (Cavagnolo et al. 2008, §3 of this thesis) and favor the scenario where these thin filaments are the result of rapid, thermally-unstable cooling of the ICM (Sharma et al. 2010).
- The most extended H α filaments extend to the radius at which the hot ICM is cooling in ~ 3 Gyr, but not beyond. This suggests a natural timescale for the formation of filaments.
- ICM cooling is enhanced by roughly an order of magnitude in regions with H α filaments, compared to surrounding regions at the same radius.

- The cooling efficiency (cooling rate per unit gas mass) is higher in groups than in clusters, as is predicted by cooling in the absence of feedback. This is a manifestation of the weak dependence of cool cores with mass (second bullet) coupled with the strong dependence of gas content on mass. This correlation would be further improved by the inclusion of high-mass, non-cooling clusters, which are underrepresented in our our sample.
- We confirm Sun (2009) finding that AGN in cool core groups have much lower radio luminosity than those in clusters. We show that this could explain the amount of feedback scaling with environment, since cool cores in groups can only survive if the amount of radio-mode feedback is small. We observe three systems with radio luminosities higher than the amount needed to remove the cool core, all of which have very disrupted cool cores and deviate from the relationship found for groups/clusters with closed feedback loops.

Our findings suggest that cool cores, and the optical line-emitting nebulae commonly associated with them, can form in groups and clusters over a large range of mass and temperature, with very little dependence on either. However, considerably larger samples will be needed to quantify whether this correlation is weak or nonexistent. We confirm the results of §3, offering further support that the observed H α filaments in the cores of groups/clusters are intimately linked to the X-ray cooling in most systems. Without high-resolution UV imaging and optical spectroscopy, we are unable to constrain the ionization mechanism of these filaments. We plan on addressing these issues in upcoming chapters.

s

Chapter 5

Star Formation Efficiency in the Cool Cores of Galaxy Clusters

5.1 Introduction

The high densities and low temperatures of the intracluster medium (ICM) in the cores of some galaxy clusters suggests that massive amounts ($100\text{--}1000 M_{\odot} \text{ yr}^{-1}$) of cool gas should be deposited onto the central galaxy. The fact that this gas reservoir is not observed has been used as prime evidence for feedback-regulated cooling (see review by Fabian 1994). By invoking feedback, either by active galactic nuclei (AGN) (e.g., Conroy & Ostriker 2008; Guo & Oh 2008; Rafferty et al. 2008), mergers (e.g., Gómez et al. 2002; ZuHone et al. 2010), conduction (e.g., Fabian et al. 2002; Voigt & Fabian 2004), or some other mechanism, theoretical models can greatly reduce the efficiency of ICM cooling, producing a better match with what is observed in high resolution X-ray grating spectra of cool cores ($0\text{--}100 M_{\odot} \text{ yr}^{-1}$, Peterson et al. 2003). However, these modest cooling flows had remained unaccounted for at low temperatures until only recently.

The presence of warm, ionized gas in the form of H α emitting filaments has been observed in the cores of several cooling flow clusters to date (e.g., Crawford et al. 1999; Hatch et al. 2007; Heckman et al. 1989; Hu et al. 1985; Jaffe et al. 2005). More recently, we showed in §3 and §4 that this emission is intimately linked to the cooling ICM and may be the result of cooling instabilities. However, while it is possible that the warm gas may be a byproduct of ICM cooling, the source of ionization in this gas remains a mystery. A wide variety of ionization mechanisms are viable in the cores of clusters (see Crawford et al. 2005, for a review), the least exotic of which may be photoionization by massive, young stars.

The identification of star-forming regions in cool core clusters has a rich history in the literature. Early on, it was noted by several groups that brightest cluster galaxies (BCGs) in cool core clusters have higher star formation rates than non-cool core BCGs (Allen 1995; Cardiel et al. 1995; Johnstone et al. 1987; McNamara & O’Connell 1989; Romanishin 1987). These studies all found evidence for significant amounts of star formation in cool cores, but the measured star formation rates were orders of magnitudes smaller than the X-ray cooling rates (e.g., McNamara & O’Connell 1989). In recent history, two separate advances have brought these measurements closer together. First, as mentioned earlier in this section, the X-ray spectroscopically-determined cooling rates are roughly an order of magnitude lower than the classically-determined values based on the soft X-ray luminosity. Secondly, large surveys in the UV (e.g., Hicks et al. 2010; Rafferty et al. 2006), optical (e.g., Bildfell et al. 2008; Crawford et al. 1999; Edwards et al. 2007, §3 of this thesis), mid-IR (e.g., Egami et al. 2006; Hansen et al. 2000; O’Dea et al. 2008; Quillen et al. 2008, hereafter MIR), and sub-mm (e.g., Edge 2001; Salomé & Combes 2003) have allowed a much more detailed picture of star formation in BCGs. The typical star formation rates of $\sim 1\text{--}10 M_{\odot} \text{ yr}^{-1}$ (O’Dea et al. 2008) imply that gas

at temperatures of $\sim 10^{6-7}$ K is being continuously converted into stars with an efficiency on the order of $\sim 10\%$. The fact that most of these studies consider the *integrated* SF rates makes it difficult to determine the exact role of young stars in ionizing the extended warm gas observed at H α , since the two may not be spatially coincident or the measurements may be contaminated by the inclusion of a central AGN.

In order to understand both the role of star formation in ionizing the warm gas and the efficiency with which the cooling ICM is converted into stars, we have conducted a high spatial resolution far-UV survey of BCGs in cooling and non-cooling clusters. We describe the collection and analysis of the data from this survey in §5.2. In §5.3 we describe the results of this survey, while in §5.4 we discuss the implications of these results in the context of our previous work (§3 and §4). Finally, in §5.5 we summarize our findings and discuss any outstanding questions. Throughout this chapter, we assume the following cosmological values: $H_0 = 73$ km s $^{-1}$ Mpc $^{-1}$, $\Omega_{matter} = 0.27$, $\Omega_{vacuum} = 0.73$.

5.2 Data Collection and Analysis

To study the far-UV (FUV) emission in cluster cores, we selected 15 galaxy clusters from the larger samples described in §3 and §4, which have deep, high spatial resolution (FWHM $\sim 0.6''$) H α imaging from the Maryland-Magellan Tunable Filter (MMTF; Veilleux et al. 2010) on the Baade 6.5-m telescope at Las Campanas Observatory. Additionally, most of these systems have deep Chandra X-ray Observatory (CXO) spectroscopic imaging, as well as Two-Micron All Sky Survey (2MASS; Skrutskie et al. 2006) and NRAO VLA Sky Survey (NVSS; Condon et al. 1998) fluxes. This broad energy coverage provides an excellent complement to a FUV

survey, allowing for the source of emission to be carefully identified. A summary of these 15 clusters can be found in Table 5.1. For further information about the reduction and analysis of the $H\alpha$ and X-ray data, see §3.

FUV imaging was acquired using the Advanced Camera for Surveys Solar Blind Channel (ACS/SBC) on the Hubble Space Telescope (HST) in both the F140LP and F150LP bandpasses whenever possible, with a total exposure time of ~ 1200 s each (PID #11980, PI Veilleux). The pointings were chosen, based on the results of our MMTF survey, to include all of the $H\alpha$ emission in the field of view. Exposures with multiple filters are required to properly remove the known ACS/SBC red leak, which has a non-negligible contribution due to the fact that the underlying BCG is very luminous and red. Since the aforementioned filters are long-pass filters, they have nearly identical throughputs at longer wavelengths. Thus, by subtracting the F150LP exposure from the F140LP exposure we can effectively remove the red leak and consider only a relatively small range in wavelength, from 1400\AA – 1500\AA . Due to the small bandpass, it is possible for line emission to dominate the observed flux – we investigate this possibility in §5.4. We have carried out this subtraction for 13/15 of the BCGs in our sample which have both F140LP and F150LP imaging. For Abell 1795 and Abell 2597, we are unable to remove the red leak contribution due to the lack of paired exposures, but we point out that, conveniently, these two systems have the brightest FUV flux in our sample and, thus, are largely unaffected by the inclusion of a small amount of non-FUV flux. Following the red-leak subtraction, we also bin the images 8×8 and smooth the images with a 1.5 pixel smoothing radius, yielding matching spatial resolution at FUV and $H\alpha$. This process is also necessary in order to increase the signal-to-noise of the FUV image, allowing us to identify interesting morphological features. The final pixel scale for both the $H\alpha$ and FUV images is $0.2''/\text{pixel}$.

Table 5.1 Sample of 15 cooling flow clusters with MMTF H α and HST FUV imaging

Name (1)	RA (2)	Dec (3)	z (4)	E(B-V) (5)	M (6)	F _{1.4} (7)	Proposal No. (8)
Abell 0970 ^a	10h17m25.7s	-10d41m20.3s	0.0587	0.055	-	< 2.5	11980
Abell 1644	12h57m11.6s	-17d24m33.9s	0.0475	0.069	3.2	98.4	11980
Abell 1650	12h58m41.5s	-01d45m41.1s	0.0846	0.017	0.0	< 2.5	11980
Abell 1795	13h48m52.5s	+26d35m33.9s	0.0625	0.013	7.8	924.5	11980, 11681
Abell 1837	14h01m36.4s	-11d07m43.2s	0.0691	0.058	0.0	4.8	11980
Abell 1991	14h54m31.5s	+18d38m32.4s	0.0587	0.025	14.6	39.0	11980
Abell 2029	15h10m56.1s	+05d44m41.8s	0.0773	0.040	3.4	527.8	11980
Abell 2052	15h16m44.5s	+07d01m18.2s	0.0345	0.037	2.6	5499.3	11980
Abell 2142	15h58m20.0s	+27d14m00.4s	0.0904	0.044	1.2	< 2.5	11980
Abell 2151	16h04m35.8s	+17d43m17.8s	0.0352	0.043	8.4	2.4	11980
Abell 2580 ^a	23h21m26.3s	-23d12m27.8s	0.0890	0.024	-	46.4	11980
Abell 2597	23h25m19.7s	-12d07m27.1s	0.0830	0.030	9.5	1874.6	11131
Abell 4059	23h57m00.7s	-34d45m32.7s	0.0475	0.015	0.7	1284.7	11980
Ophiuchus	17h12m27.7s	-23d22m10.4s	0.0285	0.588	0.0	28.8	11980
WBL 360-03 ^a	11h49m35.4s	-03d29m17.0s	0.0274	0.028	-	< 2.5	11980

(1): Cluster name, (2-4): NED RA, Dec, redshift of BCG (<http://nedwww.ipac.caltech.edu>), (5): Reddening due to Galactic extinction from Schlegel et al. (1998), (6): Spectroscopically-determined X-ray cooling rates ($M_{\odot} \text{ yr}^{-1}$) from §3, (7): 1.4 GHz radio flux (mJy) from NVSS (<http://www.cv.nrao.edu/nvss/>) (8) HST proposal number for FUV data. Proposal PIs are W. Jaffe (#11131), W. Sparks (#11681), S. Veilleux (#11980).
^a: No available Chandra data.

All FUV and $H\alpha$ fluxes were corrected for Galactic extinction following Cardelli et al. (1989) using reddening estimates from Schlegel et al. (1998).

5.3 Results

In Figure 5.1, we show the stellar continuum, $H\alpha$ and FUV images for each of the 15 BCGs in our sample. At a glance there does not appear to be consistent agreement between the $H\alpha$ and FUV morphologies. We observe systems having $H\alpha$ filaments without accompanying FUV emission (Abell 1991, Abell 2052), systems with complex FUV emission without accompanying $H\alpha$ (Abell 1837, Abell 2029), and systems with coincident $H\alpha$ and FUV extended emission (Abell 1644, Abell 1795). Thus, it is obvious that a single explanation (e.g., star formation) is unable to account for the variety of FUV and $H\alpha$ emission that we observe.

As we did with the $H\alpha$ emission in §3, the FUV morphology can be classified as either nuclear or extended. We find, in the FUV, 7/15 systems have extended emission, 5/15 have nuclear emission, while 3/15 have no emission at all. In order to quantitatively examine both the nuclear and extended emission, we extract FUV and $H\alpha$ fluxes in several regions, as shown in Figure 5.1.

In Figure 5.2a, we show the correlation between the FUV and $H\alpha$ luminosity for the regions identified in Figure 5.1. We find a significant amount of FUV emission in all 5 of the systems for which we do not detect any $H\alpha$ emission. Additionally, we see that at least 3 systems are consistent with being shock-heated (Dopita & Sutherland 1996) – a point we will return to later in this section.

As discussed by Hicks et al. (2010), a significant fraction of the FUV emission may be due to old stellar populations (e.g., horizontal branch stars) in the BCG. To proceed, we must isolate the FUV excess due to young, star-forming regions. In

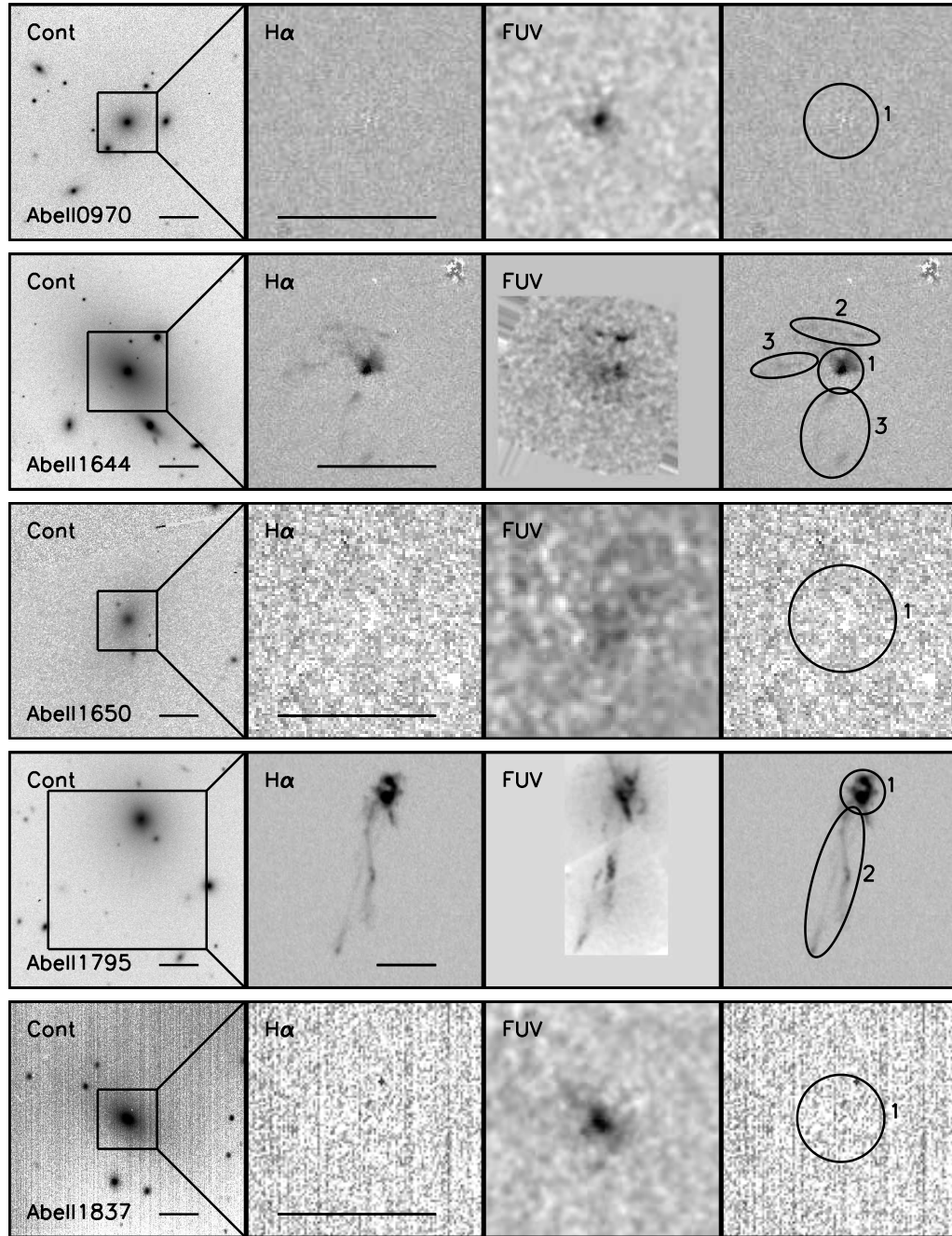


Figure 5.1 Optical and FUV data for the 15 clusters in our sample. From left to right the panels are: 1) MMTF red continuum image, 2) MMTF continuum-subtracted $H\alpha$ image, 3) ACS/SBC FUV redleak-subtracted image (F150LP-F140LP), 4) $H\alpha$ image with extraction regions defined. The horizontal scale bar in the left two panels represents 20 kpc. The $H\alpha$ and FUV images are zoomed in relative to the red continuum image. The square region in the red continuum panels represents the field of view for the zoomed-in panels. The grayscale in all images is arbitrarily chosen in order to enhance any morphological features.

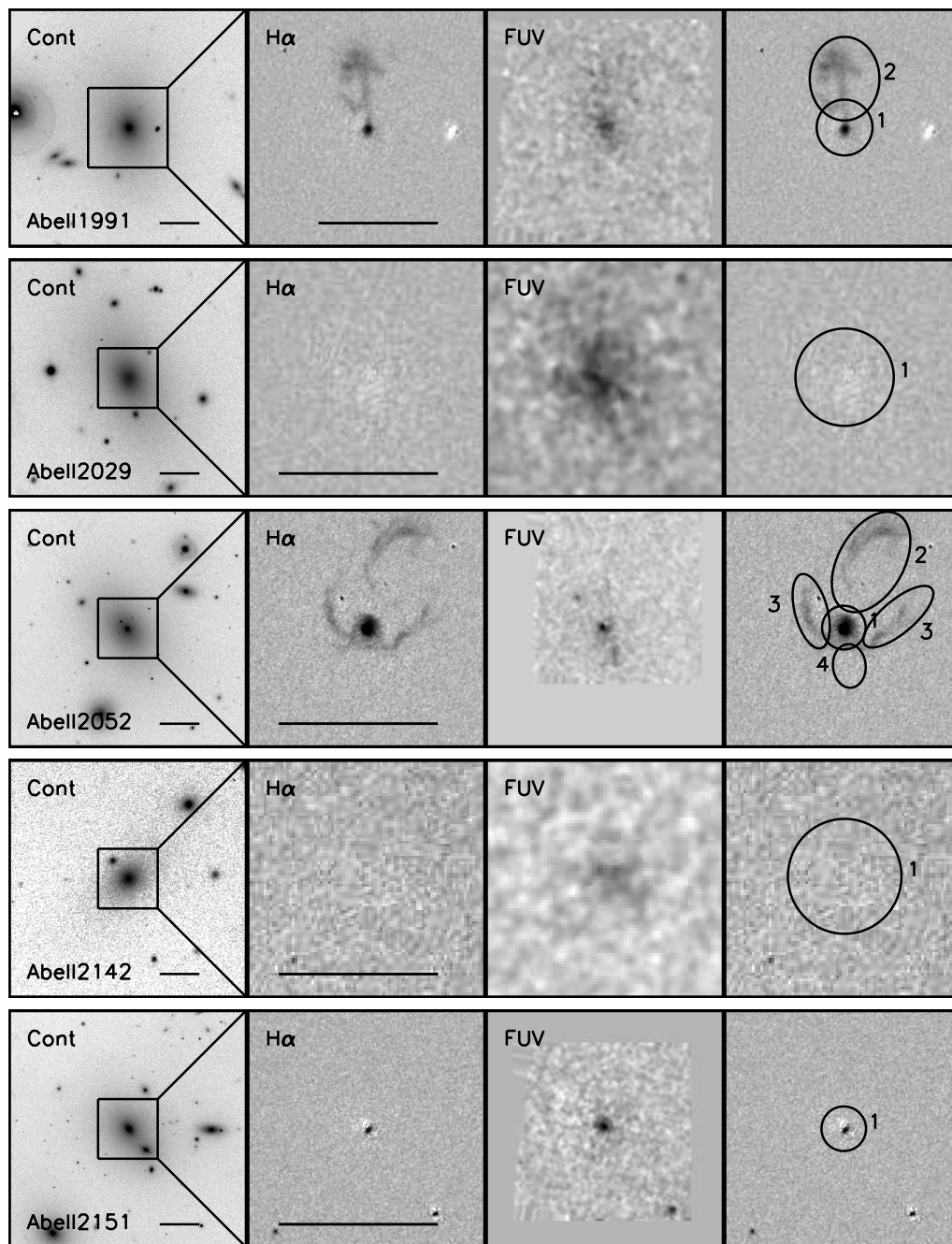


Figure 5.1 Continued.

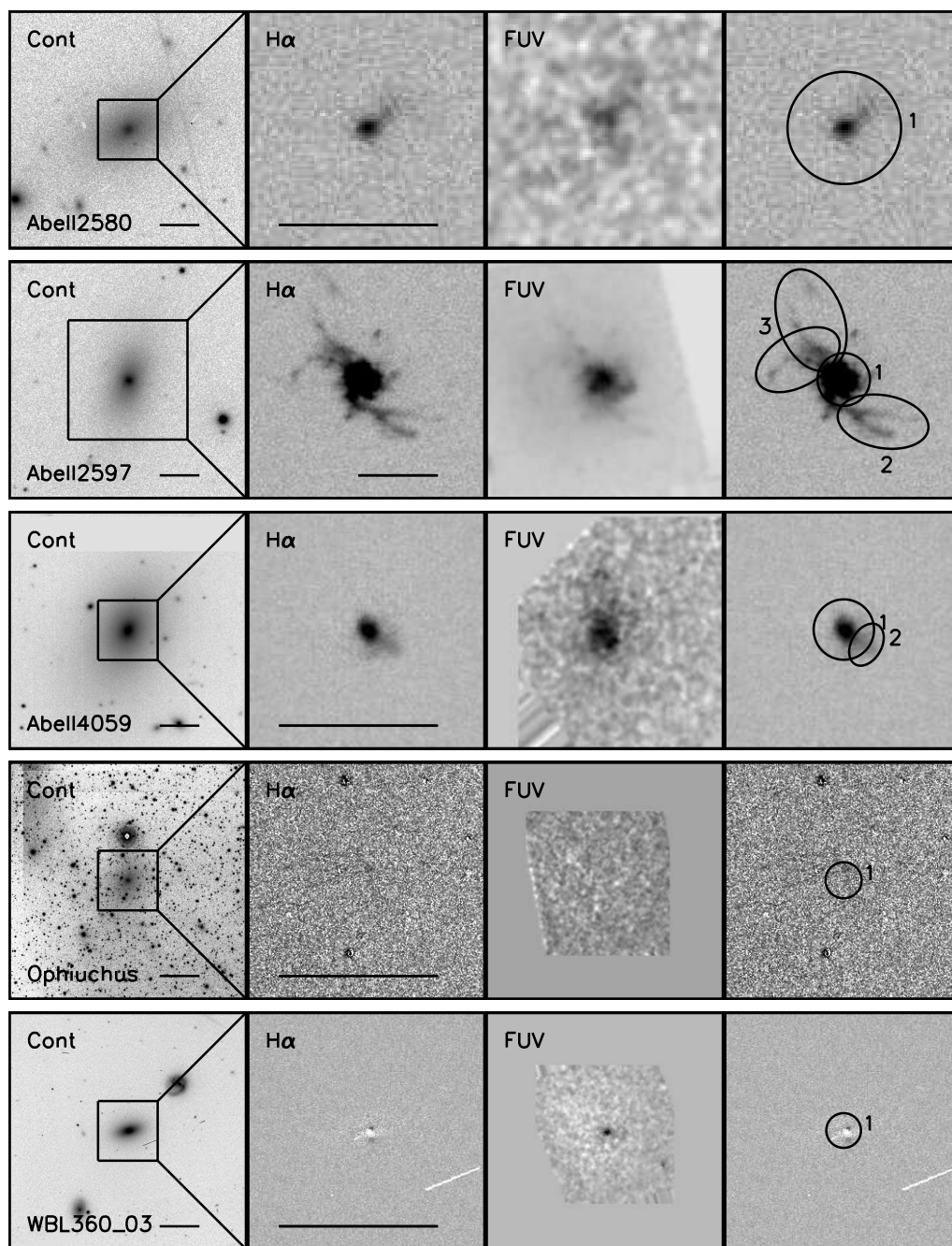


Figure 5.1 Continued.

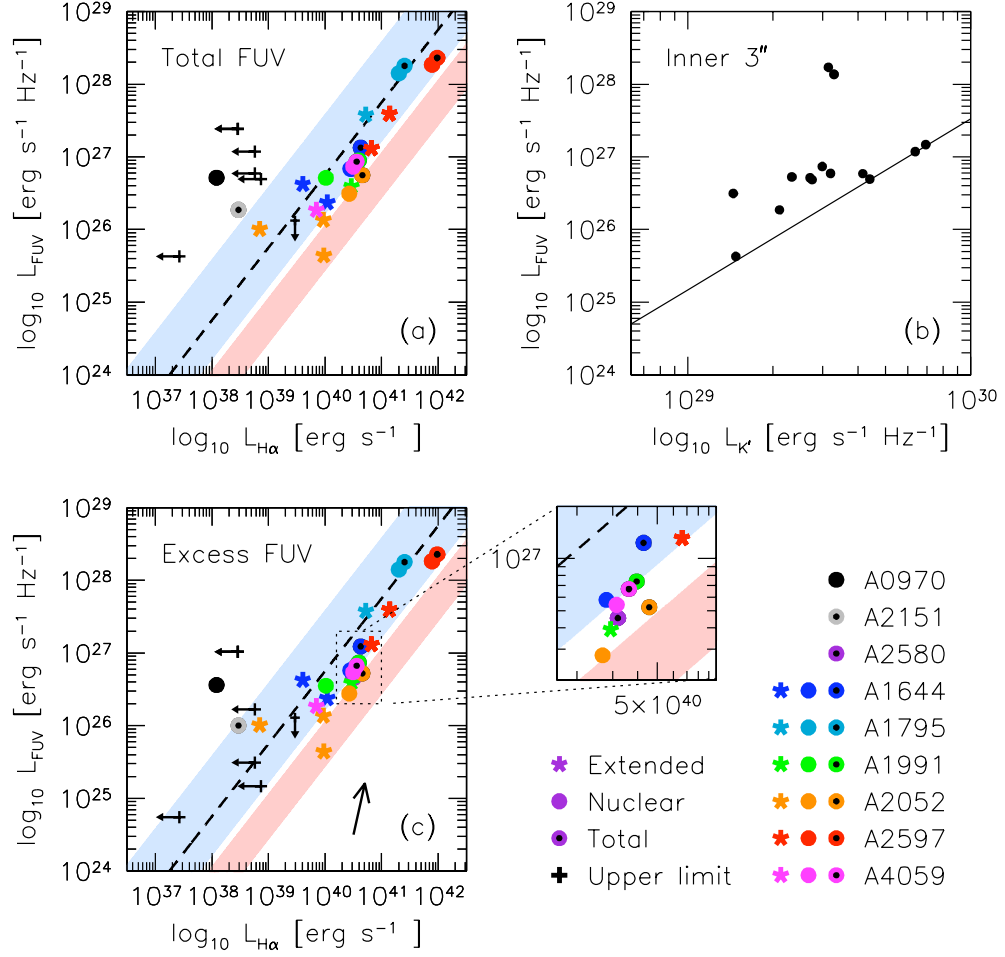


Figure 5.2 (a) FUV versus $\text{H}\alpha$ luminosity for 15 BCGs in our sample. For systems with extended FUV or $\text{H}\alpha$ emission, we separate the emission into extended, nuclear (inner 3'') and entire systems (see Figure 5.1). The dashed line represents the relation between $\text{H}\alpha$ and FUV luminosity for SF regions, as defined by Kennicutt (1998), the shaded blue region represents the expected FUV/ $\text{H}\alpha$ ratio for continuous SF covering the full range of IMFs and metallicities from Starburst99 (Leitherer et al. 1999), while the shaded red region defines the expected FUV/ $\text{H}\alpha$ ratio for fast shocks (Dopita & Sutherland 1996). The legend in the lower right describes the different point type/colors. (b) FUV versus K' -band luminosity in the central 3'' of the BCG. The solid line represents our estimate of the contribution to the FUV luminosity from old, horizontal-branch stars. (c) Similar to panel (a), but with the contribution from old stars removed from the nuclear and total regions. The correlation between FUV and $\text{H}\alpha$ luminosity is much more significant, suggesting that the majority of the observed $\text{H}\alpha$ emission may be due to photoionization by young stars. The extended and nuclear emission in Abell 2052 and Abell 2580, as well as the extended emission in Abell 1991 appears to be consistent with heating by shocks, while the remaining systems are likely star-forming. The arrow in the lower right corner represents the magnitude of the intrinsic extinction correction for $E(B-V)=0.2$.

order to remove the contribution from old stars, we consider the inner $3''$ and plot the K-band (from 2MASS; Skrutskie et al. 2006) versus the FUV luminosity (Figure 5.2b). Hicks et al. (2010) show that the FUV luminosity from old stars is highly concentrated in the central region, thus removing this contribution in the inner region will act as a suitable first-order correction. In order to calibrate this correction for our sample, which lacks a control sample of confirmed non-star-forming galaxies, we opt to fit a line which is chosen to pass through the four points with the lowest $L_{FUV}/L_{K'}$ ratio. We make the assumption that these four galaxies with the lowest $L_{FUV}/L_{K'}$ ratio are non-star-forming, which is supported by non-detections at $H\alpha$. The equation for this relation is: $\log_{10}(L_{FUV,3''}) = 2.35\log_{10}(L_{K',3''}) - 42.98$. The fact that four points with non-detections at $H\alpha$ lie neatly along the same line suggests that this correction is meaningful.

Figure 5.2c shows the FUV excess due to young stars versus the $H\alpha$ luminosity for the total, nuclear and extended regions in our complete sample of BCGs. With the contribution from old stellar populations removed, we find a tight correlation between L_{FUV} and $L_{H\alpha}$ over four orders of magnitude. The majority of systems in our sample are consistent with the continuous star formation scenario (Kennicutt 1998; Leitherer et al. 1999), suggesting that much of the warm gas found in cluster cores may be photoionized by young stars. Two systems, Abell 0970 and Abell 2029 have anomalously high FUV/ $H\alpha$ ratios, suggesting that star formation may be proceeding in bursts. As a starburst ages, the UV/ $H\alpha$ ratio will climb quickly due to the massive stars dying first. This means that, by 10 Myr after the burst, the UV/ $H\alpha$ ratio can already be an order of magnitude higher than the expected value for continuous star formation (see §3 for further discussion). We find that the filaments in Abell 1991 and Abell 2052 are consistent with being heated by fast shocks, along with the nuclei of Abell 2052 and Abell 2580. In the case of Abell 2052,

there exist high quality radio and X-ray maps which show that the observed $H\alpha$ emission is coincident with the inner edge of a radio-blow bubble. In Abell 1991, the $H\alpha$ morphology is reminiscent of a bow shock, and is spatially coincident with a soft X-ray blob which is offset from the cluster core. Much of the FUV and $H\alpha$ data is clustered between the regions depicting continuous star formation and shock heating, as shown in the zoomed-in portion of Figure 5.2. These regions may indeed be heated by a combination of processes, or they may simply be reddened due to intrinsic extinction. Based on their FUV/ $H\alpha$ ratios, $H\alpha$ morphology, disrupted X-ray morphology, and high radio luminosity, we propose that the optical emission in Abell 1991, Abell 2052, and Abell 2580 is the product of shock heating, while the remaining 12 systems are experiencing continuous or burst-like star formation. We will return to this classification in the discussion. The SF rates that we measure in the systems with nuclear emission only range from 0.01–0.1 $M_{\odot} \text{ yr}^{-1}$, which are typical of normal red-sequence ellipticals (Kennicutt 1998). For the systems with extended emission, excluding those that are obviously shock-heated, the measured star formation rates range from 0.1–5 $M_{\odot} \text{ yr}^{-1}$ which is similar to the rates of 0.008–3.6 $M_{\odot} \text{ yr}^{-1}$ observed in “blue early-type galaxies” (Wei et al. 2010).

In Figure 5.3 we present the distribution of the FUV/ $H\alpha$ ratio in various regions for the 10 systems with detections ($>1\sigma$) at either $H\alpha$ or FUV. In the innermost region ($r < 0.8''$), the warm gas appears to be shock-heated in 60% of systems – these shocked nuclei may be associated with AGN-driven outflows. Due to the small radial extent of this bin, the 2MASS data is of insufficient spatial resolution to remove any contribution from old stars. Thus, these FUV/ $H\alpha$ ratios are upper limits. Of the remaining 4 systems, 2 are consistent with continuous star formation or a young starburst, while the remaining two are consistent with an aged starburst. At larger radius ($0.8'' < r < 3.0''$) the FUV/ $H\alpha$ ratio is slightly larger, with the

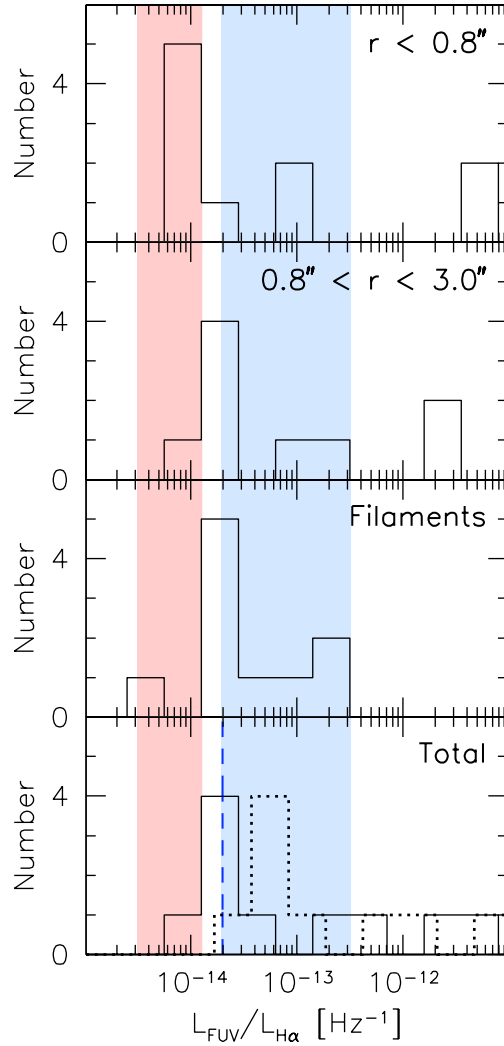


Figure 5.3 Distribution of the FUV to $H\alpha$ luminosity ratios for the 10 clusters in our sample with high S/N detections in either the FUV or $H\alpha$. Each panel considers a different region, from top to bottom: the nucleus, the central $3''$, excluding the nucleus, the filaments, and the entire system. The red vertical band represents the region consistent with shocks (Dopita & Sutherland 1996), while the blue band represents the region consistent with continuous star formation (Leitherer et al. 1999). In the nucleus, the majority of the observed $H\alpha$ emission is consistent with having been shock-heated, while in the outer regions, including filaments, the FUV/ $H\alpha$ ratio lies between the two highlighted regions. In the bottom panel, the dotted histogram shows how the distribution would be altered if we corrected the fluxes for an intrinsic extinction of $E(B-V)=0.2$ (dust screen model), while the blue dashed line represents the expected value for O8V stars (symbolic of a top-heavy IMF).

distribution peaking in between the regions describing shocks and star formation (see inset of Figure 5.4). These data have had the contribution from old stellar populations removed, as described earlier in this section. The FUV/H α ratio at this radius is similar to what we observe in the filaments, as is seen in the third panel of Figure 5.3. The fact that the distribution of FUV/H α peaks between the values for shocks and star formation supports a number of scenarios, including a mixture of the two processes, dusty star formation and star formation with an IMF skewed towards high-mass stars (see right-most panel of Figure 5.3). We will investigate these scenarios in §5.4.

In §3 and §4, we showed that the H α emission observed in the cool cores of galaxy clusters is intimately linked to the cooling ICM. In general, the thin, extended filaments observed in many of these clusters are found in regions where the ICM is cooling most rapidly, suggesting that this warm gas may be a byproduct of the ongoing cooling. If this is the case, it is relevant to ask what fraction of the cooling ICM is turning into stars. We address this question in Figure 5.4 by comparing the star formation rate with the X-ray cooling rate (dM/dt) for 32 galaxy clusters. In order to compute the star formation rate, we use the prescriptions in Kennicutt (1998). For the systems observed with HST, we use the average of the FUV- and H α -determined star formation rates (filled blue circles). For an additional 10 clusters from §3 and §4 we make use of archival GALEX data for 5 clusters (open blue circles) and assume that both the UV and H α emission trace star forming regions. These data have also had the contribution from old stellar populations removed, as described in §3. In the remaining 5 cases where there is no accompanying UV data, we assume that the H α emission is the result of photoionization by young stars, and convert the H α luminosity into a continuous star formation rate (green triangles). For the three shock-heated systems (red crosses) mentioned above, we determine

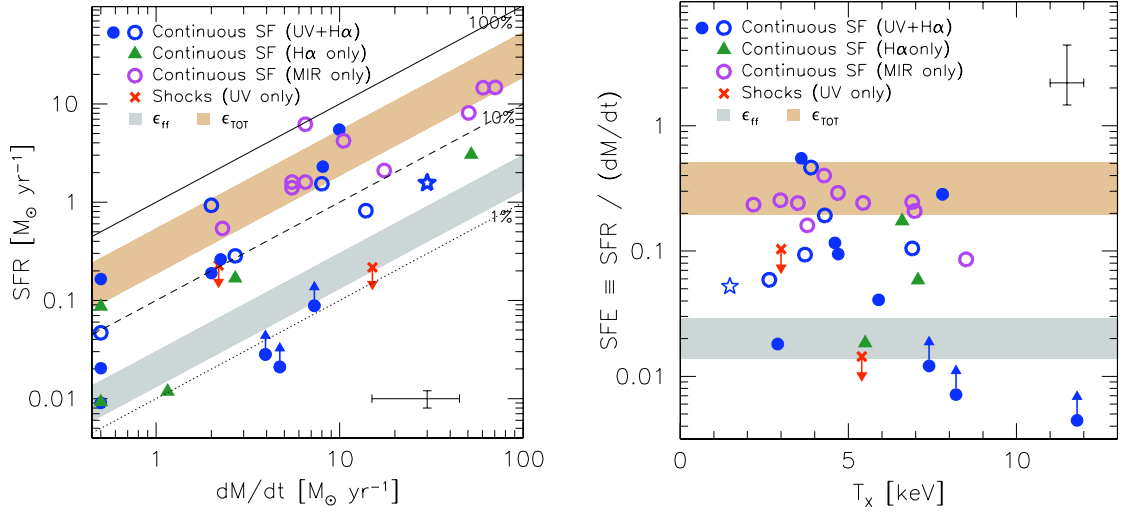


Figure 5.4 Left: SF rate (SFR) versus X-ray cooling rate (dM/dt) for 32 galaxy clusters. The filled blue circles (10) and red crosses (2) correspond to clusters identified as star-forming and shock-heated from Figure 5.2, respectively. One of the shock-heated systems, Abell 2580, does not have available data from the CXO archives. The open blue circles (5) refer to clusters with MMTF H α imaging and archival GALEX near-UV (NUV) data from §3. The green triangles (5) are clusters with deep H α imaging from §3 and §4 – we assume this emission is due to star formation. Star formation rates are computed from NUV, FUV, and H α luminosities based on the prescriptions in Kennicutt (1998). We also show data from O’Dea et al. (2008) as open purple circles (10), with SF rates based on mid-IR (MIR, $24\mu\text{m}$) *Spitzer* data and dM/dt computed in a similar fashion to us. The blue star represents the Perseus cluster (Conselice et al. 2001; Sanders et al. 2004). Diagonal lines refer to efficiencies of 1%, 10% and 100%, while the shaded regions refer to the typical SF efficiency in molecular clouds per free fall time (gray; Krumholz & McKee 2005) and over the lifetime of the cloud (tan; Kroupa 2001; Lada & Lada 2003). Typical errors (20% in SFR, 50% in dM/dt) are shown in the bottom right corner. Right: SF efficiency (SFR per dM/dt) as a function of cluster X-ray temperature from the ACCEPT sample of Cavagnolo et al. (2009). Typical errors are shown in the upper right corner. We note that the error in SF efficiency is dominated by our uncertainty in the X-ray cooling rate, dM/dt . The highest-temperature point is the Ophiuchus cluster, which lies close to the Galactic plane and, thus, suffers from heavy extinction. While we do correct for Galactic extinction, the large column density will amplify any uncertainty in the measurement of N_H or in the extinction curves applied.

the SF rate based on the FUV luminosity alone – this represents an upper limit on the amount of continuous star formation. Finally, we also include 10 clusters from the sample of O’Dea et al. (2008), who compute SF rates based on *Spitzer* data, and dM/dt in a similar manner to us (open purple circles). We note that the SFRs derived from FUV data are systematically lower than those derived from $24\mu m$ *Spitzer* data. This is most likely due to our lack of an intrinsic extinction correction for these FUV data.

We find that the “efficiency” of star formation, defined as the current ratio of stars formed to gas cooling out of the ICM, can range from 1% to 50% over the full sample. This spread is independent of whether we only consider systems classified as star-forming based on their FUV/ $H\alpha$ ratios in Figure 5.2. For the majority of the 32 clusters in Figure 5.4, there is a tight correlation between SF rate and dM/dt with a typical efficiency between 10–50%. In the right panel of Figure 5.4, we show that the efficiency is nearly independent of the cluster temperature, with only a weak dependence which is primarily driven by highly extinguished systems. This suggests that the temperature of the surrounding ICM does not hamper the BCG’s ability to form stars. While not shown here, we also investigated the distribution of star formation efficiencies with the central entropy, K_0 , from Cavagnolo et al. (2009) and, similarly to T_X , find no correlation. In the following section we will discuss possible interpretations of this efficiency measure.

5.4 Discussion

5.4.1 Star Formation as an Ionization Source

In Crawford et al. (2005), a variety of ionization sources are discussed which could produce the observed $H\alpha$ emission in the cool cores of galaxy clusters. The purpose

of this HST survey was to investigate one of the most plausible ionization sources: photoionization by young stars. In Figures 5.2 and 5.3 we showed that, once the contribution to the FUV emission from old stellar populations is removed, the majority of the $H\alpha$ and FUV emission that we observe in cluster cores is roughly consistent with the star formation scenario. Based on the $FUV/H\alpha$ ratios, we identify three different types of system:

1. $FUV/H\alpha \gtrsim 10^{-12} \text{ Hz}^{-1}$. Suggests a starburst that has aged by at least 10 Myr. Two systems, Abell 0970 and Abell 2029, fulfill this criteria, while several others may fall into this category if their $H\alpha$ luminosity is significantly less than the measured upper limits.
2. $FUV/H\alpha \sim 10^{-13} \text{ Hz}^{-1}$. The $FUV/H\alpha$ ratios of these systems are consistent with continuous star formation or a recent (0–5 Gyr ago) burst of star formation. The filaments in Abell 1644, Abell 1795, Abell 2597, and part of Abell 2052, along with the nuclei of Abell 1795, Abell 1991, Abell 2151, and Abell 2597 appear to be star-forming.
3. $FUV/H\alpha \lesssim 10^{-14} \text{ Hz}^{-1}$. Suggests heating by fast shocks or some other source of hard ionization (e.g., cosmic rays, AGN). The filaments of Abell 2052 and Abell 1991, and the nuclei of Abell 2052 and Abell 2580 have $FUV/H\alpha$ ratios which are consistent with this picture, in the absence of internal reddening.

Figures 5.2 (inset) and 5.3 show that a large fraction of the systems which we observe fall between the regions describing shock heating and star formation. However, these data have not been corrected for intrinsic reddening due to dust. Correcting for a very modest reddening ($E(B-V) \sim 0.2$) would boost the FUV luminosity of these systems such that the $FUV/H\alpha$ ratio is consistent with star formation (see

Figure 5.2c and the lower panel of Figure 5.3). Unfortunately, the amount of reddening in the filaments and nuclei of these systems is currently not well constrained for very many systems, but typical values of $E(B-V)$ can range from 0–0.4 in the cores of galaxy clusters (Crawford et al. 1999). In the case of Abell 2052, for which we measure FUV/ $H\alpha$ ratios indicative of shock-heating *and* have an estimate of the amount of intrinsic reddening from Crawford ($E(B-V) = 0.22^{+0.36}_{-0.21}$), we can investigate whether correcting for this extinction would provide FUV/ $H\alpha$ ratios consistent with star-forming regions. Assuming a simple dust-screen model, correcting for a reddening of $E(B-V) = 0.22$ would transform a FUV/ $H\alpha$ ratio of $4.4 \times 10^{-15} Hz^{-1}$ in the filaments of Abell 2052 to $1.2 \times 10^{-14} Hz^{-1}$, which is consistent with the upper limit for shock-heated systems (see Figure 5.3). However if, contrary to expectations, the filaments have a slightly higher reddening than the nucleus, the FUV/ $H\alpha$ ratio may be even higher. Thus, it is certainly possible that the systems which we classify as shock-heated, or those which have ambiguous FUV/ $H\alpha$ ratios, may in fact be highly-obscured star-forming systems. We will address this possibility in significantly more detail in an upcoming study which will include long-slit spectroscopy of the $H\alpha$ filaments providing, for the first time, reddening estimates away from the nucleus in these systems (see §6 for more details).

An alternative explanation for the intermediate FUV/ $H\alpha$ ratios is that the IMF in the filaments is top-heavy ($\alpha \ll 2.35$). Again, the lower panel of Figure 5.3 shows that the peak of the FUV/ $H\alpha$ distribution is consistent with the value expected for O8V stars. There is a substantial amount of literature providing evidence for a top-heavy IMF in various environments including the Galactic center (Maness et al. 2007) and disturbed galaxies (Habergham et al. 2010). Thus, regardless of whether there is a small amount of dust or a slightly altered IMF, we suspect that the majority of the systems with intermediate FUV/ $H\alpha$ ratios are in fact star-

forming, with the exception of Abell 1991, Abell 2052, and Abell 2580, which have low FUV/H α ratios *and* morphologies which resemble bow-shocks and/or jets.

Due to our use of the F150LP filter to remove red leak contamination, we are considering only a very small wavelength range from 1400–1500Å. In this region, there may be line emission from [OIV] and various ionization states of sulfur due to gas cooling at $\sim 10^5$ K. In order to establish that we are indeed observing continuum emission from young stars, we have computed UV spectral energy distributions (SEDs) for 6 BCGs which have deep GALEX, XMM-OM, and HST UV data. These data are presented in the left panel of Figure 5.5. We see that, in general, the UV SED follows a powerlaw over the range of 1500–3000Å. The new HST data, depicted as colored stars in this plot, agree well with the extrapolation of the continuum to shorter wavelengths, suggesting that there is very little contamination from line emission. This also suggests that there is little contribution from a diffuse UV component. This is further emphasized in the right panel of Figure 5.5 where we show the residuals from the continuum fit for each of the 6 BCGs. Our measured FUV fluxes from these new HST data are consistent with the measurement of a UV continuum from archival GALEX and XMM-OM data.

The idea that massive, young stars may be responsible for heating the majority of the warm, ionized filaments observed in cool core clusters is certainly not a new one (see e.g., Heckman et al. 1989; Hu et al. 1985; McNamara & O’Connell 1989). Most recently, O’Dea et al. (2008), Hicks et al. (2010), and ourselves (§3 of this thesis) conducted MIR, UV and H α surveys, respectively, of cool core clusters and found a strong correlation between the SF rate and the cooling properties of cluster cores. However, this work extends these findings to include spatially-resolved SF rates, which the previous studies have been unable to provide. This allows us to say conclusively that the young stars and the warm, ionized gas are in close proximity

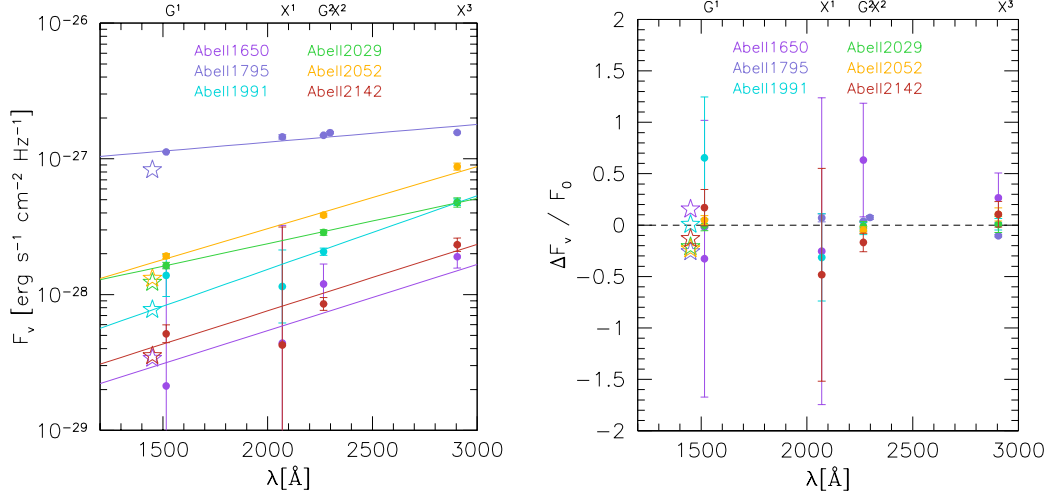


Figure 5.5 Left panel: UV spectral energy distributions (SEDs) for 6 cluster cores in our sample using data from GALEX and XMM-OM (§3). All fluxes have been corrected for Galactic extinction. The two *GALEX* filters are denoted by G^1 and G^2 , while the three *XMM-OM* filters are denoted by X^1 , X^2 and X^3 . The colored lines represent a fit to the GALEX+XMM-OM data, while the stars represent the FUV flux that we measure with HST ACS/SBC. Right panel: Residuals from the continuum fits shown in the left panel. Our new HST FUV data are consistent with the UV continuum fit, showing little evidence for additional line emission.

($\lesssim 1''$) in the vast majority of systems, offering a straightforward explanation for the heating of these filaments.

5.4.2 Star Formation Efficiencies in Cooling Flows

In §5.3, we provide estimates of the efficiency with which the cooling ICM is converted into stars, assuming that this is indeed the source of star formation. This assumption is based on the results of §3 and §4, which provided several strong links between the X-ray cooling properties and the warm, ionized gas. These estimates of star formation efficiency represent a constraint on the so-called “accreting box model” of star formation. The simplified model that we propose is that the ICM is allowed to cool rapidly in regions where cooling *locally* dominates over feedback

(Sharma et al. 2010). Our estimates of the ICM cooling rate, based on medium-resolution CXO spectra, are consistent with estimates based on high-resolution XMM grating spectroscopy by Peterson et al. (2003) for the five overlapping systems. Once the gas reaches temperatures of $\sim 10^{5.5}$ K, it can continue to cool rapidly via UV/optical/IR line emission without producing fluxes that are inconsistent with what are observed. In the standard way, star formation will proceed once the gas reaches low enough temperature and high enough density. Observations by Edge (2001) and Salomé & Combes (2003) show evidence for molecular gas in the cool cores of several galaxy clusters, consistent with this picture.

If the above scenario is correct, our estimate of the star formation efficiency provides a constraint on the fraction of hot gas that will be converted to stars, assuming a steady inflow of gas. In Figure 5.6 we provide a histogram of SF efficiencies for all of the systems in Figure 5.4 with non-zero X-ray cooling rates (dM/dt). The peak of this distribution is well defined at an efficiency of $14_{-8}^{+18}\%$, regardless of which SF indicator (UV, $H\alpha$, MIR) is used. We note that, while the distribution for UV- and MIR-determined SF rates both peak at roughly the same value, the UV-determined SF histogram extends to much lower values. The low-efficiency tail of this distribution may be an artifact produced by intrinsic extinction due to dust, to which the UV will be most sensitive, or may be indicative of a selection bias in the MIR sample. If we measure the peak efficiency based on the subsamples excluding the MIR and MIR+ $H\alpha$ (with no accompanying UV) data, we get $10_{-7}^{+25}\%$ and $14_{-8}^{+20}\%$, respectively. Thus, the peak value of 14% is not solely driven by the inclusion of MIR data.

The average efficiency of $14_{-8}^{+18}\%$, based on MIR, $H\alpha$ and UV data, is consistent with the estimates of star formation efficiency over the lifetime of a typical molecular cloud (20–50%; Kroupa 2001; Lada & Lada 2003). This large variance in star

formation efficiency may be due to differences in the ICM cooling and star formation timescales. Naturally, one would expect that there is some delay between the ICM cooling and the formation of stars, so that a reservoir of cold gas can accumulate and the formation of stars can be triggered. If this is indeed the case, one would expect to observe cooling-dominated periods (low SFE) followed by periods of strong star formation (high SFE) once the cold gas reservoir has reached some critical mass.

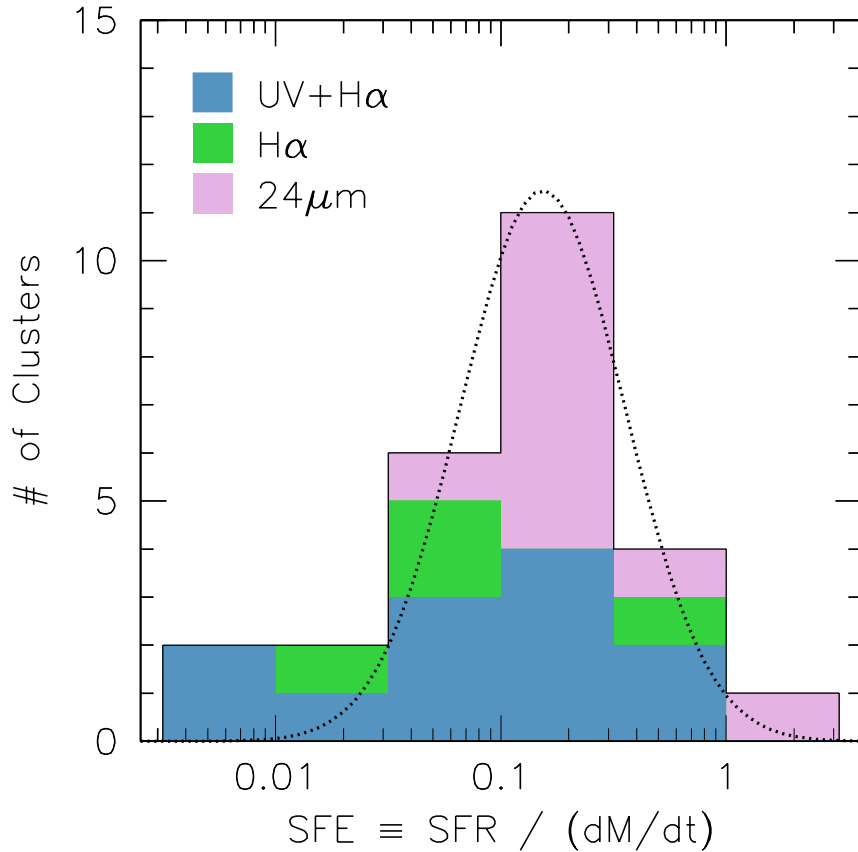


Figure 5.6 Distribution of measured star formation efficiencies from Figure 5.4 for 26 systems. Systems which are likely shock-heated (Abell 1991, Abell 2052, Abell 2580) have not been included. The additive contribution to the total histogram (solid black line) from UV+H α , H α and MIR data are shown in different colors following the color scheme in Figure 5.4. The dotted line shows a Gaussian fit to this histogram, which peaks at $14_{-8}^{+18}\%$ efficiency.

Over an ensemble of systems, the average SFE is then an estimate of the time-averaged efficiency of an accreting system in converting a steady stream of cooling gas into stars. An alternative explanation for the spread of observed efficiencies is that the source of feedback is episodic (e.g., AGN). In this scenario, an episode of strong feedback from the AGN would re-heat the reservoir of cool gas, severely reducing the potential for star formation. This may indeed be the case, since two of the three systems with the highest 1.4 GHz luminosity (Abell 2052, Abell 2597, and Perseus A) have $\text{SFE} \lesssim 0.1$.

The fact that Figure 5.6 shows a well-defined peak suggests that the fraction of stars formed in an accreting system is constant over long enough timescales. Our estimate of an average efficiency indicates that, for a steady-state system accreting hot gas which is then allowed to cool, roughly $4 M_{\odot}$ of gas will either be re-heated or expelled via winds for every $1 M_{\odot}$ of stars formed. This fraction of baryons in stars is consistent with the global fraction of $\sim 20\text{--}30\%$ required by simulations to reproduce the observed stellar mass function of galaxies (Somerville et al. 2008). Unlike measurements of SF efficiency for giant molecular clouds, this estimate does not require the use of a specific timescale, since we are assuming that stars are forming out of the inflow of hot gas and that the reservoir for this hot gas is inexhaustible.

5.5 Summary and Future Prospects

We have assembled a unique set of high spatial resolution far-UV and $\text{H}\alpha$ images for 15 cool core galaxy clusters. These data provide an unprecedented view of the thin, extended filaments in the cores of galaxy clusters. Based on the ratio of the far-UV to $\text{H}\alpha$ luminosity, the UV SED, and the far-UV and $\text{H}\alpha$ morphology, we conclude that the warm, ionized gas in the cluster cores is photoionized by massive,

young stars in all but a few (Abell 1991, Abell 2052, Abell 2580) systems. We show that the extended filaments, when considered separately, appear to be forming stars in the majority of cases, while the nuclei tend to have slightly lower FUV/H α ratios, suggesting either a harder ionization source or higher extinction. The slight deviation from expected FUV/H α ratios for continuous star formation (Leitherer et al. 1999) may be due to the fact that we have made no attempt to correct for intrinsic extinction due to dust or due to a top-heavy ($\alpha \ll 2.35$) IMF. We note that modest amounts of dust ($E(B-V) \sim 0.2$) in the most dense regions of the ICM can account for this deviation. Ideally, one would like spatially-resolved optical spectra of the filaments in order to constrain the heat source and intrinsic reddening of the filaments. We plan on addressing this issue in upcoming studies (see §6). Comparing the estimates of the star formation rates based on FUV, H α and MIR luminosities to the spectroscopically-determined X-ray cooling rate suggests a star formation efficiency of $14_{-8}^{+18}\%$. This value represents the time-averaged fraction, by mass, of gas cooling out of the ICM which turns into stars and agrees well with the stars-to-gas fraction of $\sim 20\text{--}30\%$ required by simulations to reproduce the observed stellar mass function. This result provides a new constraint for studies of star formation in accreting systems. Many aspects of this simplified scenario are still not well understood, including whether the star formation is similar to that seen in nearby spirals or vastly different. We intend to investigate such differences via an assortment of star formation indicators from the UV to radio in future work (see §6).

Chapter 6

Summary and Future Work

6.1 Summary

The goal of this project was to conduct a census of $H\alpha$ filaments in the cores of galaxy clusters in order to shed new light on three outstanding questions:

- i. How common are emission-line nebulae in cool core clusters and what is the typical morphology? Is Perseus A a “typical” system or an anomaly?
- ii. What process or processes are responsible for producing the observed thin filaments of cool gas?
- iii. What process or processes are responsible for ionizing the cool gas to produce the high $H\alpha$ surface brightnesses that are observed?

In an attempt to address all three of these questions, we have assembled the largest ever collection of galaxy groups and clusters with $H\alpha$ imaging using the Maryland-Magellan Tunable Filter. These data were supplemented with high spatial resolution X-ray (Chandra), UV (HST, GALEX, XMM-OM), near-IR (2MASS) and 1.4 GHz radio (VLA) data in order to get as complete a picture of the ICM, BCG

and AGN as possible for each system. These multi-wavelength data have yielded a number of interesting results, as we will now summarize:

1. Utilizing deep, high-spatial resolution $H\alpha$ and far-UV imaging of Abell 1795, we found compelling evidence for star-forming filaments extending 50kpc from the BCG nucleus. The cool filaments are likely a result of a cooling wake, due to a combination of rapid ICM cooling and the motion of the BCG through the cluster core (Figures 2.3–2.4).
2. For a sample of 23 galaxy clusters, we find that the morphology of filaments is either: (a) Complex, extended, thin $H\alpha$ -emitting filaments (8/23); (b) Nuclear, slightly elongated emission (7/23); (c) No detectable emission (8/23) (Figure 3.4).
3. The $H\alpha$ morphology is strongly correlated with the soft (0.5–2.0 keV) X-ray morphology. Systems with smooth, undisturbed X-ray halos tend to not have $H\alpha$ emission (Figure 3.4).
4. The observed $H\alpha$ filaments are unresolved in the transverse direction in all cases. This suggests a typical width of $< 700\text{pc}$ (Figure 3.4).
5. There is a strong correlation between the $H\alpha$ flux and both the X-ray determined cooling rate, dM/dt , and the central entropy over ~ 3 orders of magnitude (Figure 3.8).
6. The observed $H\alpha$ filaments never extend beyond the X-ray cooling radius, defined as the radius within which the ICM can cool in $< 5\text{Gyr}$ (Figure 3.9).
7. The cooling time of the X-ray gas coincident with the $H\alpha$ filaments is significantly lower than that of the surrounding ICM (Figure 3.13).

8. The presence and morphology of warm, ionized filaments is independent of environment (Figure 4.1).
9. The presence of H α emission is only weakly dependent on the global mass. That is, rich clusters and poor groups are equally likely, within a factor of 2, to harbor complex emission-line nebulae (Figure 4.3).
10. There is a weak correlation between the presence of warm filaments and the global gas fraction (51% confidence) and a strong correlation with global entropy (89% confidence) (Figure 4.3).
11. There is a strong correlation between the presence of H α filaments and the properties of the cool core, namely the X-ray cooling rate (72% confidence), the average temperature in the inner 100kpc (55% confidence), and the entropy at 50kpc (85% confidence) (Figure 4.4).
12. The cooling efficiency (cooling rate per unit gas mass) is higher in groups than in clusters, as is predicted in the absence of feedback (or under the assumption that feedback scales with gas mass) (Figure 4.8).
13. Cool core groups have typically lower radio luminosity than clusters due to the fact that a powerful AGN outburst in a group would destroy the cool core. We show evidence that this process is ongoing in three higher-mass systems (Figure 4.9).
14. Of the 15 systems with deep, high-resolution far-UV imaging, 12 have FUV/H α fluxes and morphologies consistent with photoionization by young stars (Figures 5.1–5.4).
15. The star formation rate inferred by a combination of UV, H α and mid-IR luminosities for 32 galaxies correlates with the X-ray cooling rate (Figure 5.4).

The efficiency of stars created out of the cooling flow implied by this correlation is $14_{-8}^{+18}\%$, which agrees well with the global fraction of baryons in stars (Figure 5.6).

As we discussed in §3 and §4, these results offer overwhelming evidence that the observed H α filaments are intimately linked to the cooling ICM (points 3–13 above). Our preferred scenario is that these filaments are the byproduct of thermal instabilities in the cooling ICM. The thinness of the observed filaments relative to their extent is reminiscent of the thin, filamentary structure seen in hydrodynamic simulations of cooling gas. Sharma et al. (2010) have shown that, in regions where cooling *locally* dominates over feedback, these filaments are an inevitable phase of the cooling. This simple explanation matches all of the observed trends noted above, requiring nothing more than a cooling ICM and anisotropic feedback (e.g., AGN jets).

Based on our work presented in §2 and §5 (points 1 and 14–15 above), we speculate that the dominant ionization mechanism in these filaments is photoionization by young stars. While optical line ratios from §2 for Abell 1795 and from the literature for a variety of other systems suggest that a harder ionization source may be necessary, the evidence for star-formation in these systems is too overwhelming to be ignored (see discussions in §1.5 and §5.1). The fact that the star formation rate is roughly 15% of the cooling rate, matching the observed universal baryon fraction in stars, is additional support for this hypothesis. In the $\sim 20\%$ of systems that are inconsistent with being photoionized by young stars, we propose that the dominant heating mechanism is fast shocks due to the very high H α /UV ratios. These shocks are likely a result of the dense, cool ICM being excavated by radio feedback from the AGN. This scenario is further supported by the fact that the shock-heated systems have consistently higher radio luminosity than their star-forming counterparts.

While this work has provided several important constraints on the formation and evolution of emission-line nebulae in cool core clusters, there are still several outstanding questions. Below, we describe follow-up projects which will utilize the results from this work in combination with new data to address some of these unanswered questions.

6.2 Future Work

6.2.1 Optical Spectroscopy of $H\alpha$ Filaments

Despite the overwhelming evidence for star formation in the cool cores of galaxy clusters from UV, IR, and sub-mm data, there is still much to be learned about the ionization source from optical spectroscopy of the cool filaments. Using the IMACS spectrograph on the Baade telescope at Magellan we have collected long-slit spectra for 8 galaxy clusters which exhibit complex, extended filaments (see Figure 6.1). These spectra will allow us to address several outstanding issues, including:

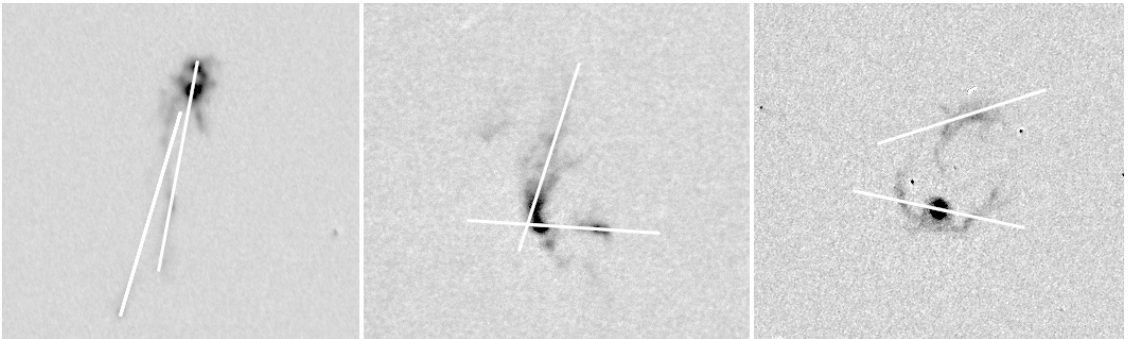


Figure 6.1 Examples of our long-slit spectroscopy positioning for Abell 1795, Seric 159-03, and Abell 2052.. For each system we align two slits in order to obtain maximum coverage of the filaments while also covering the nucleus with at least one of the slits.

- What are the radial velocity profiles along the filaments? Can we differentiate between infall and outflow scenarios with these data?

- How turbulent is the warm gas in these filaments? Is it consistent with the models of thermally unstable cooling?
- Can the optical line ratios rule out any additional ionization mechanisms? Are they consistent with the simple star formation model or do they require a mix of processes?
- In the systems that we classify as shock-heated based on their lack of UV emission, do the optical line ratios suggest shock-heating as well?
- How much reddening is there in the filaments? Do the reddening-corrected UV luminosities still agree with the expectation for continuous star formation?

A preliminary analysis of these data is currently underway, but early results suggest that a mixture of ionization processes may be necessary in all systems. In Figure 6.2 we show optical line ratios for four systems which show that the $[\text{O I}]/\text{H}\alpha$ line ratio is higher than expected for the systems classified as star-forming based on other diagnostics. Such a signature would be produced by slow shocks, which tend to increase $[\text{O I}]/\text{H}\alpha$ significantly more than the other diagnostic line ratios. We hope to create a model which combines star formation, both continuous and bursting, with fast and slow shocks in order to better match these data.

These data will represent the largest sample of deep optical spectroscopy of emission-line nebulae to date and will provide new constraints on the kinematics and source of ionization/heating in these complex filaments.

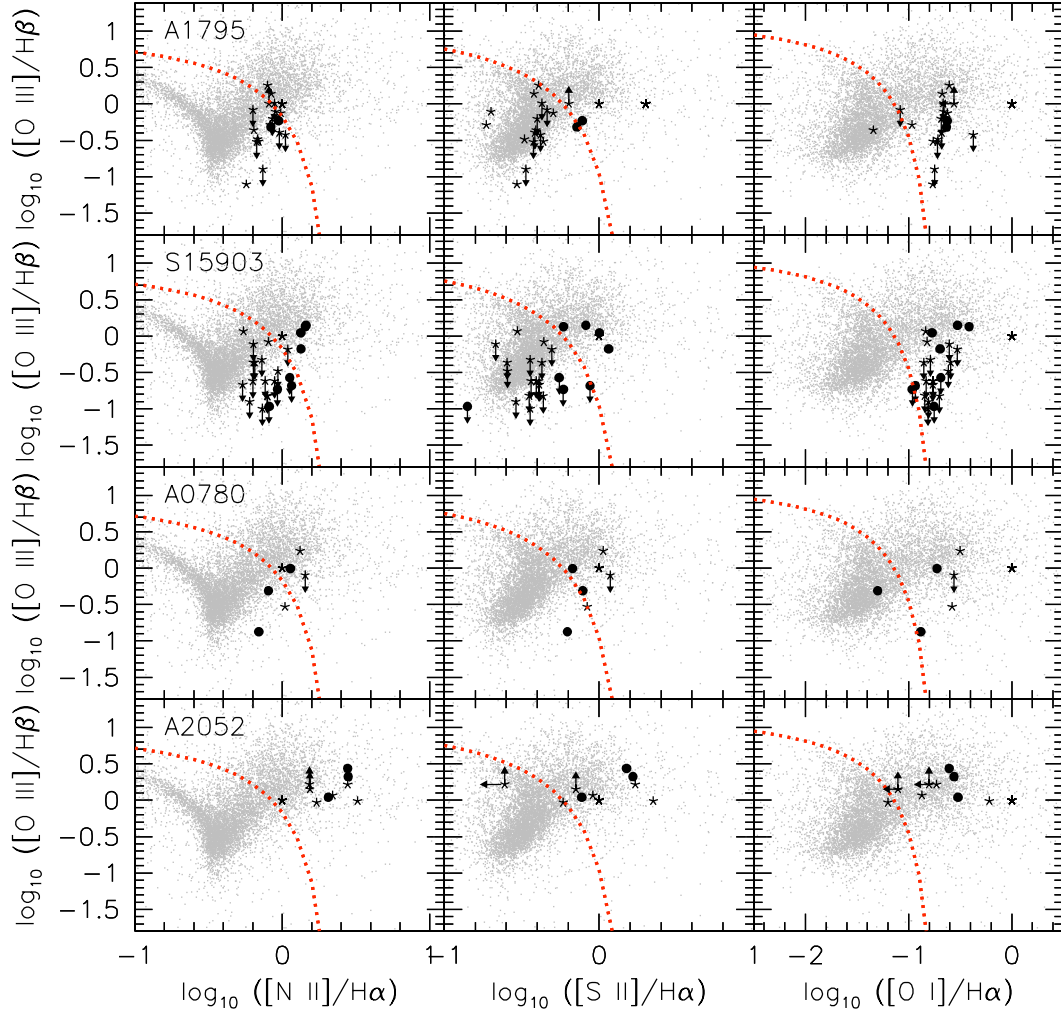


Figure 6.2 Tentative results from our spectroscopic survey of warm filaments in the cool cores of galaxy clusters. The $[\text{O III}]/\text{H}\beta$ line ratio is plotted against the $[\text{N II}]/\text{H}\alpha$, $[\text{S II}]/\text{H}\alpha$, and $[\text{O I}]/\text{H}\alpha$ ratios for 4 sample clusters. Black stars represent points in the filaments ($> 5''$ from the nucleus) while black circles represent nuclear data. The grey points represent the data from SDSS (Kewley et al. 2006) while the red line represents the maximum ratios for starburst galaxies (Kewley et al. 2001). We tentatively find that galaxies which we classified as star-forming based on their UV emission (Abell 1795 and Sersic 159-03) have optical line ratios which support this hypothesis. Abell 2052, which we classified as a shocked system, has very strong line ratios, reminiscent of those seen in AGN. We note that *all* systems appear to have higher than expected $[\text{O I}]/\text{H}\alpha$ ratios.

6.2.2 A Complete Multiwavelength View of the ICM at $z \sim 0$

The current picture of cooling in galaxy clusters involves a complicated balance between radiative cooling of the ICM and feedback from various sources including the central AGN, heat conduction from the outer layers inwards, and merging with subclusters or groups. While, individually, each of these processes can provide the required energy to offset cooling in a global sense, one would still expect to see regions of local imbalance between heating and cooling, leading to reduced cooling flows (see e.g., Sharma et al. 2010). These reduced cooling flows ($\sim 1\text{--}10 M_{\odot} \text{ yr}^{-1}$) have been observed in several X-ray studies of galaxy clusters, as we have shown throughout this work. Our unique database of multi-wavelength imaging and spectroscopy for a large sample of groups and clusters provides us with an opportunity to assemble a complete picture of the multiphase ICM and determine the extent to which there is still “missing gas”. In order to track down all of the ICM phases, we have obtained new and archival data at a wide range of energies, as shown in Table 6.2.2. This study represents the first ever census of the ICM at all temperatures for more than a few galaxy clusters. In §3 and §4, we presented deep, high spatial resolution imaging of the hot (X-ray) and warm ($H\alpha$) ICM phases. Our recently-approved Herschel program will provide deep imaging at 70, 100, 160, 250, 350 and $500\mu\text{m}$, along with imaging spectroscopy of the [C II] $158\mu\text{m}$ line for 11 cooling flow clusters. These photometric data, in combination with archival Spitzer data at $24\mu\text{m}$, will allow us to create accurate maps of the temperature and quantity of intracluster dust. Such maps will allow us to properly quantify the amount of unobscured, ongoing star formation, as well as determine the role of dust in the ICM cooling process. Additionally, the imaging spectroscopy of the [C II] $158\mu\text{m}$ line will provide an estimate of the amount of cooling gas below 10^4 K, along with the spatial

distribution of this cooling. These maps will be compared to 2-D X-ray cooling maps in order to determine if the gas cooling in the X-ray and IR are spatially coincident. Our ongoing sub-mm program (CARMA, PI: M. McDonald; SMA, PI: L. Wei, Co-PI: M. McDonald) will allow us to establish a firm estimate of the amount and morphology of cold gas in the cluster core and act as a precursor study for future ALMA projects. Finally, our deep far-UV HST imaging (§5) provides an estimate of the mass of cold gas that has turned into stars. By comparing the total mass in young stars and in warm, cool, and cold gas phases to the estimates of the X-ray cooling flow, one can determine whether there is any discrepancy and, if so, the magnitude of this discrepancy for an ensemble of systems. Furthermore, the combination of X-ray cooling maps, dust maps and IR cooling maps will provide new insights into the interplay between various cooling processes (e.g., thermal bremsstrahlung, line cooling, dust cooling) in the intracluster medium. These results will provide a crucial test of the cooling flow model, and potentially offer the long sought-after answer to the cooling flow problem.

Table 6.1 Multi-wavelength data available for our sample of cool core clusters

Observatory	Obs Type	Wavelength	Source (Reference)	Interesting Science Probed
CXO	Phot+Spec	X-ray	Archive	Hot ICM properties, X-ray cooling flow
HST	Phot	far UV	New (M09, M11b)	Star formation, young stars
GALEX	Phot	near UV	New & Archive (M10)	Star formation, young stars
XMM-OM	Phot	near-UV	Archive	Star formation, young stars
MMTF	Phot	H α	New (M10, M11a)	Warm, ionized gas
MMTF	Phot	$\sim 6700\text{\AA}$	New (M10, M11a)	Stellar Continuum
Magellan	Spec	$\sim 4000\text{--}8000\text{\AA}$	New (M11c)	Kinematics & excitation of warm gas
2MASS	Phot	near IR	Archive	Old Stellar Populations
Spitzer	Phot	near-mid IR	Archive	Dust content
Herschel	Phot+Spec	mid-far IR	New*	Dust content, cooling gas
SMA	Phot+Spec	sub-mm	New*	Cold, molecular gas
CARMA	Phot+Spec	sub-mm	New*	Cold, molecular gas
VLA	Phot	1.4 GHz	Archive	Synchrotron emission from AGN jets

Table 6.1: Multi-wavelength data available for our sample of cooling flow clusters. The observations marked by an asterisk have recently received TAC approval and are scheduled for observation in 2010/11. This broad energy coverage allows us to track down all phases of the ICM and build a complete picture of the ongoing heating and cooling processes. The observations marked by an asterisk are pending TAC approval.

6.2.3 The Evolution of Feedback and Cooling in Cluster Cores

An important aspect of cool core clusters, which has received little attention until recently, is their evolution over time. The number of cool cores as a function of redshift provides crucial insights into our understanding of both structure formation and AGN feedback. In a simplified picture, the time-dependent fraction of clusters with cool cores can be thought of as a tracer for the cooling/feedback imbalance. The latter is indeed critical for models of galaxy cluster and structure formation. In recent years, multiple independent surveys have attempted to quantify the fraction of cool cores via a variety of methods (Figure 6.3). The evolution of cool cores appears to drop off rapidly from $0 < z < 0.5$, offering tantalizing evidence for a ~ 3 Gyr duty cycle for strong AGN feedback. However, a survey by Santos et al. (2008), which classified cool cores based on the central X-ray surface brightness, found that by $z \sim 1$ the fraction of cool cores resembles that at $z \sim 0$, suggesting an earlier epoch at which cooling dominated feedback, potentially before BCGs were firmly established.

The detection of cool cores at X-ray wavelengths becomes exceedingly difficult at high redshift, but there may be a more promising method. In this work (§3) we have shown that the presence of $H\alpha$ filaments is evidence for cooling flows, with the $H\alpha$ luminosity being directly correlated with the X-ray cooling rate (Figure 3.8). The detection of cooling flows via optical emission is preferable to X-ray detection due to the relatively ease with which one can measure $L_{H\alpha}$ (optical/NIR photometry versus X-ray spectroscopy), the lower uncertainty in $L_{H\alpha}$ (10%, compared to 60% for X-ray measurements of the cooling rate) and the higher sensitivity and better spatial resolution of optical detectors relative to X-ray detectors ($< 0.1''$ for HST

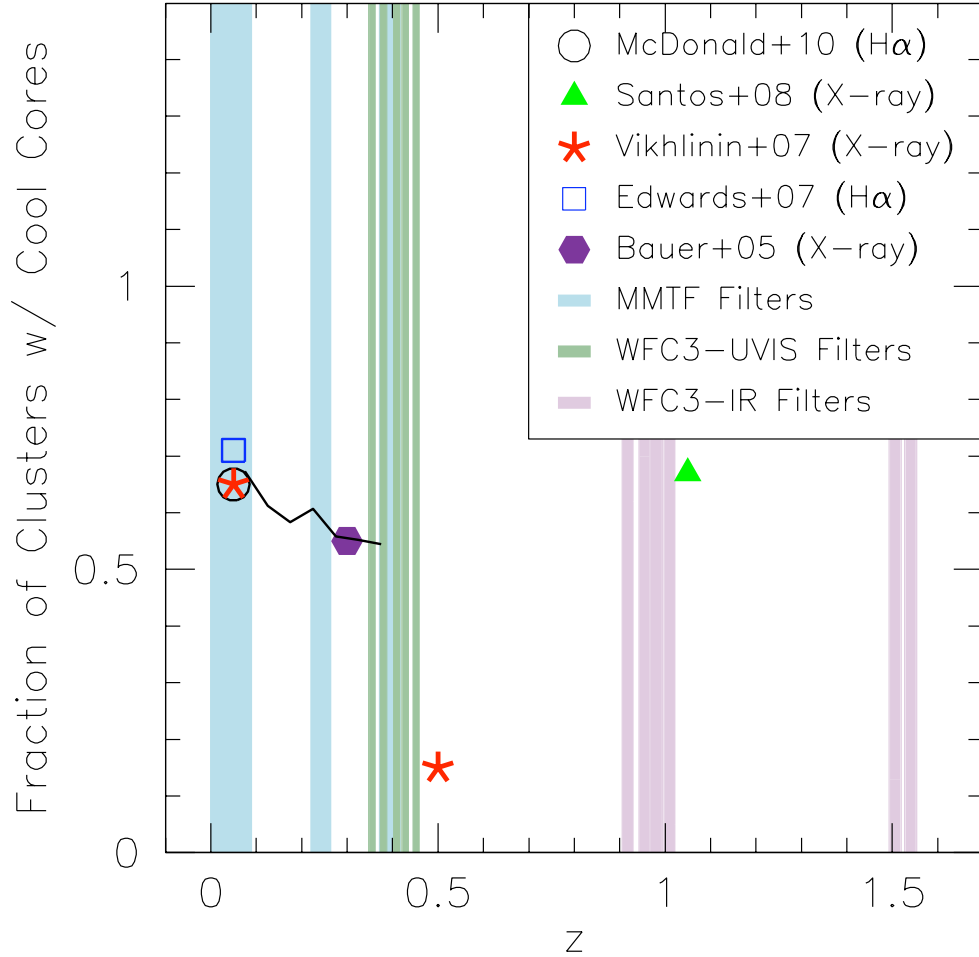


Figure 6.3 Fraction of galaxy clusters with cool cores as a function of redshift, as measured by multiple groups. The vertical bars represent the redshift coverage for a combined MMTF–HST survey of H α in cooling flow clusters. With simultaneous surveys of modest size (~ 20 clusters in each bin), an additional four points could be added to this plot at $z = 0.25, 0.4, 0.95$ and 1.5 . Additionally, SDSS spectroscopy can be used to constrain the *nuclear* H α emission at low redshift, as the solid black line demonstrates (McDonald in prep). These new observations would firmly establish the redshift evolution of cool cores, providing critical constraints on cooling and feedback scenarios.

compared to $> 1''$ for CXO). In Figure 6.3, the ability of a combined MMTF and HST survey in establishing the evolution of cool cores is demonstrated. In this work, we have surveyed 23 clusters and 10 groups at redshifts $0 < z < 0.1$. Using order-blocking and narrow-band filters on the MMTF and HST, respectively, we will determine the fraction of cool cores at $z \sim 0.25, 0.4, \text{ and } 1.0$. We have applied for 24 orbits on HST and will apply for MMTF time through the MIT guaranteed access in order to complete these programs. While the number of known clusters at such high redshift is currently quite small, the timing of this survey is fortuitous, as multiple telescopes (e.g., Planck, South Pole Telescope) are currently wrapping up surveys designed to detect hundreds of high-redshift clusters utilizing the Sunyaev-Zeldovich effect and will be releasing their catalogues over the coming years. The enhanced spatial resolution of HST will offset the effect of increasing distance, such that at $z = 0.5$ the spatial resolution will be similar to our MMTF observations at $z \sim 0.1$, allowing the detection of extended, ionized filaments at higher redshift (Figure 6.4). Furthermore, the preliminary results of an SDSS study of $H\alpha$ emission in 32,000+ BCGs (solid black line in Figure 6.3; McDonald in prep.) shows that

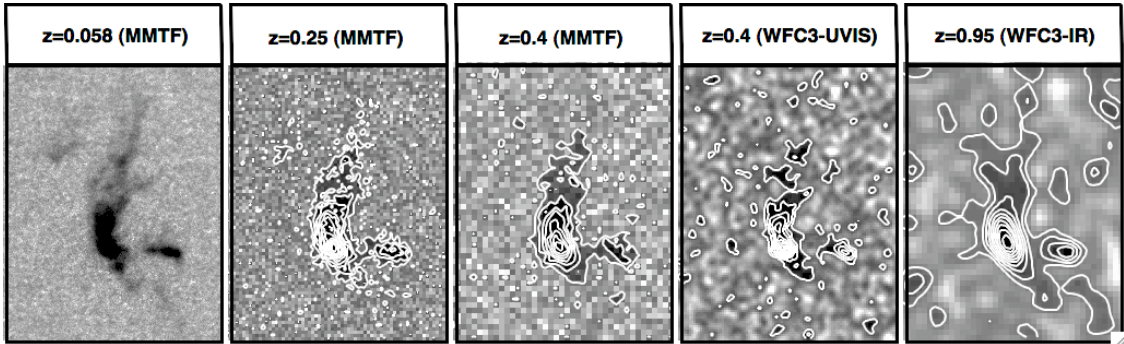


Figure 6.4 Simulated continuum-subtracted $[N II]+H\alpha$ images of the BCG in Seric 159-03 using the MMTF and HST WFC3 over a range in redshift. Extended emission in the north and east direction are detected out to $z = 0.95$. Exposure times are 3600s for MMTF and 8000s (2.7 orbits) for WFC3. The combination of spatial resolution and depth are required to separate the filaments from AGN contamination. Contour levels represents $1-\sigma, 2-\sigma, 3-\sigma, \text{ etc.}$ above the background.

the time-dependent frequency with which we detect $H\alpha$ emission matches well the results of X-ray surveys over the range $0 < z < 0.4$. Due to the straightforward nature of narrow-band imaging, we require only modest amounts of observing time on both Magellan (~ 1 hour per cluster) and HST (2 orbits per cluster), in order to detect extended emission out to $z = 1$. This can be compared to the >100 ks X-ray exposures required per cluster to do the same experiment (Santos et al. 2008). This new technique of identifying and quantifying cooling flows in galaxy clusters will have a tremendous impact on our understanding of the evolving balance between cooling and feedback, and on galaxy cluster evolution as a whole.

6.3 Conclusions

This work represents a significant step forward in the study of cool cores in galaxy groups and clusters. We have provided compelling evidence that the warm, ionized filaments seen in these cool cores are intimately linked to the cooling ICM and are likely a byproduct of thermally-unstable cooling. The high $H\alpha$ surface brightnesses of these filaments is likely due to ongoing or burst-like star formation, as is evidenced by the significant UV and IR excess in systems with complex filaments. This new understanding of the optical filaments in cluster cores allows us to glimpse the cooling properties of the ICM in the optical, rather than the X-ray, allowing for a powerful new diagnostic tool in studies of galaxy clusters. Furthermore, the wealth of data acquired for this project have spawned several follow-up projects which should continue to unravel the mysteries of the ICM for years to come.

Appendix A

Properties of Individual Clusters

In this section, we comment on the clusters in our sample for which the $H\alpha$ emission is interesting in terms of its flux (or lack thereof) or morphology. We discuss possible formation mechanisms and implications on current theories as they apply to each case.

Abell 0085

A large ring can be seen in the X-ray image south of the cluster core, resembling the outer edge of a bubble. Unlike Abell 2052, however, this X-ray edge has no $H\alpha$ counterpart. This cluster is one of three which has asymmetric $H\alpha$ emission on small scales only. Based on the high $H\alpha$ /NUV ratio, it is possible that the gas could be ionized by a recent burst of star formation in the BCG center. Previous works (e.g., Durret et al. 2005) have suggested that this cluster has undergone intense merging activity, based on the temperature/metallicity maps from XMM-Newton. This scenario is consistent with the relatively high temperature and entropy that we measure, compared to clusters with more filamentary $H\alpha$ emission.

Abell 0133

A single, thin $H\alpha$ filament extends northeast from the center of this cluster for ~ 25 kpc. This filament is only barely detected, but the detection significance is increased slightly by the exact coincidence with an X-ray filament. This cluster appears to be very similar to Abell 1795 in both morphology (long, thin strands in a single direction) and ionization mechanism (NUV/ $H\alpha$ ratio is consistent with ongoing star formation). Based on XMM-Newton observations, Fujita et al. (2004) came to the conclusion that this X-ray filament is likely due to a buoyant radio bubble, since it was the only scenario put forward that did not directly oppose their results. However, we show that the metallicity in the filament is consistent with coming from larger radii, *not* smaller radii, therefore it is inconsistent with the buoyant radio bubble scenario.

Abell 0478

The X-ray morphology and $H\alpha$ morphology match up very well in this cluster, as seen in Figure 3.4 and also the unsharp masked X-ray image in Sanderson et al. (2005). There appears to be two nuclei in both the $H\alpha$ and X-ray emission, while the continuum image is that of a normal, undisturbed elliptical galaxy. The available UV data for this cluster is quite poor, but it appears that there is a significant amount of on-going star formation in the center of this cluster. However, the combination of shallow data and high extinction ($E(B-V)=0.52$) makes it difficult to trust these data. Without a deeper UV image of the cluster core, it is difficult to determine the heating source. This cluster also has the highest $H\alpha$ luminosity of any other in our sample and a significant amount of structure extending beyond the optical radius of the galaxy, making it one of the most intriguing clusters in our sample.

Abell 0496

This cluster has arguably the most interesting H α morphology of any cluster in our sample. There are at least 5 distinct filaments, with various shapes and directions. The two longest filaments run parallel to each other for ~ 12 kpc. Using unsharp mask HST images, Hatch et al. (2007) found significant structure in the dust which may be coincident with some of our detected H α filaments. Dupke et al. (2007) also discuss the presence of a cold front, as can be clearly seen in Figure 3.4, which may be due to an off-center encounter with a massive dark matter halo roughly 0.5 Gyr ago. Regardless of the method of producing this morphology in the X-ray, we note that the H α filaments do not extend beyond the cold front in this cluster (~ 15 kpc), despite the fact that the cooling radius is nearly 50 kpc.

Abell 0780 (Hydra A)

Wise et al. (2007) present a summary of the X-ray and radio properties of this cluster, showing the excellent correlation between the radio jets and the X-ray cavities. The arcing H α filament that we detect north of the BCG appears to be spatially correlated with the radio jet. The NUV emission for this cluster is very bright, but it is unclear if it has morphological similarities to the H α emission without higher resolution UV imaging. A very bright star to the west of the BCG made the data reduction slightly more complicated for this cluster, leading to a lower S/N in the region with the southern filaments.

Abell 1644

An arcing trail of cool gas extends south from the core of this cluster. This morphology is likely the result of an off-axis encounter with a subcluster (Reiprich et al. 2004). We detect a curved $H\alpha$ filament coincident with the cool x-ray gas, as well as two perpendicular $H\alpha$ strands to the west and north of the cluster core. These previously-undetected filaments have large length-width ratios, suggesting that turbulence must be low or the magnetic field strength must be high in this cluster core. Additionally, we find very little evidence for an AGN in this cluster, in terms of the radio power, X-ray morphology and hard X-ray flux.

Abell 1795

A pair of thin ($\sim 100\text{pc}$), intertwined filaments extend south from the cluster core for $\sim 50\text{ kpc}$ (§2). These filaments appear to be heated by strands of young stars which lie along the full extent of both filaments. However, the elevated $[\text{NII}]/H\alpha$ ratios found in MV09 and the literature suggest that either the star formation is dominated by massive stars, or another ionizing mechanism is also important. These twin filaments are coincident with a giant X-ray filament which is unresolved by Chandra. Additionally, this cluster has powerful radio jets which are offset in angle from the filament direction. The cooling wake hypothesis may be valid in this case, as the BCG appears to have a strong peculiar velocity relative to the cluster (Oegerle & Hill 2001). However, we note that a cooling wake should intuitively have slightly more turbulence than a straight cooling flow, which is inconsistent with the picture of long, thin filaments that we observe.

Abell 2029

This cluster is the most massive in our sample and also has the most massive BCG. However, despite being exceptionally bright at X-ray, NUV and 1.4 GHz, we detect no H α emission. A clue as to why this may be lies in the unsharp mask image of the X-ray gas. Unlike most other massive clusters, Abell 2029 is quite symmetric with no signs of any structure in the X-ray image. This suggests that the X-ray structure which we observe in all H α -bright clusters is necessary to produce the filamentary H α emission. This provides yet another link between the H α filaments and the cooling X-ray gas and, at the same time, offers a counter-argument to the idea of buoyant radio bubbles being responsible for the emission.

Abell 2052

The H α emission surrounding the BCG in this cluster is coincident with radio-blown bubbles in the central region of the cluster. These bubbles to the north and south of the cluster core are filled with radio emission, which likely originated from the AGN within the BCG (Blanton et al. 2003). Since the H α emission is seen primarily along the edges of the northern bubble, we suspect that shocks may be responsible for the heating in this case. The very low NUV/H α ratio seen in Figures 3.6 and 5.2 further supports this hypothesis. As this cluster is more strongly influenced by the AGN than any other cluster in our sample, it is an outlier in some of our plots. As an example, in Figure 3.12 Abell 2052 is represented by the point with the lowest on-filament metal abundance. This abundance measurement is most consistent with the core abundance, not the abundance at the cooling radius. Thus it is possible that our simple picture of the H α filaments being tied to the cooling flow may not apply to this cluster.

Abell 4059

The core of this cluster contains two peaks, only one of which is reproduced in $H\alpha$. The $H\alpha$ emission extends for a short distance to the west, coincident with an extended arm in the X-ray image (Choi et al. 2004; Reynolds et al. 2008). The radio emission from this cluster extends north, perpendicular to the direction of $H\alpha$ emission, suggesting that the radio jets are not playing a role in the heating.

Sersic 159-03

The optical emission in this cluster has been observed by Jaffe et al. (2005) and more recently by Oonk et al. (2010). Both authors find molecular gas which traces the ionized gas out to 20 kpc. We are able to detect $H\alpha$ to 35 kpc, where the surface brightness blends into the background. It is likely that a deeper exposure would detect the ionized gas out to the cooling radius of ~ 60 kpc. There is no evidence for an AGN in the core of this cluster, despite the fact that it has some of the most extended and complex filaments. This suggests that the phenomenon of warm ionized filaments in clusters is likely independent of the presence of an AGN.

Appendix B

Glossary

2MASS	Two-Micron All-Sky Survey
ACS	Advanced Camera for Surveys
AGN	Active galactic nucleus/nuclei
BCG	Brightest cluster galaxy
CXO	Chandra X-ray Observatory
dM/dt	X-ray cooling rate [$M_{\odot} \text{ yr}^{-1}$]
FUV	Far ultraviolet
GALEX	Galaxy Evolution Explorer
H α	Hydrogen recombination line
HST	Hubble Space Telescope
ICM	Intracluster medium
IMF	Initial mass function
IR	Infrared
ISM	Interstellar Medium
MHD	Magnetohydrodynamic
MMTF	Maryland-Magellan Tunable Filter
NIR	Near infrared
NUV	Near ultraviolet
NVSS	NRAO VLA Sky Survey
PSF	Point spread function

R_{cool}	X-ray cooling radius
$R_{H\alpha}$	Maximum extent of $H\alpha$ emission
SBC	Solar Blind Channel
SED	Spectral energy distribution
SF	Star formation
FH	Star formation history
SFR	Star formation rate
S/N	Signal-to-noise ratio
UV	Ultraviolet
VLA	Very Large Array
XMM	X-ray Multi-Mirror Mission
XMM-OM	XMM Optical Monitor

Bibliography

- Abazajian, K. N., Adelman-McCarthy, J. K., Agüeros, M. A., Allam, S. S., Allende Prieto, C., An, D., Anderson, K. S. J., Anderson, S. F., Annis, J., Bahcall, N. A., & et al. 2009, *ApJS*, 182, 543
- Abell, G. O. 1958, *ApJS*, 3, 211
- Abell, G. O., Corwin, Jr., H. G., & Olowin, R. P. 1989, *ApJS*, 70, 1
- Allen, S. W. 1995, *MNRAS*, 276, 947
- Anders, E., & Grevesse, N. 1989, *Geochim. Cosmochim. Acta*, 53, 197
- Arnaud, K. A. 1996, in *Astronomical Society of the Pacific Conference Series*, Vol. 101, *Astronomical Data Analysis Software and Systems V*, ed. G. H. Jacoby & J. Barnes, 17–+
- Bell, E. F., & de Jong, R. S. 2001, *ApJ*, 550, 212
- Bildfell, C., Hoekstra, H., Babul, A., & Mahdavi, A. 2008, *MNRAS*, 389, 1637
- Bîrzan, L., Rafferty, D. A., McNamara, B. R., Wise, M. W., & Nulsen, P. E. J. 2004, *ApJ*, 607, 800
- Bland-Hawthorn, J., & Jones, D. H. 1998, *PASA*, 15, 44
- Blanton, E. L., Randall, S. W., Douglass, E. M., Sarazin, C. L., Clarke, T. E., & McNamara, B. R. 2009, *ApJ*, 697, L95
- Blanton, E. L., Sarazin, C. L., & McNamara, B. R. 2003, *ApJ*, 585, 227
- Boehringer, H., & Werner, N. 2009, *ArXiv e-prints*

Brighenti, F., & Mathews, W. G. 2003, *ApJ*, 587, 580

Cardelli, J. A., Clayton, G. C., & Mathis, J. S. 1989, *ApJ*, 345, 245

Cardiel, N., Gorgas, J., & Aragon-Salamanca, A. 1995, *MNRAS*, 277, 502

Cattaneo, A., & Teyssier, R. 2007, *MNRAS*, 376, 1547

Cavagnolo, K. W., Donahue, M., Voit, G. M., & Sun, M. 2008, *ApJ*, 683, L107

—. 2009, *ApJS*, 182, 12

Ceverino, D., Dekel, A., & Bournaud, F. 2010, *MNRAS*, 404, 2151

Choi, Y., Reynolds, C. S., Heinz, S., Rosenberg, J. L., Perlman, E. S., & Yang, J. 2004, *ApJ*, 606, 185

Churazov, E., Brüggén, M., Kaiser, C. R., Böhringer, H., & Forman, W. 2001, *ApJ*, 554, 261

Condon, J. J., Cotton, W. D., Greisen, E. W., Yin, Q. F., Perley, R. A., Taylor, G. B., & Broderick, J. J. 1998, *AJ*, 115, 1693

Conroy, C., & Ostriker, J. P. 2008, *ApJ*, 681, 151

Conselice, C. J., Gallagher, III, J. S., & Wyse, R. F. G. 2001, *AJ*, 122, 2281

Cowie, L. L., Fabian, A. C., & Nulsen, P. E. J. 1980, *MNRAS*, 191, 399

Cowie, L. L., Hu, E. M., Jenkins, E. B., & York, D. G. 1983, *ApJ*, 272, 29

Crawford, C. S., Allen, S. W., Ebeling, H., Edge, A. C., & Fabian, A. C. 1999, *MNRAS*, 306, 857

Crawford, C. S., Sanders, J. S., & Fabian, A. C. 2005, *MNRAS*, 361, 17

Croton, D. J., Springel, V., White, S. D. M., De Lucia, G., Frenk, C. S., Gao, L., Jenkins, A., Kauffmann, G., Navarro, J. F., & Yoshida, N. 2006, *MNRAS*, 365, 11

David, L. P., Jones, C., Forman, W., & Daines, S. 1994, *ApJ*, 428, 544

Donahue, M., Horner, D. J., Cavagnolo, K. W., & Voit, G. M. 2006, *ApJ*, 643, 730

Dopita, M. A., & Sutherland, R. S. 1996, *ApJS*, 102, 161

- Dupke, R., White, III, R. E., & Bregman, J. N. 2007, *ApJ*, 671, 181
- Durret, F., Lima Neto, G. B., & Forman, W. 2005, *A&A*, 432, 809
- Edge, A. C. 2001, *MNRAS*, 328, 762
- Edwards, L. O. V., Hudson, M. J., Balogh, M. L., & Smith, R. J. 2007, *MNRAS*, 379, 100
- Egami, E., Misselt, K. A., Rieke, G. H., Wise, M. W., Neugebauer, G., Kneib, J., Le Floch, E., Smith, G. P., Blaylock, M., Dole, H., Frayer, D. T., Huang, J., Krause, O., Papovich, C., Pérez-González, P. G., & Rigby, J. R. 2006, *ApJ*, 647, 922
- Ettori, S., Fabian, A. C., Allen, S. W., & Johnstone, R. M. 2002, *MNRAS*, 331, 635
- Fabian, A. C. 1994, *ARA&A*, 32, 277
- Fabian, A. C., Nulsen, P. E. J., & Canizares, C. R. 1984, *Nature*, 310, 733
- Fabian, A. C., Sanders, J. S., Allen, S. W., Crawford, C. S., Iwasawa, K., Johnstone, R. M., Schmidt, R. W., & Taylor, G. B. 2003, *MNRAS*, 344, L43
- Fabian, A. C., Sanders, J. S., Ettori, S., Taylor, G. B., Allen, S. W., Crawford, C. S., Iwasawa, K., & Johnstone, R. M. 2001, *MNRAS*, 321, L33
- Fabian, A. C., Sanders, J. S., Ettori, S., Taylor, G. B., Allen, S. W., Crawford, C. S., Iwasawa, K., Johnstone, R. M., & Ogle, P. M. 2000, *MNRAS*, 318, L65
- Fabian, A. C., Sanders, J. S., Taylor, G. B., Allen, S. W., Crawford, C. S., Johnstone, R. M., & Iwasawa, K. 2006, *MNRAS*, 366, 417
- Fabian, A. C., Voigt, L. M., & Morris, R. G. 2002, *MNRAS*, 335, L71
- Fakhouri, O., & Ma, C. 2010, *MNRAS*, 401, 2245
- Ferland, G. J., Fabian, A. C., Hatch, N. A., Johnstone, R. M., Porter, R. L., van Hoof, P. A. M., & Williams, R. J. R. 2008, *MNRAS*, 386, L72
- . 2009, *MNRAS*, 392, 1475
- Fujita, Y., Sarazin, C. L., Reiprich, T. H., Andernach, H., Ehle, M., Murgia, M.,

- Rudnick, L., & Slee, O. B. 2004, *ApJ*, 616, 157
- Ge, J. P., & Owen, F. N. 1993, *AJ*, 105, 778
- Giodini, S., Pierini, D., Finoguenov, A., Pratt, G. W., Boehringer, H., Leauthaud, A., Guzzo, L., Aussel, H., Bolzonella, M., Capak, P., Elvis, M., Hasinger, G., Ilbert, O., Kartaltepe, J. S., Koekemoer, A. M., Lilly, S. J., Massey, R., McCracken, H. J., Rhodes, J., Salvato, M., Sanders, D. B., Scoville, N. Z., Sasaki, S., Smolcic, V., Taniguchi, Y., Thompson, D., & the COSMOS Collaboration. 2009, *ApJ*, 703, 982
- Gómez, P. L., Loken, C., Roettiger, K., & Burns, J. O. 2002, *ApJ*, 569, 122
- Guo, F., & Oh, S. P. 2008, *MNRAS*, 384, 251
- Habergham, S. M., Anderson, J. P., & James, P. A. 2010, *ApJ*, 717, 342
- Hamuy, M., Suntzeff, N. B., Heathcote, S. R., Walker, A. R., Gigoux, P., & Phillips, M. M. 1994, *PASP*, 106, 566
- Hamuy, M., Walker, A. R., Suntzeff, N. B., Gigoux, P., Heathcote, S. R., & Phillips, M. M. 1992, *PASP*, 104, 533
- Hansen, L., Jørgensen, H. E., Nørgaard-Nielsen, H. U., Pedersen, K., Goudfrooij, P., & Linden-Vørnle, M. J. D. 2000, *A&A*, 356, 83
- Hatch, N. A., Crawford, C. S., & Fabian, A. C. 2007, *MNRAS*, 380, 33
- Hattori, M., Yoshida, T., & Habe, A. 1995, *MNRAS*, 275, 1195
- Heckman, T. M., Baum, S. A., van Breugel, W. J. M., & McCarthy, P. 1989, *ApJ*, 338, 48
- Hicks, A. K., & Mushotzky, R. 2005, *ApJ*, 635, L9
- Hicks, A. K., Mushotzky, R., & Donahue, M. 2010, *ApJ*, 719, 1844
- Hu, E. M., Cowie, L. L., & Wang, Z. 1985, *ApJS*, 59, 447
- Jaffe, W., Bremer, M. N., & Baker, K. 2005, *MNRAS*, 360, 748
- Johnson, R. E., Markevitch, M., Wegner, G. A., Jones, C., & Forman, W. R. 2010,

- ApJ, 710, 1776
- Johnstone, R. M., Fabian, A. C., & Nulsen, P. E. J. 1987, MNRAS, 224, 75
- Kennicutt, Jr., R. C. 1998, ARA&A, 36, 189
- Kewley, L. J., Dopita, M. A., Sutherland, R. S., Heisler, C. A., & Trevena, J. 2001, ApJ, 556, 121
- Kewley, L. J., Groves, B., Kauffmann, G., & Heckman, T. 2006, MNRAS, 372, 961
- Kroupa, P. 2001, MNRAS, 322, 231
- Krumholz, M. R., & McKee, C. F. 2005, ApJ, 630, 250
- Lada, C. J., & Lada, E. A. 2003, ARA&A, 41, 57
- Lauer, T. R., Faber, S. M., Gebhardt, K., Richstone, D., Tremaine, S., Ajhar, E. A., Aller, M. C., Bender, R., Dressler, A., Filippenko, A. V., Green, R., Grillmair, C. J., Ho, L. C., Kormendy, J., Magorrian, J., Pinkney, J., & Siopis, C. 2005, AJ, 129, 2138
- Leccardi, A., & Molendi, S. 2008, A&A, 486, 359
- Leitherer, C., Schaerer, D., Goldader, J. D., González Delgado, R. M., Robert, C., Kune, D. F., de Mello, D. F., Devost, D., & Heckman, T. M. 1999, ApJS, 123, 3
- Lequeux, J. 2005, The interstellar medium, ed. Lequeux, J.
- Lim, J., Ao, Y., & Dinh-V-Trung. 2008, ApJ, 672, 252
- Loewenstein, M., & Fabian, A. C. 1990, MNRAS, 242, 120
- Mal'ushkin, L. 2001, ApJ, 554, 561
- Maness, H., Martins, F., Trippe, S., Genzel, R., Graham, J. R., Sheehy, C., Salaris, M., Gillessen, S., Alexander, T., Paumard, T., Ott, T., Abuter, R., & Eisenhauer, F. 2007, ApJ, 669, 1024
- McCarthy, I. G., Schaye, J., Ponman, T. J., Bower, R. G., Booth, C. M., Dalla Vecchia, C., Crain, R. A., Springel, V., Theuns, T., & Wiersma, R. P. C. 2010, MNRAS, 406, 822

- McDonald, M., & Veilleux, S. 2009, *ApJ*, 703, L172
- McDonald, M., Veilleux, S., & Mushotzky, R. 2011a, *ApJ*, 731, 33
- McDonald, M., Veilleux, S., Rupke, D. S. N., & Mushotzky, R. 2010, *ApJ*, 721, 1262
- McDonald, M., Veilleux, S., Rupke, D. S. N., Mushotzky, R., & Reynolds, C. 2011b,
ArXiv e-prints
- McNamara, B. R., & O'Connell, R. W. 1989, *AJ*, 98, 2018
- McNamara, B. R., Wise, M., Sarazin, C. L., Jannuzi, B. T., & Elston, R. 1996, *ApJ*,
466, L9+
- Meurer, G. R., Wong, O. I., Kim, J. H., Hanish, D. J., Heckman, T. M., Werk,
J., Bland-Hawthorn, J., Dopita, M. A., Zwaan, M. A., Koribalski, B., Seibert,
M., Thilker, D. A., Ferguson, H. C., Webster, R. L., Putman, M. E., Knezek,
P. M., Doyle, M. T., Drinkwater, M. J., Hoopes, C. G., Kilborn, V. A., Meyer,
M., Ryan-Weber, E. V., Smith, R. C., & Staveley-Smith, L. 2009, *ApJ*, 695, 765
- Minkowski, R. L., & Abell, G. O. 1963, *The National Geographic Society-Palomar
Observatory Sky Survey*, ed. Strand, K. A. (the University of Chicago Press),
481–+
- Narayan, R., & Medvedev, M. V. 2001, *ApJ*, 562, L129
- Nipoti, C., & Binney, J. 2004, *MNRAS*, 349, 1509
- O'Dea, C. P., Baum, S. A., Privon, G., Noel-Storr, J., Quillen, A. C., Zufelt, N.,
Park, J., Edge, A., Russell, H., Fabian, A. C., Donahue, M., Sarazin, C. L.,
McNamara, B., Bregman, J. N., & Egami, E. 2008, *ApJ*, 681, 1035
- Oegerle, W. R., & Hill, J. M. 2001, *AJ*, 122, 2858
- Oke, J. B. 1990, *AJ*, 99, 1621
- Oonk, J. B. R., Jaffe, W., Bremer, M. N., & van Weeren, R. J. 2010, *MNRAS*, 405,
898
- Owen, F. N., Ledlow, M. J., & Keel, W. C. 1995, *AJ*, 109, 14

- Peres, C. B., Fabian, A. C., Edge, A. C., Allen, S. W., Johnstone, R. M., & White, D. A. 1998, *MNRAS*, 298, 416
- Peterson, J. R., & Fabian, A. C. 2006, *Phys. Rep.*, 427, 1
- Peterson, J. R., Kahn, S. M., Paerels, F. B. S., Kaastra, J. S., Tamura, T., Bleeker, J. A. M., Ferrigno, C., & Jernigan, J. G. 2003, *ApJ*, 590, 207
- Pope, E. C. D. 2010, *MNRAS*, 404, 451
- Pope, E. C. D., Pittard, J. M., Hartquist, T. W., & Falle, S. A. E. G. 2008, *MNRAS*, 385, 1779
- Quillen, A. C., Zufelt, N., Park, J., O’Dea, C. P., Baum, S. A., Privon, G., Noel-Storr, J., Edge, A., Russell, H., Fabian, A., Donahue, M., Bregman, J. N., McNamara, B. R., & Sarazin, C. L. 2008, *ApJS*, 176, 39
- Rafferty, D. A., McNamara, B. R., & Nulsen, P. E. J. 2008, *ApJ*, 687, 899
- Rafferty, D. A., McNamara, B. R., Nulsen, P. E. J., & Wise, M. W. 2006, *ApJ*, 652, 216
- Randall, S. W., Jones, C., Markevitch, M., Blanton, E. L., Nulsen, P. E. J., & Forman, W. R. 2009, *ApJ*, 700, 1404
- Randall, S. W., Sarazin, C. L., & Ricker, P. M. 2002, *ApJ*, 577, 579
- Reid, I. N., Brewer, C., Brucato, R. J., McKinley, W. R., Maury, A., Mendenhall, D., Mould, J. R., Mueller, J., Neugebauer, G., Phinney, J., Sargent, W. L. W., Schombert, J., & Thicksten, R. 1991, *PASP*, 103, 661
- Reiprich, T. H., Sarazin, C. L., Kempner, J. C., & Tittley, E. 2004, *ApJ*, 608, 179
- Revaz, Y., Combes, F., & Salomé, P. 2008, *A&A*, 477, L33
- Reynolds, C. S., Casper, E. A., & Heinz, S. 2008, *ApJ*, 679, 1181
- Reynolds, C. S., McKernan, B., Fabian, A. C., Stone, J. M., & Vernaleo, J. C. 2005, *MNRAS*, 357, 242
- Rodríguez-Martínez, M., Velázquez, P. F., Binette, L., & Raga, A. C. 2006, *A&A*,

- Romanishin, W. 1987, *ApJ*, 323, L113
- Russell, H. R., Sanders, J. S., & Fabian, A. C. 2008, *MNRAS*, 390, 1207
- Sakelliou, I., Merrifield, M. R., & McHardy, I. M. 1996, *MNRAS*, 283, 673
- Salomé, P., & Combes, F. 2003, *A&A*, 412, 657
- Salomé, P., Combes, F., Revaz, Y., Edge, A. C., Hatch, N. A., Fabian, A. C., & Johnstone, R. M. 2008, *A&A*, 484, 317
- Salpeter, E. E. 1955, *ApJ*, 121, 161
- Sanders, J. S., & Fabian, A. C. 2002, *MNRAS*, 331, 273
- . 2007, *MNRAS*, 381, 1381
- Sanders, J. S., Fabian, A. C., Allen, S. W., & Schmidt, R. W. 2004, *MNRAS*, 349, 952
- Sanders, J. S., Fabian, A. C., Smith, R. K., & Peterson, J. R. 2010, *MNRAS*, 402, L11
- Sanderson, A. J. R., Finoguenov, A., & Mohr, J. J. 2005, *ApJ*, 630, 191
- Santos, J. S., Rosati, P., Tozzi, P., Böhringer, H., Ettori, S., & Bignamini, A. 2008, *A&A*, 483, 35
- Schlegel, D. J., Finkbeiner, D. P., & Davis, M. 1998, *ApJ*, 500, 525
- Shapley, H., & Ames, A. 1926, *Harvard College Observatory Circular*, 294, 1
- Sharma, P., Parrish, I. J., & Quataert, E. 2010, *ApJ*, 720, 652
- Skrutskie, M. F., Cutri, R. M., Stiening, R., Weinberg, M. D., Schneider, S., Carpenter, J. M., Beichman, C., Capps, R., Chester, T., Elias, J., Huchra, J., Liebert, J., Lonsdale, C., Monet, D. G., Price, S., Seitzer, P., Jarrett, T., Kirkpatrick, J. D., Gizis, J. E., Howard, E., Evans, T., Fowler, J., Fullmer, L., Hurt, R., Light, R., Kopan, E. L., Marsh, K. A., McCallon, H. L., Tam, R., Van Dyk, S., & Wheelock, S. 2006, *AJ*, 131, 1163

- Somerville, R. S., Hopkins, P. F., Cox, T. J., Robertson, B. E., & Hernquist, L. 2008, *MNRAS*, 391, 481
- Sun, M. 2009, *ApJ*, 704, 1586
- Sun, M., Voit, G. M., Donahue, M., Jones, C., Forman, W., & Vikhlinin, A. 2009, *ApJ*, 693, 1142
- van Breugel, W., Heckman, T., & Miley, G. 1984, *ApJ*, 276, 79
- Veilleux, S., Cecil, G., & Bland-Hawthorn, J. 2005, *ARA&A*, 43, 769
- Veilleux, S., Weiner, B. J., Rupke, D. S. N., McDonald, M., Birk, C., Bland-Hawthorn, J., Dressler, A., Hare, T., Osip, D., Pietraszewski, C., & Vogel, S. N. 2010, *AJ*, 139, 145
- Vernaleo, J. C., & Reynolds, C. S. 2007, *ApJ*, 671, 171
- Vikhlinin, A., Burenin, R., Forman, W. R., Jones, C., Hornstrup, A., Murray, S. S., & Quintana, H. 2007, in *Heating versus Cooling in Galaxies and Clusters of Galaxies*, ed. H. Böhringer, G. W. Pratt, A. Finoguenov, & P. Schuecker , 48–+
- Voigt, L. M., & Fabian, A. C. 2004, *MNRAS*, 347, 1130
- Wei, L. H., Kannappan, S. J., Vogel, S. N., & Baker, A. J. 2010, *ApJ*, 708, 841
- White, D. A., Jones, C., & Forman, W. 1997, *MNRAS*, 292, 419
- Wilman, R. J., Edge, A. C., & Swinbank, A. M. 2009, *MNRAS*, 395, 1355
- Wise, M. W., McNamara, B. R., Nulsen, P. E. J., Houck, J. C., & David, L. P. 2007, *ApJ*, 659, 1153
- Zuhone, J., & Markevitch, M. 2009, in *American Institute of Physics Conference Series*, Vol. 1201, *American Institute of Physics Conference Series*, ed. S. Heinz & E. Wilcots, 383–386
- ZuHone, J. A., Markevitch, M., & Johnson, R. E. 2010, *ApJ*, 717, 908
- Zwicky, F. 1937, *ApJ*, 86, 217
- . 1938, *PASP*, 50, 218

- Zwicky, F., Herzog, E., & Wild, P. 1961, Catalogue of galaxies and of clusters of galaxies, Vol. I, ed. Zwicky, F., Herzog, E., & Wild, P.
- . 1963, Catalogue of galaxies and of clusters of galaxies, Vol. 2, ed. Zwicky, F., Herzog, E., & Wild, P.
- . 1966, Catalogue of galaxies and of clusters of galaxies, Vol. 3, ed. Zwicky, F., Herzog, E., & Wild, P.